MIT/WHOI

**Massachusetts Institute of Technology**
**Woods Hole Oceanographic Institution**

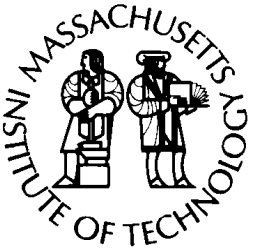


# Joint Program in Oceanography/ Applied Ocean Science and Engineering

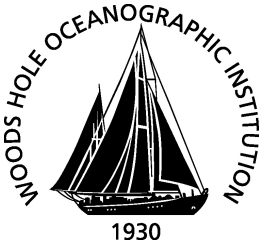


---

## DOCTORAL DISSERTATION

Seismic and Numerical Constraints on the Formation and Evolution of Oceanic Lithosphere

by

Hannah F. Mark

September 2019

# SEISMIC AND NUMERICAL CONSTRAINTS ON THE FORMATION AND EVOLUTION OF OCEANIC LITHOSPHERE

by

Hannah F. Mark
B.A., University of Chicago (2014)

Submitted in partial fulfillment of the requirements for the degree of

Doctor of Philosophy

at the

MASSACHUSETTS INSTITUTE OF TECHNOLOGY

and the

WOODS HOLE OCEANOGRAPHIC INSTITUTION

September 2019



Author……

Joint Program in Oceanography /Applied Ocean Science & Engineering
Massachusetts Institute of Technology & Woods Hole Oceanographic Institution
August 22, 2019

Certified by……

Dr. Daniel Lizarralde
Associate Scientist with Tenure, Department of Geology & Geophysics
Woods Hole Oceanographic Institution
Thesis Supervisor

Accepted by…….

Dr. Oliver Jagoutz
Professor of Geology, Department of Earth and Planetary Sciences
Massachusetts Institute of Technology
Chair, Joint Committee for Marine Geology & Geophysics

# SEISMIC AND NUMERICAL CONSTRAINTS ON THE FORMATION AND EVOLUTION OF OCEANIC LITHOSPHERE

by

Hannah F. Mark

Submitted to the MIT-WHOI Joint Program in Oceanography and Applied Ocean Science and Engineering in Partial Fulfillment of the Requirements for the Degree of Doctor of Philosophy in Marine Geophysics.

Abstract

This thesis explicates aspects of the basic structure of oceanic lithosphere that are shaped by the processes that form the lithosphere. The strength of lithospheric plates relative to the underlying mantle enables the surface plate motions and plate boundary processes that characterize plate tectonics on Earth. Surprisingly, we have a relatively poor understanding of the physical mechanisms that make the lithosphere strong relative to the asthenosphere, and we lack a reference model for ordinary lithospheric structure that can serve as a baseline for comparing geophysical observations across locations. Chapters 2 and 3 of this thesis investigate the seismic structure of a portion of the Pacific plate where the simple tectonic history of the plate suggests that its structure can be used as a reference model for oceanic lithosphere. We present measurements of shallow azimuthal seismic anisotropy, and of a seismic discontinuity in the upper mantle, that reflect the effects of shear deformation and melting processes involved in the formation of the lithosphere at mid-ocean ridges. Chapter 4 uses numerical models to explore factors controlling fault slip behavior on normal faults that accommodate tectonic extension during plate formation.

Thesis Supervisor: Dr. Daniel Lizarralde
Title: Associate Scientist with Tenure in Geology & Geophysics
Woods Hole Oceanographic Institution

# Acknowledgments

A few months ago, as my office mate Meghan and I were both getting close to defending our theses, my advisor Dan stopped by our office and shared this analogy: in grad school, he said, we were like caterpillars, happily eating fresh green leaves. Soon, though, we would graduate, leave that comfortable existence behind, and venture out into the world as butterflies, searching for scarcer food sources while floating at the mercy of the wind. This metamorphosis is exciting, of course, but it's a big change when, in Dan's words, "you can't just eat that leaf anymore." As I contemplate my impending butterfly-hood, I am grateful for all the people who have helped me get to this point and done their best to equip me for the next academic life stage.

First among those people are my advisors, Dan Lizarralde and Mark Behn. Over the last five-ish years Dan has taught me how to write a short email, change the color scheme in GVim, and pull useful information out of a set of wiggly lines. His unfailing curiosity and quest for clarity have continually inspired me, and if I haven't quite figured out how to craft a perfect topic sentence yet, that's on me, not him. From Mark, I have learned many valuable lessons about numerical methods and baseball. Amazingly, he has continued to work with me despite my dislike of both MATLAB and the Red Sox. I am very lucky to have had the chance to work with these two extraordinary scientists and mentors.

The other members of my thesis committee – John Collins, Greg Hirth, and Rob van der Hilst – have given me support and guidance through the last several years. I thank Rob for reminding me to look at my results with skepticism, and Greg for letting me convince him that receiver functions could be meaningful. John has essentially been my third thesis advisor, and I thank him for sharing his OBS expertise and for singing in the office next door. My favorite songs in his repertoire are "The Mermaid" and "Space Oddity."

Working on data from NoMelt meant that I got to collaborate with some stellar scientists, including Jim Gaherty, Rob Evans, and several of their students and postdocs. I have benefitted from their enthusiasm for group meetings and thoughtful comments on my work. On the modeling side, my chapter on normal fault models would not have been possible without Yajing Liu, who let me use her rate-and-state code and drew me numerous diagrams to explain how it worked.

I have also been lucky enough to work with a bunch of WHOI folks on things other than my thesis research. TAing for Anthony Kirincich and Gareth Lawson was incredibly fun, and I learned a lot about teaching by watching them in action. I also enjoyed assisting Stace Beaulieu with the software carpentry workshop, where I learned a bunch of bash commands that I wish I had known earlier. Jeff McGuire let me play with Salton Sea seismic data for a geodynamics project. Ann Devenish taught me the very basics of library science and showed me how to gracefully say no to jobs I didn't have time for. Lonny Lippsett helped me write an *Oceanus* article about my research that made sense to my whole family. While I didn't work with Mark Kurz or Adam Soule on anything science-related, they have both looked out for me over the last few years. I thank Adam for the hamentasch and for chairing my defense, and I thank Mark for letting me spend time with Cleo.

This thesis could not have been written without the behind-the-scenes work of many people. I appreciate everyone in the Academic Programs Office at WHOI and the Education Office at MIT

who keep the Joint Program running smoothly, including Jim Yoder, Meg Tivey, Delia Oppo, Julia Westwater, Lea Fraser, Christine Charette, Kama Thieler, Kris Kipp, Valerie Caron, and Martha Bridgers. I thank the G&G department admins, in particular Sally Houghton, Kelly Servant, Kim Deisher, and Christina Cuellar, for their help and for all the chats in the Clark South hallway. I also thank the shuttle drivers Dan Mullen, Tracy Williams, and Ron Dyer for making my very brief commute easy and pleasant. I thank Rose for taking good care of all of us.

I probably wouldn't have gone to graduate school if not for Dion Heinz, Andy Campbell, and David Rowley at the University of Chicago. I thank Andy and Dion for giving me my first lab job and introducing me to the wonders of diamond anvil cells. I thank David for making me read *The Origin of Continents and Oceans.*

My fellow students in the Joint Program are as fine a peer group as I could ever have wished for. I thank Nathan Miller, Helen Feng, Laura Stevens, and Jean-Arthur Olive for their mentoring (official and un); Noelle Held and Katie Samuelson for a truly surprising birthday cake; Jessie Pearl, Jimmy Bramante, and Ben Jones for taking on the Mass Dash; Katie Castagno for the haircuts and for letting me hang out with Maple; Lizzie Wallace for also wearing the weird shoes; Billy Shinevar for writing the SCARF paper so I didn't have to; Fiona Clerc for not quite smuggling an Azorean pineapple; Net Charoenpong and Gabi Farfan for joining me on early morning trips to MIT; Laura Weber for sharing my enthusiasm for sourdough; Emmanuel Codillo for being so cheerful all the time; Casey Zakroff for the outreach adventures; Chrissy Hernandez and Suzi Clark for joining the chorale; and, most of all, Meghan Jones, for being the very best office mate, house mate, and friend.

I have met a number of non-scientists over the last few years who have made my life in Woods Hole much richer. I thank all of the Tunes at Noon musicians for playing the new tunes I brought in. I am grateful to the Vineyard Swordfish, who taught me four and a half dances and even let me play with the band sometimes. My fellow singers in the Falmouth Chorale and Chamber Singers have continually amazed me with their musicianship and their kindness. I especially thank Trish, Carla, Adrian, and all the other soprani for hitting the high As in the Beethoven; Dave, Ed, and Tom for anchoring the bass line; Megan for remembering all the warmup stretches; John for occasionally giving us Renaissance pieces to sing; and Sarah for being Sarah. Glenn, Ken, and Lenny in the Falmouth Track Club helped me end many workweeks on a high note with the Friday Five. Margaret and everyone at the Woods Hole Public Library gave me lots of great book recommendations.

I thank Charlotte, Margot, Ludda, Helena, Kelly, Devon, Dennis, Natalia, Rene, and Evie for dinner parties, game nights, and dog snaps. I thank Quinn, Jason, Ida, and Philip for keeping in touch.

I have, objectively speaking, the best family there is. My aunts, uncles, cousins, and grandmother now all know the meaning of the word "lithosphere." My parents have supported me in all things. My sister has always led the way.

Funding for this research was provided by a National Science Foundation Graduate Research Fellowship, an MIT Presidential Fellowship, the National Science Foundation Division of Earth Sciences (EAR) contract #1010432, and the WHOI Academic Programs Office.

# Contents

# List of Figures

# List of Tables

# Chapter 1

# Introduction

This thesis focuses on the structure and properties of the lithosphere, the rigid outermost layer of the Earth that comprises the plates of plate tectonics. Plate tectonic theory describes a dynamic system where lithospheric plates are created and destroyed over geologic time, cycling carbon, water, and other compounds and elements between surface reservoirs and the deep Earth. The plates move relative to one another on the surface, continually reshaping the configuration of continents and ocean basins. Surface plate motions depend on the properties of plates: specifically, on their strength. Strong plates are able to slide relatively easily over the underlying mantle. Strong plates can also maintain internal rigidity to first order, localizing deformation to their boundaries and enabling the plate boundary processes that characterize active tectonics.

Surprisingly, we do not fully understand why the lithosphere is strong compared to the underlying mantle. The vast majority of the lithosphere lies at depths within the Earth that are inaccessible to us for direct sampling. We therefore rely on remote sensing data, such as seismic and electromagnetic data, to try and determine how the structure of the lithosphere, in terms of composition, temperature, and mineral fabrics, results in strong, internally rigid plates. While significant progress has been made in measuring the geophysical properties of the lithosphere, including seismic velocities, anisotropy, and conductivity, interpreting these measurements is difficult because the observed properties vary across locations, and we lack a reference model for basic lithospheric structure to use as a baseline for comparisons between locations.

In Chapters 2 and 3 of this thesis, we investigate the seismic structure of a relatively undeformed and unaltered oceanic plate in the central Pacific. The simple tectonic history of this plate enables us to use measurements of its structure as a reference point for minimally altered oceanic lithosphere. In Chapter 2, we measure azimuthal anisotropy in the uppermost mantle. This measurement is interpreted primarily in terms of mineral fabrics generated by shear deformation as the plate was forming at a mid-ocean ridge (e.g., Hess, 1964). In Chapter 3, we image an abrupt decrease in seismic velocities, or seismic discontinuity, in the upper mantle. The discontinuity is best explained by the presence of a relatively sharp gradient in hydration established by mantle melting during plate formation. Water content is expected to strongly influence mantle viscosity (e.g., Hirth & Kohlstedt, 1996), so a contrast in hydration could help to accommodate relative motion between the rigid lithosphere and the underlying mantle.

Strong plates that localize strain in narrow boundary zones occasionally break at those boundaries, releasing accumulated stress via a spectrum of fault behaviors from slow creep to earthquakes (e.g., Peng & Gomberg, 2010). Over the last several decades, our understanding of the properties that control these fault behaviors has changed dramatically due to the development of the theory of rate-and-state friction. Rate-and-state friction describes how the frictional properties of a material vary depending on *rate*, the rate of slip on a frictional interface, and *state*, a quantity that describes the integrated history of slip on the interface (e.g., Dieterich, 1972, 1978; Marone, 1998; Rice & Ruina, 1983; Scholz, 1998). The time-varying frictional properties described by rate-and-state friction have been shown to explain much of the range of fault behaviors seen at subduction zone megathrusts and oceanic transform faults (e.g., Liu et al., 2012; Liu & Rice, 2007). In Chapter 4 of this thesis, we use rate-and-state friction models to explore factors that control the relative proportions of stress released in earthquakes versus aseismic slip for normal faults that accommodate tectonic extension during plate formation at ridges.

The mapping between the geophysical parameters that we measure and the physical structure of the lithosphere is highly non-unique. Numerical models are therefore an important complement to observational studies, as they enable us to explore the sensitivity of observable quantities to the physical parameters we are interested in, such as mineral fabrics or gradients in mantle composition. The appendix to this thesis describes previous work on modeling the development of mineral fabric

in the upper mantle, and discusses future directions for models relevant to the measurements described in Chapters 2 and 3.

### 1.1 The NoMelt experiment

The data used in Chapters 2 and 3 of this thesis are from the NoMelt experiment, which aimed to characterize the detailed structure of oceanic lithosphere by gathering and analyzing multiple complimentary types of geophysical data at a single location in the central Pacific. The experiment was situated in the center of a stable spreading segment between the Clarion and Clipperton fracture zones on ~70 Myr old lithosphere (Barckhausen et al., 2013). The plate at this location appears to have a simple tectonic history, suggesting that measurements of plate structure obtained at this site can serve as a reference for the basic structure of oceanic lithosphere. An array of 26 broadband ocean bottom seismometers (OBS) were deployed on the seafloor to record passive seismicity for ~1 year, along with a 6 magnetotelluric instruments. An array of 31 short-period OBS was temporarily deployed alongside the broadband instruments to record long-offset active-source seismic refractions, and seismic reflection data were also collected with a 6 km multi-channel seismic streamer. The measurements presented in Chapters 2 and 3 of this thesis are part of a larger body of work from NoMelt that has provided constraints on the seismic and electrical structure through the crust and upper 300 km of the oceanic mantle beneath the NoMelt array (Lin et al., 2016; Lizarralde et al., 2018; Ma et al., 2018; Matsuno & Evans, 2017; Russell et al., 2019; Sarafian et al., 2015).

### 1.2 A baseline for azimuthal anisotropy in the lithospheric mantle

Laboratory experiments have demonstrated that deformation of mantle materials can align olivine and other minerals into preferred orientations (e.g., Skemer & Hansen, 2016; Zhang et al., 2000; Zhang & Karato, 1995). Simple models for mantle corner flow beneath mid-ocean ridges, where mantle material upwells, turns the corner at the ridge, and flows horizontally out from in the direction of plate spreading, predict observable seismic anisotropy in the uppermost oceanic mantle with the fastest velocities oriented parallel to the spreading direction (Hess, 1964). Observations validate this prediction to first order, but the observed strength of azimuthal anisotropy and the orientation of the fast direction with respect to paleospreading vary significantly between locations (e.g., Gaherty et al., 2004; Morris et al., 1969; Raitt et al., 1969; Shimamura, 1984; Takeo et al., 2016;

VanderBeek & Toomey, 2017). This variability has been used to suggest that observations of anisotropy in the lithospheric mantle are sensitive to variations in mantle flow patterns at mid-ocean ridges.

Using anisotropy to understand variations in mantle flow associated with plate spreading requires a baseline for the seismic expression of mantle corner flow. In Chapter 2, we measure seismic anisotropy in ~70 Myr old Pacific lithosphere at the NoMelt site, where the simple tectonic history of the plate indicates that the observed structure can serve as a reference for anisotropy due to plate spreading. We also measure vertical gradients in the strength of anisotropy which are interpreted as the anisotropic signature of aligned cracks closing due to increasing pressure at depth (Greenfield & Graham, 1996; Hudson, 1981). Such cracks, which might form due to thermal contraction as the plate cools, could provide permeable pathways for water to infiltrate and react with crust and mantle rocks, thus chemically altering shallow parts of the plate.

### 1.3 Physical mechanisms for the Gutenberg discontinuity and the lithosphere-asthenosphere boundary

The fact that plates move on Earth's surface implies the existence of a shear zone that accommodates the motion of the rigid lithosphere relative to the weaker asthenosphere. The sharpness of this transition, and the physical mechanisms that generate it, govern the coupling between the plates and flow in the underlying mantle, which, in turn, affects the balance of forces that drive plate tectonics and the wavelength of mantle convection (Ghosh et al., 2008; Höink et al., 2011; Lenardic et al., 2006; Richards et al., 2001; Richards & Lenardic, 2018). While this transition is typically referred to as the lithosphere-asthenosphere boundary (LAB), constraints on its location and sharpness are weak, and it is not clear whether it is sharp and boundary-like or is instead a broad zone of shear.

If the transition from lithosphere to asthenosphere was controlled by temperature alone, then the strength of the plates relative to the underlying mantle would be due solely to the temperature dependence of viscosity. However, not all seismic observations can be explained with temperature-dependent viscosity as the only control on lithospheric strength (Faul & Jackson, 2005; Jackson et al., 2002; Stixrude & Lithgow-Bertelloni, 2005). The viscosity of the mantle may also be influenced

by changes in its composition (Hirth & Kohlstedt, 1996; Phipps Morgan, 1997), or by the presence of melt (Kawakatsu et al., 2009; Schmerr, 2012). A sharp compositional gradient, or accumulated melt-rich layers, could generate viscosity contrasts to help accommodate plate motion relative to the underlying mantle. Determining the physical mechanisms responsible for the transition between the lithosphere and asthenosphere is difficult because different types of seismic observations appear to support different physical mechanisms for the LAB. Tomographic velocity models show velocity gradients suggestive of a thermal lithosphere (e.g., Beghein et al., 2014), while receiver functions and SS precursors image sharp discontinuities potentially indicative of compositional boundaries or melt accumulation (Kawakatsu et al., 2009; Kumar & Kawakatsu, 2011; Schmerr, 2012; Tharimena et al., 2017).

In Chapter 3, we present observations of the seismic Gutenberg discontinuity (G) in the upper mantle beneath the NoMelt site. Combined constraints from the receiver functions and measurements of the local seismic and electrical structure at the NoMelt site suggest that the G discontinuity represents a dehydration boundary (Sarafian et al., 2015). The top of the observed discontinuity appears to be at a shallower depth than changes in the strength and orientation of azimuthal anisotropy observed at the site (Lin et al., 2016). While a dehydration boundary is expected to generate a viscosity contrast that could help to localize some of the shear between the plate and the underlying mantle (Hirth & Kohlstedt, 1996; Karato et al., 1986), separation between G and the shift in azimuthal anisotropy suggests that relative motion between the lithosphere and asthenosphere is accommodated over a broad depth range extending beyond the discontinuity.

### 1.4 Causes of variable seismic coupling on mid-ocean ridge normal faults

Strain associated with plate spreading at mid-ocean ridges is accommodated by a combination of magmatism and tectonic extension (e.g., Buck et al., 2005; Escartín et al., 1999). Measurements of seismic moment release relative to total tectonic strain accommodation have shown that the seismic coupling coefficient, defined as the fraction of slip on faults that occurs seismically, varies systematically with spreading rate for mid-ocean ridge normal faults (Bird et al., 2002; Bird & Kagan, 2004; Cowie et al., 1993; Frohlich & Wetzel, 2007; Sobolev & Rundquist, 1999). Almost all of the slip on normal faults near fast-spreading ridges is aseismic, while for faults near slow-spreading ridges, as much as 60% of fault slip may occur seismically (Cowie et al., 1993; Olive & Escartín,

2016). This difference in fault behavior across spreading rates could be a consequence of differences in the size of the seismogenic zone on faults due to variations in thermal structure and fault geometry across spreading rates (Boettcher et al., 2007; Liu et al., 2012; Solomon et al., 1988). Alternatively, fault behavior might be controlled by variable frictional properties on fault surfaces, as faults near slow-spreading ridges are expected to experience greater amounts of chemical alteration and serpentinization while they are still active (Liu & Rice, 2007; McGuire et al., 2012; Roland et al., 2012).

In Chapter 4, we use rate-and-state friction models to simulate seismic cycles on oceanic normal faults and explore the effects of different thermal and geometric parameters on fault behavior. The models indicate that the seismic coupling coefficient scales with the size of the seismogenic zone relative to the critical patch size for earthquake nucleation, and the range of variability observed across mid-ocean ridges can be explained by variations in fault geometry and thermal structure without invoking material heterogeneity. We also analyze earthquake catalogs for the Corinth Rift, and find that the scaling between seismic coupling coefficient and seismogenic zone width for mid-ocean ridges can be extended to explain seismic coupling in this continental rift setting.

### 1.5 Interpreting upper mantle anisotropy using geodynamic models

Laboratory studies linking the formation of anisotropic mineral fabrics to deformation suggest that observations of coherent seismic anisotropy in the upper mantle represent mineral fabrics formed by mantle flow. However, interpreting observations of seismic anisotropy beyond basic assessments of how well fast velocities align with present or past plate motion is challenging, because it requires integrating the grain-scale deformation processes that form mineral fabrics with plate-scale flow patterns based on observations that are filtered through the particular resolution of seismic data.

Numerical models help bridge the gaps between the sample scale and the plate scale by generating predictions for anisotropy that can be compared to seismic observations. In the Appendix, we describe previous efforts to model fabric development under different assumptions for mantle rheology and discuss future directions for anisotropy models that integrate multiple rheological factors previously considered in isolation. We also present preliminary models of anisotropic fabric development associated with plate spreading.

# Chapter 2

# Azimuthal seismic anisotropy of 70 Ma Pacific-plate upper mantle

This chapter was originally published as: Mark, H. F., Lizarralde, D., Collins, J. A., Miller, N. C., Hirth, G., Gaherty, J. B., & Evans, R. L. (2019). Azimuthal seismic anisotropy of 70-Ma Pacific-plate upper mantle. Journal of Geophysical Research: Solid Earth, 124, 1889-1909. Used with permission as granted in the original copyright agreement.

## 2.1 Abstract

Plate formation and evolution processes are predicted to generate upper mantle seismic anisotropy and negative vertical velocity gradients in oceanic lithosphere. However, predictions for upper mantle seismic velocity structure do not fully agree with the results of seismic experiments. The strength of anisotropy observed in the upper mantle varies widely. Further, many refraction studies observe a fast direction of anisotropy rotated several degrees with respect to the paleospreading direction, suggesting that upper mantle anisotropy records processes other than 2D corner flow and plate-driven shear near mid-ocean ridges. We measure 6.0 ± 0.3% anisotropy at the Moho in 70 Ma lithosphere in the central Pacific with a fast direction parallel to paleospreading, consistent with mineral alignment by 2D mantle flow near a mid-ocean ridge. We also find an increase in the strength of anisotropy with depth, with vertical velocity gradients estimated at 0.02 km/s/km in the fast direction and 0 km/s/km in the slow direction. The increase in anisotropy with depth can be explained by mechanisms for producing anisotropy other than intrinsic effects from mineral fabric, such as aligned cracks or other structures. This measurement of seismic anisotropy and gradients reflects the effects of both plate formation and evolution processes on seismic velocity structure in mature oceanic lithosphere, and can serve as a reference for future studies to investigate the processes involved in lithospheric formation and evolution.

## 2.2 Introduction

The structure of mature oceanic lithosphere derives from plate formation processes at mid-ocean ridges combined with off-axis modification as the plate ages. The composition of the lithosphere is derived from melting of the upper mantle at mid-ocean ridges. Some mantle minerals preferentially melt and are extracted at the ridge to form the crust, while other minerals remain in the residual lithospheric mantle. Lab-based melting models predict that this will result in a compositional gradient from lherzolite at depth up to depleted harzburgite in the shallowest mantle (e.g., Langmuir et al., 1992), and evidence for such a gradient is seen in peridotite samples from seafloor dredges and ophiolites (e.g., Constantin et al., 1995; Dick et al., 1984; Kelemen et al., 1992; Ringwood, 1958). Ridge processes also produce mineral fabrics in the lithosphere. The mantle experiences large shear strains during corner flow at the ridge, and laboratory experiments show that this can impart an anisotropic fabric that can be locked into the lithospheric mantle as minerals are aligned into a crystallographic preferred orientation (CPO) by shear (e.g., Nicolas et al., 1973; F. J. Turner, 1942; Zhang & Karato, 1995). Off-axis, plate structure continues to evolve: as plates cool, they undergo tensional cracking and serpentinization (e.g., Cormier et al., 2011; Dunn, 2015; Korenaga, 2007; Mishra & Gordon, 2016; Sandwell & Fialko, 2004).

Our current understanding of plate formation and evolution processes, and the relationships between physical properties and seismic velocities, enable us to make predictions about the seismic velocity structure of oceanic lithosphere including seismic anisotropy and vertical gradients. The vertical velocity gradient in the uppermost oceanic mantle is predicted to be negative (e.g., Stixrude & Lithgow-Bertelloni, 2005) as the effects on seismic velocities due to compositional gradients resulting from melt extraction (Langmuir et al., 1992) and thermal gradients established by plate cooling (e.g., Christensen, 1979) are stronger than the effect of increasing pressure with depth (O. L. Anderson et al., 1968; Greenfield & Graham, 1996; Meglis et al., 1996). For dominantly two dimensional (2D) mantle flow, the alignment of anisotropic olivine crystals into a CPO is expected to produce seismic anisotropy in the lithospheric mantle such that *P* wave velocities are fastest for seismic waves propagating parallel to the direction of plate spreading (Hess, 1964; Mainprice, 2015; Skemer & Hansen, 2016; F. J. Turner, 1942; Verma, 1960; Zhang & Karato, 1995). The azimuth along which *P* wave velocities are largest is referred to as the fast direction of anisotropy. If aligned

cracks are present due to off-axis cooling, they are also predicted to produce anisotropy as velocities are slowed normal to the cracks (e.g., D. L. Anderson et al., 1974; Hudson, 1981; Nishizawa, 1982).

Seismic observations have shown that anisotropy is indeed present throughout the oceanic upper mantle, but other aspects of these predictions for lithospheric velocity structure are either unverified by or in conflict with observations. The fact that strong *Pn* phases are seen in seismic refraction experiments requires that positive velocity gradients exist in at least some parts of the oceanic upper mantle, contrary to predictions from physical models. Anisotropy consistent with a CPO formed by 2D mantle flow has been measured at some locations in the oceanic upper mantle (Raitt et al., 1969; Shimamura, 1984; Snydsman et al., 1975), but many refraction studies measure anisotropy where the fast direction is not parallel to the paleospreading direction, suggesting that 3D mantle flow patterns and/or other processes that influence lithospheric anisotropy may be relatively common (Dunn & Toomey, 1997; Keen & Barrett, 1971; Keen & Tramontini, 1970; Morris et al., 1969; Shearer & Orcutt, 1986; Shintaku et al., 2014; Toomey et al., 2007; VanderBeek et al., 2016; VanderBeek & Toomey, 2017). Further, estimates of the strength of anisotropy vary widely (e.g., Gaherty et al., 2004; Shimamura, 1984).

The lack of consistency among observations of anisotropy and differences between observed and predicted velocity structures raise questions about the processes involved in lithospheric formation and evolution. It is not clear whether the anisotropy we observe is set primarily by mantle corner flow during plate formation, or if plate evolution processes, such as cracking and chemical alteration, contribute significantly to the signal. Azimuthal anisotropy is often discussed as a product of 2D mantle flow, but the role of 3D flow patterns at mid-ocean ridges and their effects on anisotropic fabric in the lithosphere are not well understood. Resolving these questions requires a baseline of observations in oceanic lithosphere from a simple setting where we expect the links between plate formation and evolution processes and the observed seismic structure to be relatively straightforward.

We present a measurement of upper mantle anisotropy and vertical velocity gradients in 70 Ma lithosphere in the central Pacific using active-source refraction data acquired during the 2011 NoMelt experiment. This measurement can serve as a reference model for upper mantle anisotropy, and provides a point of comparison for future, targeted studies of anisotropy in oceanic lithosphere.

We find that the magnitude of anisotropy increases with depth. The depth variation suggests that the effective anisotropy includes some extrinsic component, such as anisotropy due to aligned or spatially organized cracks.

### 2.3 The NoMelt Experiment and data

The NoMelt experiment was conducted in 2011–2012 on ~70 Ma lithosphere between the Clarion and Clipperton fracture zones in the central Pacific (Figure 2-1) and was designed to image the detailed seismic and electrical structure of "normal," mature oceanic lithosphere and the underlying asthenosphere. "Normal" here refers to lithosphere with a simple evolutionary history, where the effects of processes involved in plate formation and evolution should be minimally overprinted by the effects of more complex tectonics. At an age of 70 Ma the plate is no longer directly influenced by ridge processes, and at this particular site there is no evidence for modification of the lithosphere since its formation by, for example, hotspot volcanism. The estimated paleospreading half-rate at this location is intermediate at 35 mm/yr (Barckhausen et al., 2013).

The seismic component of NoMelt consisted of a 600x400 km array of 26 broad-band (BB) ocean-bottom seismometers (OBS), 22 of which were recovered, and 34 short-period (SP) OBS, 33 of which were recovered. The SP instruments were deployed at 20 km intervals along Line 02 (L02), the main active-source transect striking at an azimuth of ~78.5ºN, parallel to the plate-kinematic flow line; and at 50 km intervals along Line 06 (L06), a 200 km line normal to the center of the main transect (Figure 2-1). The OBS array recorded airgun shots fired by the R/V *M.G. Langseth's* 36-element array. Shots were fired along L02, L06, and Line 04 (L04), a semicircle with radius 75 km centered at the intersection of L02 and L06. A shot interval of 4 minutes was used to ensure that previous shot noise did not obscure refraction arrivals at large offsets. The source geometry was designed to provide large-offset refraction data along L02, good controls on velocities parallel and perpendicular to the plate kinematic flow line with L02 and L06, and full azimuthal coverage with L04.

Broadband data from NoMelt have been used to constrain shear wave velocity and anisotropy in the upper mantle down to 300 km (Lin et al., 2016). Lin et al. (2016) observe the strongest anisotropy in the shallowest part of their model (G parameter ~2.5%), with the fast direction approximately

parallel to paleospreading. They attribute the shallow anisotropy to high strain in the lithospheric mantle during corner flow and plate spreading, and propose that anisotropy deeper in the asthenosphere could result from pressure-gradient-driven return flow or density-driven small-scale convection beneath the plate. In this study, we present a measurement of *P*-wave anisotropy within the upper ~7 km of the mantle.

### 2.4 Methods and results

We estimate azimuthal anisotropy in the upper ~7 km of the mantle using a delay-time approach (e.g., Raitt et al., 1969). Delay times are the differences between observed traveltimes of mantle refractions (*Pn*) and times predicted for propagation through an isotropic mantle. These differences are interpreted as the effect of anisotropic wavespeeds in the upper mantle. We calculate the delay times and model them in terms of anisotropic elasticity parameters.

The calculation of delay times from observed *Pn* traveltimes involves accounting for two main traveltime effects separate from the effects of anisotropy: effects unrelated to mantle propagation (static effects), and effects due to both azimuthal variation in traveltime through an isotropic 1D crust and variable propagation distances within the mantle (propagation effects). The dominant static effect is due to variable water depth. High-quality swath bathymetry data collected during the NoMelt survey are used to correct for water depth variations. Correcting for propagation effects is done using raytracing methods, but the correction relies on estimates of mantle velocity at different azimuths. This means that calculating the delay times used to determine the anisotropic velocities requires prior knowledge of the azimuthal velocity variation, making the measurement of azimuthal anisotropy from refraction data a non-linear problem. We address this nonlinearity by solving the problem with an iterative approach, described below, beginning with an initial estimate of azimuthal velocity variation determined directly from the data. This initial estimate is obtained by fitting traveltime as a function of source–receiver offset. The offset dependence of traveltime at a given azimuth also provides sensitivity to the azimuthal variation of vertical velocity gradients. We incorporate gradients into the propagation correction and use a grid-search method to find a preferred model for vertical velocity gradients along with the anisotropy model.

We analyzed 7,961 refraction traveltimes observed at 31 OBS from shots along L02, L04, and L06. The traveltimes were picked by hand, as opposed to with an automatic picking algorithm. The majority of the picks (64%) are from along L02 at azimuths near 79°N and 259°N (Figure 2-2). About 64% of picks are at source–receiver offsets between 35 and 100 km with the distribution peak at 90 km, and 36% are between 100 and 165 km (Figure 2-2). We show that an inversion of synthetic traveltimes with the same offset and azimuthal distributions as the NoMelt data recovers a known velocity model equally well as data that have a uniform distribution of azimuth and offset. However, binning tests indicate that the uneven distribution of azimuths in the data skews our inversion, so we devise a weighting scheme to mitigate the effects of the data distribution.

The following sections describe the steps outlined above, including the application of static corrections, the initial estimate of azimuthal anisotropy, and the iterative application of propagation corrections and linear inversion for azimuthal anisotropy. The inversion is done with two parameterizations: one with no vertical velocity gradients, and one with vertical gradients that can vary by azimuth. We present the results alongside the methods to demonstrate the effect of each step in the process, and because the methodology depends on the results in important ways. In particular, we present inversions of azimuthally binned versus un-binned data, and the resulting models have slightly different fast direction orientations, suggesting that the large amount of data along L02 leverages the fast direction estimate. We therefore also present the results of inversions where the data along the L02 azimuth and back azimuth are down-weighted. The end result is three pairs of models: one based on all of the traveltime data equally weighted, one based on azimuthally binned data, and one based on the data with L02 traveltimes down-weighted. The six models are slightly different from one another but are equally valid, and we describe the implications of those differences for our preferred final model.

### 2.4.1 Data processing and reduction

Processing steps for the OBS data included band-pass filtering, deconvolution, OBS relocation and, for the BB OBS, resampling. The data were filtered using an 8-pole, minimum-phase Butterworth filter with corner frequencies of 4 and 15 Hz to increase the signal-to-noise ratio of the *Pn* phase, which has a dominant frequency of ~10 Hz. A linear prediction deconvolution with a filter length of 0.2 seconds and a prediction distance of 0.01 seconds was applied using the software package

*SIOSEIS* (Henkart, 2003) to attenuate reverberations from shallow structure. The SP OBS recorded at 200 samples per second, and the BB OBS at 50 samples per second. The BB OBS were resampled to 5 ms to aid in picking.

The seafloor locations of the SP OBS were determined using direct water wave arrival times and a grid-search centered on the OBS deployment locations. For each OBS, predicted traveltimes for the direct water wave were calculated for a grid of positions surrounding the deployment location, with the depth at each position taken from the multibeam bathymetry grid. At each grid point location, the root mean square error (RMSE) of the predicted traveltimes was calculated with respect to the observed traveltimes. This constrained the instrument location to within the set of positions where the RMSE was less than or equal to the uncertainty of the observed traveltimes. The seafloor location was chosen as the position in that set closest to the sea-surface deployment location. Each estimated seafloor OBS location was less than 600 m away from its corresponding deployment location. The BB OBS were located by ranging to the instruments from several azimuths using 12 kHz acoustic signals.

Traveltime data were obtained by hand-picking *Pn* first arrivals on the vertical ground-motion components of 23 SP and 8 BB OBS. Where corresponding pairs of sources and receivers were available, traveltimes were checked for reciprocity. The traveltime picks covered 360° of azimuth across the center of the array (Figure 2-2). The azimuthal distribution of data at offsets greater than 165 km is sparse. We therefore chose to use only picks with source–receiver offsets up to 165 km in the analysis for anisotropy. In addition, we do not use picks from shots along the western 180 km of L02. For shots along the eastern 420 km of L02, OBS receiver gathers show a pattern of horizontal phase velocity of the *Pn* branch out to ~250 km that is similar for all instruments, indicative of a mostly 1D uppermost mantle velocity structure. This pattern changes abruptly 180 km from the western end of L02, near the location indicated in Figure 2-3. The *Pn* refraction phase observed over the western portion of L02 has a horizontal phase velocity that is variable and generally greater than in the east, indicative of some amount of variable uppermost mantle structure west of km 180. The change that occurs across km 180 presumably reflects a relatively minor transient event that occurred at the ridge, such as the propagation of a ridge discontinuity, since there are no dramatic bathymetric or crustal-scale features marking this location.

### 2.4.2 Static corrections

Static time corrections were applied to the data to correct for the effects of variable water depth and sediment thickness on traveltimes. Although the NoMelt site has a relatively thin sediment cover (~200 m) and low topographic relief, these time corrections are important for our measurement because the traveltime signal from azimuthal anisotropy is small. Water depth along the shot lines varied by ~300 meters, and for a standard water velocity of 1.5 km/s, a 300 m increase in water depth adds approximately 200 milliseconds of traveltime unrelated to mantle velocity structure. A similar effect is seen for variations in sediment thickness on both the source and receiver sides of the raypath. This is a significant time contribution relative to that of anisotropy: for comparison, in a medium with 7% anisotropy, similar to what has been previously observed in the Pacific (Keen & Barrett, 1971; Morris et al., 1969; Raitt et al., 1969), the traveltime difference between the fast and slow directions for a mantle refraction at 75 km is only ~800 ms.

The static corrections were calculated based on high-resolution swath bathymetry and multi-channel seismic (MCS) data. MCS data from L02 and L06 were stacked and time-migrated using Paradigm Geophysical's *Echos* software. The traveltime to the basement was picked on the migrated sections and those traveltimes were used along with bathymetry data to estimate sediment thickness along L02 and L06. To calculate source-side statics, we used a ray parameter of 1/8.5 s/km to find the piercing points at which each down-going ray intersects the seafloor and basement. Traveltimes through the water and sediments were estimated based on the piercing points using a constant water velocity of 1.5 km/s and sediment velocity of 1.8 km/s, and those times were subtracted from traveltimes calculated for a uniform water depth of 5175 m and a uniform sediment thickness of 120 m to obtain the source-side static corrections. Receiver-side statics were also calculated based on 120 m thick sediments, assuming a vertical upgoing ray through the sediments. Since all of the OBS were located along L02 and L06, receiver-side statics were applied to all traveltime picks. However, the L04 MCS data could not be satisfactorily migrated, so the L04 source-side statics corrected for variable water depth but not for sediment thickness. The static corrections were on the order of 50-100 milliseconds. The static corrections were applied to the OBS data before picking traveltimes because removing the effects of bathymetry and sediments on the source side greatly improved phase coherence for *Pn*.

### 2.4.3 Propagation corrections

Calculating delay times from picked and static-corrected *Pn* traveltimes involves accounting for the traveltime contributions from two propagation effects: variable propagation distance through the mantle, and azimuthal variation in crustal propagation times. The *Pn* delay time is the difference between the observed traveltime of a *Pn* phase that has propagated some distance through the mantle, and the predicted traveltime for propagation through an isotropic mantle over the same distance. Since the time delay with respect to traveltime in an isotropic mantle accrues along the ray path, the magnitude of the delay time depends on the mantle propagation distance, and this dependency must be accounted for in order to use the variation of delay times with azimuth to estimate anisotropic parameters. The NoMelt *Pn* traveltime data span a range of source–receiver offsets (Figure 2-2) and thus a range of mantle propagation distances. Further, these traveltimes include propagation times through the crust, which also vary with azimuth if the mantle is anisotropic. This is true even when the crustal velocity structure is isotropic because the horizontal propagation distance in the crust depends on the critical angle for refraction, which in turn depends on the velocity at the top of the mantle.

We use raytracing to estimate the propagation effects and subtract those effects from the static-corrected traveltimes. For each pick, the full offset was traced through a water layer, sediment, crust, and mantle in a model with an anisotropic mantle, using the mantle velocity corresponding to the pick azimuth. Velocity depth gradients in the mantle were set as a function of azimuth. The choice of gradients is discussed further in Section 2.5. At the same azimuth, and with identical water, sediment, and crustal layers, a ray was traced such that it traveled a set reference distance horizontally in the mantle. The propagation correction is the difference between the traced time at the full distance, and the traced time at the reference mantle propagation distance. Algebraically, we can write the propagation correction $T_{corr}$ as

$$T_{corr} = T_{M,ref} - T_{M,X} - T_{C,X} \quad (1)$$

where $T_{M,ref}$ is the traced traveltime in an anisotropic mantle for the reference distance, and $T_{M,X}$ and $T_{C,X}$ are the traced traveltimes in the anisotropic mantle and the crust, respectively, for the true source–receiver offset. Subtracting the propagation correction from the observed traveltime

accounts for time spent traversing the crust as well as the difference in mantle traveltime due to source–receiver offset.

The delay time $dT$ is calculated as

$$dT = T_{obs} - T_{corr} - T_{M,iso} \quad (2)$$

where $T_{obs}$ is the observed total traveltime and $T_{M,iso}$ is the traced traveltime in an isotropic mantle for the reference distance. This produces a set of delay times that are referenced to the chosen reference distance for horizontal mantle propagation. The average horizontal distance that a NoMelt *Pn* phase traveled through the water column, sediments, and crust is ~16 km, so a reference mantle propagation distance of 75 km is used such that the total average reference offset is 91 km, matching the peak of the distribution of source–receiver offsets in the data (Figure 2-2).

Uncertainty in the delay times could come from three main sources: the lack of sediment source-side statics along L04, uncertainty in OBS locations propagated through the propagation correction, and picking error. The contribution from the L04 sediment statics should be very small since the combined source- and receiver-side static corrections were generally under 100 milliseconds in total. The uncertainty in instrument positions is likely to be small after relocation compared to total source–receiver offsets, and we do not observe coherent shifts in the residuals by station indicative of large location errors. The contribution from picking error is likely to be similar across the dataset since picks are made with consideration for the correlation between arrivals on adjacent traces. Here we assume that all of our picks have the same uncertainty.

Calculating the propagation corrections requires a model of the anisotropic mantle velocity structure, so the determination of the propagation corrections and the model of mantle velocity structure are done together in an iterative inversion. The initial velocity model for the propagation correction was determined by binning the traveltime data into 15° azimuthal bins and fitting a line to the traveltimes versus offset within each bin. The slopes of these lines were used as an initial estimate of velocity within each azimuthal bin (Figure 2-4). The bin velocities indicate a clear azimuthal variation in wavespeed. The initial propagation correction was calculated by raytracing through the piecewise bin velocity model described above.

The intercept times of the lines fit to the binned traveltime data were used to constrain the crustal portion of the model for the propagation correction. The intercept time, which represents the vertical component of propagation through water, sediments, and crust, is proportional to the product of twice the crustal thickness times the vertical slowness at the critical angle for refraction. That critical angle is a function of the velocity at the top of the mantle. The horizontal component of crustal propagation also depends on the critical angle, and these dependencies introduce an azimuthal variation into the crustal propagation times of the *Pn* phase for an anisotropic mantle even when the crust itself is isotropic. We used the proportionality between the intercept time and crustal thickness to determine the crustal velocity model. Using a water depth of 5175 m and sediment thickness of 120 m based on MCS and multibeam bathymetry data from the NoMelt site, and setting the top mantle velocity as the average of the bin velocities, we calculated intercept times for different assumed thicknesses of oceanic crustal Layers 2 and 3. The two crustal layer thicknesses were taken to be equal, and the crustal velocities were based on a typical 1D velocity model (e.g., Bratt & Purdy, 1984; Fowler, 2005). These predicted intercept times were compared to the average intercept time for the data, and the best-fitting layer thickness was approximately 3 km, giving an overall crustal thickness of 6 km. This crustal model was used in all raytracing. We chose to use an isotropic crustal model because the traveltime residuals due to crustal azimuthal anisotropy are small (~30 milliseconds, Dunn, 2015) relative to the contributions from mantle anisotropy, especially for mantle refractions which only propagate a short distance in the crust. The mean horizontal distance traveled in the crust, sediment, and water column was ~16 km, corresponding to ~6.5 seconds of traveltime.

We used two different model parameterizations in the inversion for mantle anisotropy. Both parameterizations include the crustal model described above. The parameterizations differ in the velocity gradient with depth through the mantle, with one parameterization having no vertical velocity gradient and the other having a positive gradient that varies with azimuth. We consider the parameterization with positive gradients because the *Pn* mantle refraction phase is observed to offsets of 350 km with strong amplitudes at many azimuths, and this implies that positive vertical velocity gradients with depth exist in the mantle. In addition, the amplitudes of the *Pn* phase are larger in the fast direction than in the slow direction, suggesting that the vertical velocity gradients vary with azimuth (e.g., Garmany, 1981). Azimuthally varying vertical velocity gradients are parameterized in the model as a sinusoidal variation over 90 degrees (i.e., $\cos(2\theta)$) from a

maximum value in the fast direction to a minimum value in the slow direction. As described below, the maximum and minimum values are not determined within the inversion for anisotropic parameters, but instead are found through a grid search over many individual inversion results.

### 2.4.4 Delay times and inversion for anisotropy parameters

The delay time can be written as $dT = r/dV$, where $r$ is propagation distance. After applying the propagation correction to bring the data to a common mantle propagation distance of 75 km, $dV$ values were calculated from $dT$ by evaluating

$$dV_i = \left(\frac{dT_i}{r} + \frac{1}{V_0}\right)^{-1} - V_0 \tag{3}$$

where the subscript $i$ refers to the $i^{th}$ traveltime observation, $r$ is the reference mantle propagation distance (75 km), and $V_0$ is the isotropic mantle velocity to which we are comparing the traveltime data.

It has been shown that small azimuthal anisotropy in *P* wave velocity can be described by the functional form

$$dV \approx A + Bcos2\theta + Csin2\theta + Dcos4\theta + Esin4\theta \tag{4}$$

where $dV$ is the variation in velocity with respect to an isotropic model and the coefficients $A, B, C, D,$ and $E$ are functions of the elastic parameters of the material (Backus, 1965; Crampin, 1984). In matrix form, this can be written as

$$\overrightarrow{dV} = K\vec{m} \tag{5}$$

where $\overrightarrow{dV}$ is a column vector of velocity variations, $\vec{m}$ is a vector containing the coefficients of Equation (4), and $K$ is the Jacobian relating the model parameters to the velocity variations:

$$K = \left[\left(\vec{1}\right)\left(cos2\vec{\theta}\right)\left(sin2\vec{\theta}\right)\left(cos4\vec{\theta}\right)\left(sin4\vec{\theta}\right)\right] \tag{6}$$

where $\vec{\theta}$ is a column vector of source–receiver azimuths, and $K$ has 5 columns and $N$ rows for $N$ traveltime observations. Velocity variations $dV$ were fit to the model in Equation (4) using linear least squares.

Since a velocity model is used to calculate the propagation correction, if the velocity model obtained by the inversion (Equation (4)) differs from the model used to correct the data, the model obtained from inversion is no longer consistent with the data. We therefore used an iterative approach to refine the velocity model until a self-consistent model was obtained. Beginning with the piecewise bin velocity model, the procedure for iteration was as follows: (1) calculate the mean velocity from the current velocity model to use as the isotropic reference for the mantle, (2) find the fast-direction azimuth for the current velocity model to set the phase of the gradient model, (3) calculate the propagation correction and delay times using the current velocity model, gradients, and isotropic reference, (4) calculate $dV$ and invert for a new velocity model. This process was repeated using successive refinements of the velocity model until the model parameters did not appreciably change with subsequent iterations. The parameters changed very little after 5 iterations, and 10 iterations were completed to ensure convergence of the model.

Four separate inversion results, based on all of the traveltime data, are shown in Figure 2-5. The largest difference between these models is between 5a and 5b, where propagation corrections were made using the bin velocities in both cases but static corrections are applied only in 5b, resulting in a substantially better fit to the data. The models in 5a and 5b do not include iteration, so they are not self-consistent in the sense that the mantle velocities used to make the propagation corrections differ from the mantle velocities resulting from the inversion. The model in 5c results from 10 iterations where propagation corrections are iteratively refined and the inversion is repeated until a self-consistent model is obtained. This reduces the percent anisotropy from 6.6% to 6.5% and increases the RMSE from 65 ms to 67 ms. Models in 5a-c are inversion results using the parameterization without gradients. The model in 5d includes azimuthally varying vertical velocity gradients. The fit of this model, with RMSE of 65 ms, is improved over 5c, and the model has a lower anisotropy at the Moho of 6.3%.

The models shown in 5b-d are quite similar, both visually and quantitatively. The similarity between 5b and 5c reflects how close the bin velocity model is to the continuous model obtained by inversion. Although incorporating the gradient parameterization does not result in significant changes in 5d compared to 5c, systematic variation in *Pn* amplitudes with azimuth suggests that the gradient parameterization is a better representation of the velocity structure. The choice of gradient values is discussed further in the next section.

### 2.4.5 Vertical velocity gradients

Vertical velocity gradients were estimated using a grid-search over the two values that we use to parameterize the azimuthal variation of velocity gradient: the gradients in the fast and slow directions. We performed a complete inversion, from initial tracing with the bin velocities through successive iterative refinement, for pairs of fast- and slow-direction gradients over a grid. RMSE was calculated for each inversion, and the preferred pair of gradient values was chosen based on the minimum RMSE.

Results of the grid-search used to determine the preferred gradient parameters are summarized in Figure 2-6. Our preferred gradient model has gradients of 0.02 km/s/km in the fast direction and 0 km/s/km in the slow direction. The absolute minimum RMSE is found for a slow-direction gradient of 0.01 km/s/km, with an RMSE value 0.002 milliseconds lower than that of the preferred model. However, synthetic tests discussed in the next section showed that the NoMelt data distribution can only weakly resolve the slow-direction gradient, so this was not considered sufficient evidence for a strong slow-direction gradient. Further, the low amplitudes of *Pn* arrivals along the slow direction (Figure 2-3) support a much smaller gradient in the slow direction compared to the fast direction. We note that the raytracing methods used here cannot test the feasibility of a small negative gradient for the slow direction, although this is not ruled out by the data. The inclusion of gradients in the inversion of the NoMelt data decorrelates the residuals with offset (Figure 2-7), though the effect is small. The interpretation of the inverted anisotropy is different for the model parameterizations with and without gradients. In the no-gradient models (Figures 2-5a–c), the inverted anisotropy is averaged over the depth range that the *Pn* phase traveled. For the gradient parameterization (Figure 2-5d), the percent anisotropy applies to the very top of the mantle, and the

value is smaller than the no-gradient cases in Figure 2-5 and Figure 2-8, below. Our preferred gradient model implies an increase in anisotropy with depth.

### 2.4.6 Inversion sensitivity tests

The accuracy of the inversion method was tested using synthetic traveltimes. The synthetic data were generated by raytracing a set of offsets and azimuths through a prescribed anisotropic velocity model and adding 10 ms of random normal error. Synthetic datasets were first generated for a perfectly even distribution of offsets and azimuths. Iterative inversion of the synthetics recovered the percent anisotropy within 0.04% of the generating model, the isotropic velocity within 0.01 km/s, and the fast-direction azimuth within 0.07°N. To test the effects of the uneven data distribution, synthetic traveltimes were next generated with offsets and azimuths distributed as in the NoMelt dataset. The unevenly distributed synthetic data did an equally good job of recovering all aspects of the generating model as the perfectly distributed synthetic data had. This indicates that there were sufficient data to avoid bias due to the distribution of offsets and azimuths assuming that the errors in the data are normally distributed.

While our inversion approach relies on isotropic raytracing along particular azimuths to approximate traveltimes for an anisotropic medium, this is not expected to introduce significant errors into the calculations. Using isotropic raytracing, as opposed to anisotropic raytracing, is equivalent to assuming that the effect of transverse motion due to anisotropy is small, and previous studies have demonstrated that the effect is small for *P*-wave traveltimes (Shearer & Orcutt, 1985).

Synthetic traveltime data were also used to test how well the data could resolve gradients. Synthetics were generated using an anisotropic model with known velocity gradients and with the same azimuths and offsets as the real dataset. The synthetic traveltimes were then inverted using the same method as the real data and the gradient values were gridsearched as described in Section 2.5. The RMSE was higher and the residuals were strongly correlated with source–receiver offset for models where the gradients imposed in the inversion process differed from those used to generate the synthetics (Figure 2-7). The minimum RMSE for the synthetics corresponds to the correct gradient model, showing that RMSE can be used as an indicator for gradients, but the constraints on the slow direction gradient are much weaker than the constraints for the fast direction. This is likely

because of the large range of offsets and large quantity of data available near the fast direction azimuth which is not matched for the slow direction.

While synthetic tests indicate that the distribution of data is sufficient to recover anisotropy parameters and constrain gradients in the case of normally distributed errors, the azimuthal patterns in the residuals illustrated in Figure 2-5 suggests that the data contain systematic errors. Such errors might arise if a swath of *Pn* arrivals has been picked systematically too early or late over successive shots, or if a broad region of the crust or mantle violates our assumption of 1D velocity structure. We tested for bias due to non-1D structure by averaging the static- and propagation-corrected NoMelt data into 15° bins and inverting the bin averages with weights corresponding to the standard deviation of $dV$ in each bin (Figures 2-8a, b). Since the data within a given bin come from a variety of OBS and have sampled the crust and mantle over different regions, this averaging tends to smooth out non-1D effects and, if those effects are large, the weighting damps out their effect on the inversion. Binning also reduces the weight of the most populous bins along L02. The model obtained from the binned data is very similar to that obtained from the full inversion, with 6.3% anisotropy for the binned no-gradient parameterization versus 6.5% for the un-binned data, and 6.1% anisotropy for the binned gradient case versus 6.3% for the un-binned data. While the results of the binned fits suggest that lateral variations in crust or mantle velocity structure could be present, we believe that the influence of such features is small. Since the data near any given azimuth come from a variety of source–receiver pairs that will not generally have similar travel paths, systematic variations in crust or mantle structure should be averaged out in the 1D model. Further, the traveltime residuals do not show any coherent spatial trends indicative of systematic changes in crust or mantle structure across the portion of the NoMelt site considered in this study.

For both parameterizations, the fast direction in the binned data inversions is rotated one degree to 83°N relative to the 82°N fast direction found with the un-binned data. We tested whether this rotation was due primarily to sampling bias towards data from L02 azimuths by down-weighting only the data along L02 azimuths in the inversion. Data weights were determined by the ratio of the median number of picks in non-L02 azimuthal bins to the numbers of picks along L02 azimuths. The weighting factors for L02 picks were on the order of 0.05, while non-L02 picks were given weights of 1. Inverting all of the data using this weighting scheme resulted in a fast direction along

83°N and slightly weaker anisotropy of 6.3% (Figure 2-8c) versus 6.5% (Figure 2-5c) for the unweighted inversion. This suggests that the sampling bias towards data along L02 azimuths does influence inversions using all of the traveltime picks when weights are not applied, yielding a slightly higher percent anisotropy and a rotation of the fast direction one degree closer to the azimuth of L02. The mean velocity was the same in all inversions.

When a grid-search for gradient parameters is performed using the weighted inversion, the minimum RMSE is obtained with a larger fast-direction gradient of 0.027 km/s/km compared to 0.02 km/s/km when the data are not weighted. The RMSE minimum is also less well-defined for the inversion of the weighted data than for the inversion of unweighted data, demonstrating that the data along L02 azimuths are the primary source of the constraint on the fast-direction gradient. This difference in the value of the preferred fast-direction gradient could be due to the relaxation of constraints provided by the deepest raypaths when the long-offset data along L02 are down-weighted.

We also test for the influence of the $4\theta$ terms of Equation (2) on the inversion. All of the final models (Figures 2-5c, 5d, 8a-d) have non-zero coefficients for the $4\theta$ terms, and these coefficients are an order of magnitude smaller than those of the $2\theta$ terms (Table 2-1). We tested the influence of the $4\theta$ terms on the inversion result by inverting the full, unweighted dataset while holding each of the $4\theta$ coefficients fixed. The results of a suite of such constrained inversions show that the $4\theta$ terms have a significant effect on both the strength of anisotropy obtained in the inversion and the orientation of the fast direction (Figure 2-9). When both $4\theta$ coefficients are set to zero and the traveltime data are fit with only $2\theta$ variation, the velocity in the slow direction drops and the strength of anisotropy increases from 6.3% to 6.8%, demonstrating that the $4\theta$ terms are important to the overall fit of the NoMelt data even though the coefficients are small. Several previous studies fit only for $2\theta$ coefficients because the $4\theta$ terms are generally small. Our analysis suggests that such a choice leads to less accurate results. The $4\theta$ terms are related to elastic parameters, and so setting them to zero imposes a constraint on the velocity structure of the medium that is not necessarily justified.

### 2.4.7 Final model

The six models shown in Figures 2-5c, 5d, and 8a-d all fit the traveltime observations well. Models 5c, 8a, and 8c differ from 5d, 8b, and 8d in their gradient parameterization. While the gradient parameterization used for 5d, 8b, and 8d is more realistic and justifiable than the parameterization without gradients, models 5c, 8a, and 8c have value as simple and useful models that accurately characterize the average anisotropy of the upper several kilometers of a 1D mantle. The models shown in Figure 2-5 use all of the individual traveltimes, whereas the models in Figures 2-8a and 8b are based on averages of data within 15° bins, and those in Figures 2-8c and 8d are based on weighted data with points along L02 azimuths down-weighted relative to the rest of the data. The models based on bin averages smooth out effects related to systematic data errors, while the models based on all of the data individually may be a more accurate representation of the Earth, despite some systematic misfits to the data indicated by trends in the residuals. The same fast-direction azimuth is obtained for all the models in Figure 2-8, suggesting that down-weighting data along L02 effectively mitigates bias in the fast direction estimate without requiring full binning of the data.

Our preferred model is shown in Figure 2-8d. It is a fit to data that have been corrected in a self-consistent manner, and it includes a parameterization of vertical velocity gradients that we believe is more realistic than a mantle with zero vertical velocity gradients. The inclusion of gradients reduces the RMSE of the model relative to the parameterization without gradients, and also de-correlates the residuals with offset. This anisotropy model is based on the inversion of weighted data, with points along L02 azimuths down-weighted to minimize the biasing effects of data along L02, combined with gradients determined by inversion of the full dataset. The gradient model therefore makes use of the information provided by data along L02 to better constrain the fast-direction gradient. This model has 6.0% azimuthal anisotropy in P wave velocities at the Moho, with a mean velocity of 8.13 km/s, a fast-direction vertical velocity gradient of 0.02 km/s/km and a slow-direction gradient of 0 km/s/km. The fast-direction azimuth of 83°/263°N is normal to magnetic anomalies (Barckhausen et al., 2013). Based on the range of models obtained by the different weighting and binning schemes, and on our tests with synthetic data, we estimate the uncertainty in the strength of anisotropy to be ± 0.3% and the uncertainty in the fast-direction azimuth to be ± 1°. The traveltime predictions from this model are in good agreement with the data (Figure 2-10).

The detailed characteristics of our preferred model and the five other models are provided in Table 2-1. These characteristics include calculated elements of the elastic tensor. For small azimuthal anisotropy, the square of the *P* wave velocity can be approximated by the same function form as the velocity variations:

$$V^2(\theta) \approx \hat{A} + \hat{B}\cos 2\theta + \hat{C}\sin 2\theta + \hat{D}\cos 2\theta + \hat{E}\sin 4\theta \qquad (7)$$

where $\hat{A}, \hat{B}, \hat{C}, \hat{D}$, and $\hat{E}$ are linear functions of the elastic parameters of the material (Backus, 1965; Crampin, 1984). The squared velocities of the final models were inverted to obtain $\hat{A}, \hat{B}, \hat{C}, \hat{D}$, and $\hat{E}$ coefficients. These coefficients uniquely determine four of the elastic parameters and place a constraint on two others (Table 2-1).

## 2.5 Discussion

Our measurement of azimuthal anisotropy and vertical velocity gradients in 70 Ma oceanic lithosphere at the NoMelt site provides estimates of the fast-direction orientation, strength, and depth gradients of anisotropy in the upper ~7 km of the oceanic mantle. These quantities reflect the dynamics of mantle deformation during lithospheric formation as well as processes involved in lithospheric evolution as the plate aged. The anisotropic structure at the NoMelt site is consistent with a simple model of mineral fabric formed by 2D corner flow and subsequent plate-driven shear at a mid-ocean ridge combined with some mechanism, such as the decreasing density of oriented cracks or joints with depth, that imparts an azimuthal variation in vertical velocity gradient. The NoMelt site was chosen owing to its uncomplicated tectonic history, and the mantle structure at this location is presumably indicative of a correspondingly uncomplicated mode of lithospheric formation at intermediate spreading rates. The NoMelt results thus provide a reference structure for comparison with results from lithosphere formed at different spreading rates or in more complex settings, where differences in anisotropic structure can then be interpreted to reflect differences in mantle dynamics.

### 2.5.1 Fast direction orientation

The fast direction of anisotropy from seismic studies is typically interpreted as representing a strong concentration of olivine *a* axes aligned by shear to parallel the azimuth of the major axis of the finite

strain ellipse (e.g., Hess, 1964; Nicolas & Christensen, 1987). While the orientation of the fast direction can also be affected by deformation history (e.g., Boneh et al., 2015; Boneh & Skemer, 2014), mineralogy (e.g., Mainprice et al., 2000), water content (e.g., Jung & Karato, 2001), melt (e.g., Holtzman et al., 2003), and other factors, broad agreement between models and observations for regions like the central Pacific (e.g., Becker et al., 2014) suggests that the fast direction at the NoMelt site can be interpreted in terms of strain associated with plate spreading. At the NoMelt site, we find the fast direction of anisotropy directed along 83/263°N, consistent with the presence of A-type olivine fabric formed by 2D mantle flow. The paleospreading direction at the center of the NoMelt array is estimated to be along 82°N based on local magnetic anomalies striking at 172°N (Barckhausen et al., 2013). We estimate an approximately 1° uncertainty in the fast-direction azimuth based on the range of fast azimuths from the six final models. Thus, within uncertainty, the measured fast azimuth coincides with the local paleospreading direction. This result suggests that this section of oceanic lithosphere experienced predominantly 2D mantle flow during its formation at the ridge.

The alignment of the fast and paleospreading directions at the NoMelt site is not particularly surprising; the NoMelt site was purposely located in the center of a wide, stable spreading segment where the lithosphere was likely to have experienced primarily 2D mantle flow. However, other active-source observations do not strongly support the expectation that fast and paleospreading directions are aligned. Many previous refraction-derived anisotropy measurements have found fast directions rotated several degrees away from the paleospreading direction, including a rotation of 13° near Hawaii (Morris et al., 1969), 17° near 45°N along the Mid-Atlantic Ridge (Keen & Tramontini, 1970), 17° off the coast of British Columbia (Keen & Barrett, 1971), 27° in the southwest Pacific (Shearer & Orcutt, 1985), and 15° in the western Pacific (Shintaku et al., 2014). In several studies, anisotropy initially characterized as spreading-parallel has later been recognized as skewed based on improved estimates of paleospreading directions (e.g., Morris et al., 1969; Shearer & Orcutt, 1985). While some of these previous studies suffer from poor data quality and/or lack of azimuthal coverage, the predominance in the literature of observations where the paleospreading and fast directions do not align suggests that mantle flow patterns at mid-ocean ridges may commonly be more complex than 2D corner flow, perhaps involving contributions from dynamic

flow in the asthenosphere that influence the formation of lithospheric fabric. For anisotropy measurements based on *Pn* traveltimes along a section of the East Pacific Rise near 9°N, the fast direction is rotated ~10° with respect to plate spreading (Toomey et al., 2007), and anisotropy measurements based on *Pn* phases and SKS splits around the Juan de Fuca ridge show a fast direction rotated by ~18° relative to the paleospreading direction (VanderBeek et al., 2016; VanderBeek & Toomey, 2017). These studies lead to speculation that this angular divergence represents a skewness between absolute plate motion (APM) and the plate-spreading direction. This could reflect a lag between changing asthenospheric flow and the plate-kinematic response, which may require changes in ridge segmentation (Toomey et al., 2007).

Plate reconstruction models (Seton et al., 2012) suggest that APM and paleospreading directions were not coincident when and where the NoMelt site was formed. However, our results suggest that deformation at this intermediate-rate ridge was dominated by 2D mantle flow associated with relative plate motion. Surface wave constraints on asthenospheric anisotropy at the NoMelt site also do not see a fast direction aligned with APM within the upper 300 km of the mantle (Lin et al., 2016). This has been interpreted as indicating that on a regional scale, spreading-derived CPO and dynamic flow in the asthenosphere dominate over fabric related to APM. The NoMelt results are consistent with estimates of fast direction orientation based on global surface wave tomography, which show close alignment of the fast and paleospreading directions for most Pacific lithosphere younger than 70 Ma (e.g., Becker et al., 2014). The surface wave results of Becker et al. (2014) do show large systematic differences in many other locations, including most of the Atlantic. The effects of non-2D mantle flow and other factors, such as melt supply and spreading rate, on lithospheric fabric could be evaluated in more detail by further comparisons of absolute plate motion and paleospreading directions using refraction-based measurements of anisotropy at particular locations.

### 2.5.2 Depth variation of anisotropy

The estimate of azimuthally varying vertical velocity gradients at the NoMelt site implies a depth variation in anisotropy. This depth variation could represent changes in intrinsic anisotropy related to mineral fabric, extrinsic anisotropy related to cracks or other aligned structures, or some

combination of both. The gradient estimate is pinned to a parameterization motivated by the observation that *Pn* amplitudes tend to decrease at azimuths away from the fast direction (Figures 2-3 and 2-10). However, the gradient estimate under this parameterization is based solely on traveltime misfit. Our efforts to include quantitative information on *Pn* amplitudes in the gradient estimation were complicated by the focusing and defocusing effects of seafloor structure which dominate the amplitude signal. Nevertheless, the basic observation of nonzero *Pn* amplitudes at all azimuths places some constraints on the mechanisms producing the estimated depth variation in anisotropy.

The most common interpretation of anisotropy in the uppermost oceanic mantle is as intrinsic anisotropy resulting from CPO of olivine imparted by shear strain. An interpretation of anisotropy solely in terms of CPO implies that the increase in the strength of anisotropy with depth corresponds to an increase in fabric strength with depth. Numerical models of corner flow do predict an increase in the strength of anisotropic fabric with depth in the shallow mantle (Blackman et al., 1996, 2017; Blackman & Kendall, 2002), but these models focus on asthenospheric anisotropy and do not resolve the details of fabric in the lithosphere.

While an increase in fabric strength is one possibility, azimuthal variation in vertical velocity gradients could also come from other sources. For example, fabrics other than olivine CPO may develop at mid-ocean ridges and impart intrinsic anisotropy. In particular, deformation experiments conducted on olivine aggregates with melt present (e.g., Hansen, Qi, et al., 2016, 4% melt; Qi et al., 2018, 7% melt) produce fabrics that appear to be a combination of CPO and shape-preferred orientation (SPO) (Hansen et al., 2014; Hansen, Qi, et al., 2016; Holtzman et al., 2003; Qi et al., 2018). At the much lower melt fractions typical of mid-ocean ridges, anisotropy due to this melt-present fabric is still likely to be dominated by the CPO component aligned in the shear direction, but the strength of effective seismic anisotropy may be reduced (Hansen, Qi, et al., 2016; Zhong et al., 2014). It is possible that this mechanism would impart vertical gradients in anisotropy if the percentage of melt present along a corner-flow flow line decreased for progressively deeper flow lines.

Extrinsic mechanisms such as cracks, joints, and vertical layering could also produce the observed change in anisotropy with depth. The closure of microcracks with increasing depth and pressure or, equivalently, a decrease in the occurrence of cracks with depth (e.g., Demartin et al., 2004), could

reasonably produce the observed positive vertical velocity gradients in the fast direction. Microcracks, if present, are expected to close within the depth range sampled in this study. The strength of anisotropy in our final model increases to ~7.7% at 7 km below the Moho, the maximum depth sampled by our data (Figure 2-11); this is close to the average *P* wave anisotropy estimated from olivine fabrics of ophiolite samples (8%), a value that does not include any effects from cracks (Ben Ismaïl & Mainprice, 1998). Laboratory measurements demonstrate crack closure pressures in dunite samples ranging from 250 to 750 MPa (Birch, 1960; Christensen, 1974; Greenfield & Graham, 1996), with most measurements below 400 MPa. Subtracting a hydrostatic pressure gradient from a lithostatic pressure gradient, we estimate an effective pressure of ~110 MPa at the Moho and ~265 MPa at 7 km below the Moho. This is within the range of experimentally determined crack closure pressures. The velocity gradient in the fast direction of the final model lies within the range of measurements of $V_p$ with pressure made on dunite samples compiled by Greenfield and Graham (1996) (Figure 2-11).

While the magnitude of the fast-direction gradient can be explained by the closure of randomly oriented microcracks, explaining the azimuthal variation of the velocity gradient with crack closure requires oriented cracks, which are expected to produce azimuthally varying velocities (e.g., D. L. Anderson et al., 1974; Nishizawa, 1982). Thin, water-filled, oriented cracks cannot explain the observations, since they introduce a $4\theta$ variation in velocity (e.g., Hudson, 1981), and the $4\theta$ terms in all of our models are small (Table 2-1). The observed gradients can be explained by "dry" oriented microcracks filled with damaged material and/or hydrous alteration products, which are predicted to produce a $2\theta$ velocity signal (Hudson, 1981; Thomsen, 1995). Assuming that the velocity at 7 km depth is representative of the uncracked solid, the velocity at the Moho in the fast direction can be accounted for with a dimensionless crack density of ~0.05 (e.g., Crampin et al., 1980; Garbin & Knopoff, 1973, 1975a, 1975b) where the crack density is defined as $\varepsilon = Na^3/v$ for $N$ cracks of radius $a$ in a volume $v$. Since cracks filled with hydrous minerals would not be expected to close, the crack density for filled cracks would need to decrease with depth. Under the assumption that the entire volume of the cracks is serpentinized, a crack density of 0.05 corresponds to ~0.5 wt% water in the uppermost few km of the mantle (Carlson & Miller, 2003). The oriented cracks would need to be aligned perpendicular to the paleospreading direction. This alignment would be consistent with the stress field experienced by the lithosphere near the ridge (Dunn, 2015), but horizontal

extensional stress due to thermal contraction may be at a maximum normal to the plate spreading direction at older ages (e.g., Sandwell & Fialko, 2004; Sasajima & Ito, 2017). Joints and other types of layering, such as spatial variation in the density of microcracks or gabbroic dikes (e.g., Francheteau et al., 1990; Hekinian et al., 1993), can also produce an extrinsic transverse isotropy for the wavelengths typical of active-source seismic experiments (e.g., Backus, 1962). Cracks or melt bodies localized into ridge-parallel structures could conceivably be generated by time-varying magmatism and thermal structure at a mid-ocean ridge.

While various kinds of extrinsic anisotropy may be present, they all involve important unknowns. Of the interpretations suggested here, the combination of corner flow and aligned microcracks seems the most plausible to us given what is known. Regardless of the mechanism, however, a key point to be noted from the gradient measurement is that the strength of anisotropy at 7 km below the Moho in the preferred model is estimated to be significantly higher than the depth-averaged strength of anisotropy estimated from the same data without the gradient parameterization. This suggests that information is being lost when anisotropy is inverted for using binned data, and that the maximum strength of anisotropy in the lithospheric mantle may be underestimated by studies where vertical gradients are not accounted for.

### 2.5.3 Using measurements of upper mantle anisotropy

Measurements of seismic anisotropy provide a means to learn about oceanic plate formation and mantle flow. This is possible because the evolution of lithospheric anisotropy is sensitive to a variety of factors including pre-existing mantle fabric (Boneh & Skemer, 2014; Skemer et al., 2012), the amount of strain the lithosphere experiences (e.g., N. Hedjazian & Kaminski, 2014; Ribe, 1992; Zhang & Karato, 1995), the magnitude of shear strain relative to the rate of rotation of the strain axes (Kaminski & Ribe, 2002), and the presence of melt during deformation (Hansen, Qi, et al., 2016; Qi et al., 2018). At the same time, this variety of sensitivities can make the interpretation of anisotropy difficult. Active source measurements of oceanic uppermost-mantle seismic anisotropy to date have provided estimates of fast-direction orientation and the strength of anisotropy, giving strong support for mantle flow accompanying plate separation at mid-ocean ridges. However, these results have not placed strong constraints on most of the factors that affect fabric development, so

many predictions that relate anisotropy to dynamic mid-ocean ridge processes (e.g., Blackman et al., 1996; Blackman & Kendall, 2002) remain untested.

The NoMelt results show that the addition of a constraint on the depth variation of anisotropy forces a consideration of multiple factors that impart seismic anisotropy, demonstrating a sensitivity to at least some of those factors. While our interpretation of these results is speculative, the sensitivity of the observations suggests a path forward. Differences in anisotropy, measured in a standard way, between oceanic lithosphere formed under different conditions can be used to infer variations in plate formation processes. Further, anisotropy measurements made at different ages within an otherwise relatively homogeneous segment can be used to understand how a plate evolves as it ages and, in particular, how the lithosphere responds to thermal contraction. Results from the NoMelt site provide a useful reference for this type of comparative study.

### 2.6 Conclusions

We have measured 6.0 ± 0.3% anisotropy at the Moho and azimuthally varying vertical velocity gradients in the upper 7 km of the mantle at the NoMelt site in the central Pacific. The fast direction is oriented parallel to paleospreading within an uncertainty of ± 1°, consistent with predictions for olivine fabric formed by 2D mid-ocean ridge corner flow. Our preferred gradient model, which varies azimuthally between 0.02 km/s/km in the fast direction and 0 km/s/km in the slow direction, implies that effective anisotropy increases with depth, reaching a value of 7.7% at 7 km below the Moho. We interpret the increase in anisotropy with depth as reflecting the diminishing influence of an extrinsic anisotropy that is orthogonal to the intrinsic anisotropy, as opposed to intrinsic anisotropy increasing as a function of depth. The extrinsic anisotropy can be explained by some form of organized or aligned cracks closing or otherwise decreasing in density with depth.

This study demonstrates the value of comprehensive azimuthal coverage, controls on shallow structure, and long source–receiver offsets for measuring anisotropy with depth constraints. The constraint on vertical velocity gradients enables us to consider multiple factors that affect the formation and evolution of the lithospheric mantle. Constraints on shallow structure are key to estimating gradients, as deterministic static corrections based on NoMelt MCS and swath bathymetry data provide a reduction in residuals that is on the order of the delay-time signal of

anisotropy. This measurement of anisotropy in 70-Myr-old lithosphere formed at an intermediate-to-fast spreading rate can serve as a reference for comparative studies of lithospheric formation and evolution.

### 2.7 Acknowledgments and Data

We thank the Captain and crew of the R/V *Marcus G. Langseth* and the engineers and technicians from the Scripps Institution of Oceanography and the Woods Hole Oceanographic Institution, who provided instruments through the National Science Foundation's Ocean Bottom Seismograph Instrument Pool (OBSIP). The professionalism and expertise of these individuals were key to the success of this experiment. We also thank Donna Blackman, Tom Brocher, Philip Skemer, and an anonymous reviewer for their thoughtful comments which greatly improved this paper. The OBS data described here are archived at the IRIS Data Management Center (http://www.iris.edu) under network code ZA 2011-2013. The travel time picks are archived in the Marine-Geo Digital Library (http://www.marine-geo.org/library/) with the DOI 10.1594/IEDA/324643. This work was supported by NSF grant OCE-0928663 to D. Lizarralde, J. Collins, and R. Evans; NSF grant OCE-0927172 to G. Hirth; NSF grant OCE-0928270 to J. Gaherty; and an NSF Graduate Research Fellowship to H. Mark.

## 2.8 Figures and tables

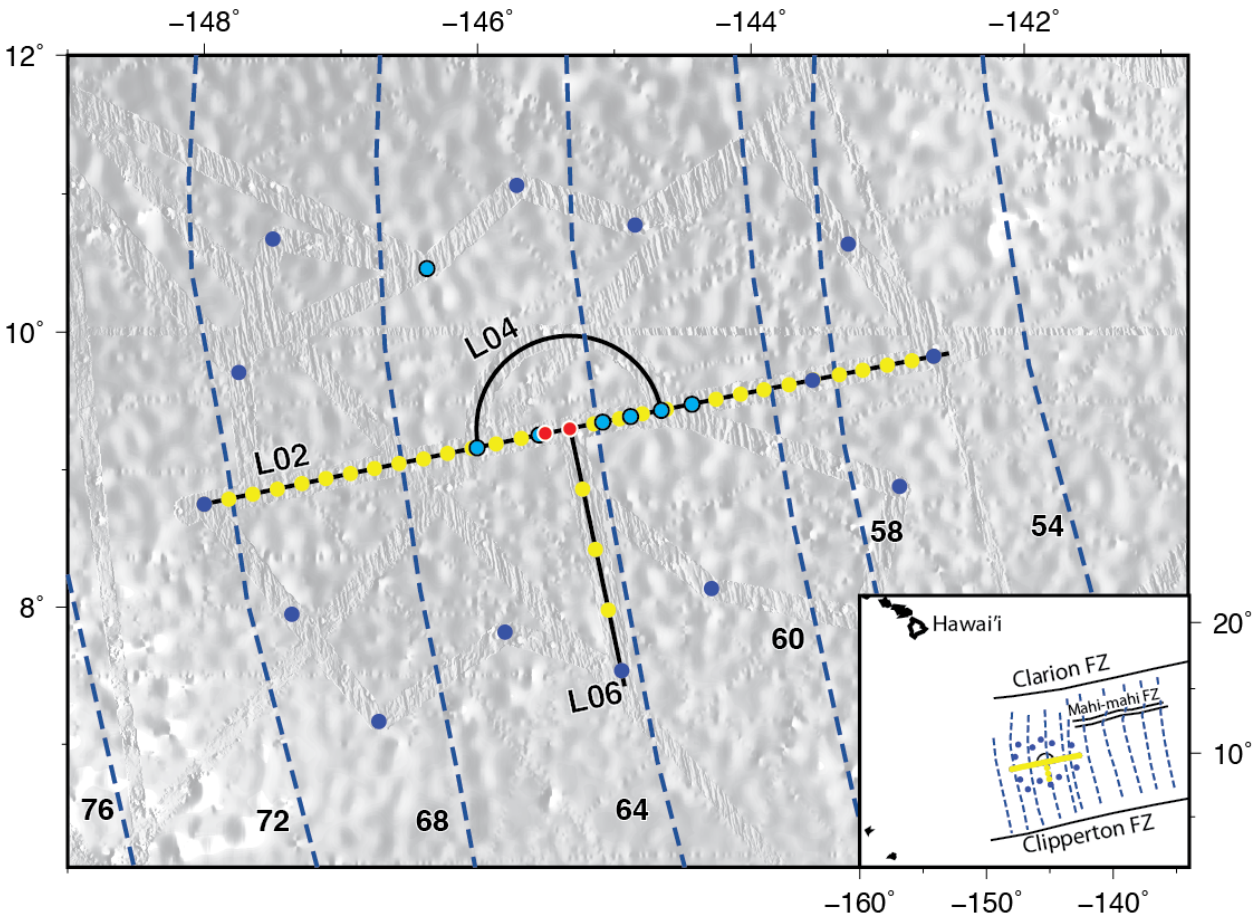


**Figure 2-1.** Map of the central Pacific showing the NoMelt array. Short-period (SP) OBS are marked by yellow dots, broadband (BB) OBS by blue dots. Lighter blue dots outlined in black indicate BB instruments used in this study. SP OBS A15 and BB OBS B14 (Figs. 2-3, 2-10) are marked by red dots outlined in white. Shotlines are in black: L02 runs nearly East-West, L06 runs nearly North-South, and L04 is a semicircle near the center of the array. Dashed light blue lines show isochrons from Barckhausen et al. (2013) and the bathymetry is from GMRT v3.4 (Ryan et al., 2009). The inset map shows the location of the array within the Pacific. The study site is located between the Clarion and Clipperton fracture zones, approximately 1500 km southeast of Hawai'i.

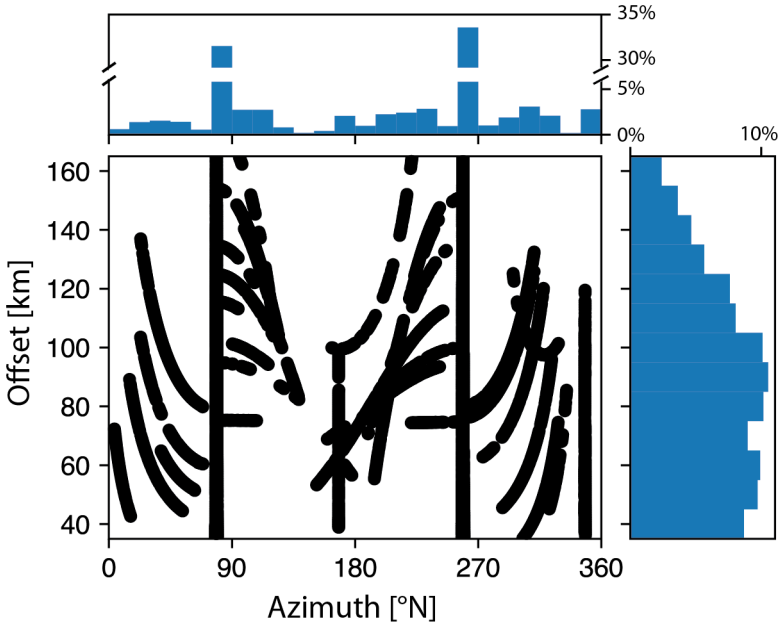


**Figure 2-2.** Distributions of source–receiver offset and azimuth for the 7,961 traveltime picks (black) used in the analyses. Histograms show the uneven distribution of azimuths (top) and the more uniform distribution of offset (right) in the dataset.

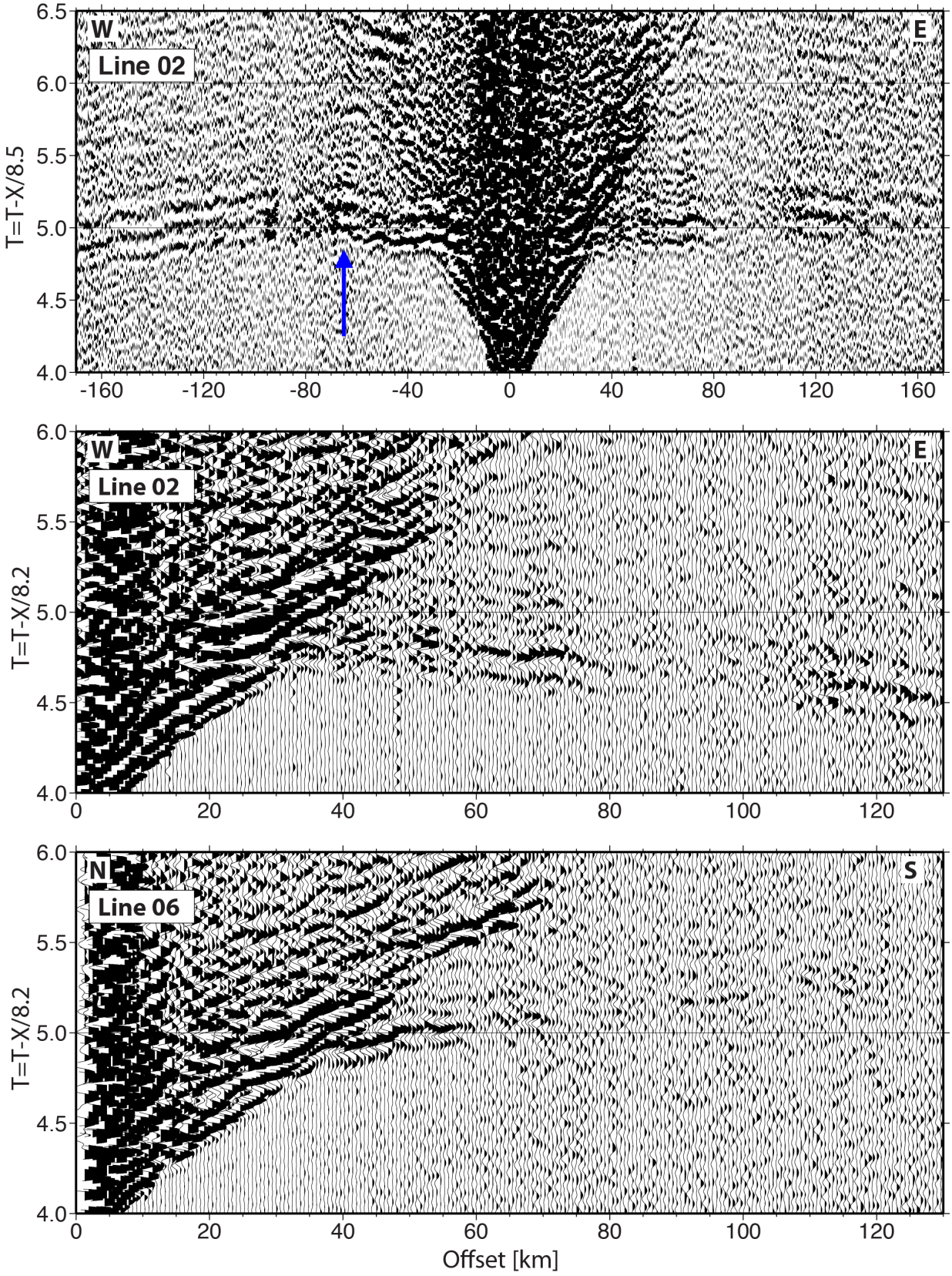
W
Line 02
E
T=T-X/8.5
6.5
6.0
5.5
5.0
4.5
4.0
-160
-120
-80
-40
0
40
80
120
160
W
Line 02
E
T=T-X/8.2
6.0
5.5
5.0
4.5
4.0
0
20
40
60
80
100
120
N
Line 06
S
T=T-X/8.2
6.0
5.5
5.0
4.5
4.0
0
20
40
60
80
100
120
Offset [km]

**Figure 2-3.** Record sections corrected for variable water depth and sediment thickness for BB OBS B14, located at the crossing of Line 02 and Line 06. Data from shots along Line 02 is shown in the top two panels; the bottom panel shows data from shots along Line 06. A blue arrow in the top panel indicates the transition to faster phase velocities 180 km from the western end of Line 02. The horizontal phase velocity of *Pn* is observed to be greater than 8.2 km/s along Line 02, the flow-line direction, and slower than 8.2 km/s perpendicular to the flow line along Line 06.

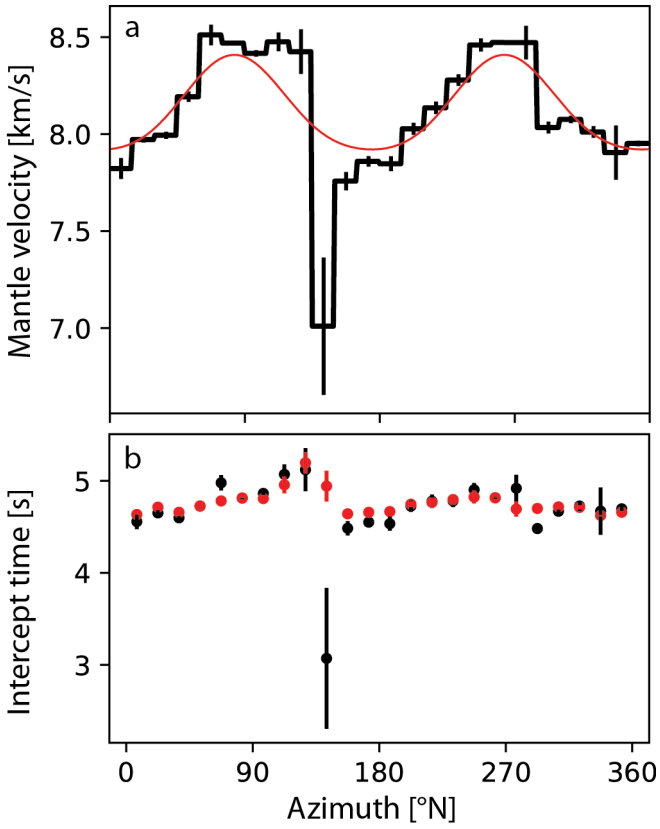


**Figure 2-4. (a)** Bin velocities used for the initial iteration of the joint propagation correction and model inversion (black) and the final model obtained after the iterations converged (red). Black bars show the 95% confidence intervals for the bin velocities. The anomalous bin velocity near 140°N is due to a sparsely populated bin with only 16 picks constraining the linear fit. **(b)** Intercept times from the initial bin velocity model (black), and intercept times calculated from the final model, which has a constant crustal thickness (red). The close agreement between these intercept times indicates that the variation in intercept times is primarily due to the mantle anisotropy and that crustal thickness variations throughout the NoMelt region are small.

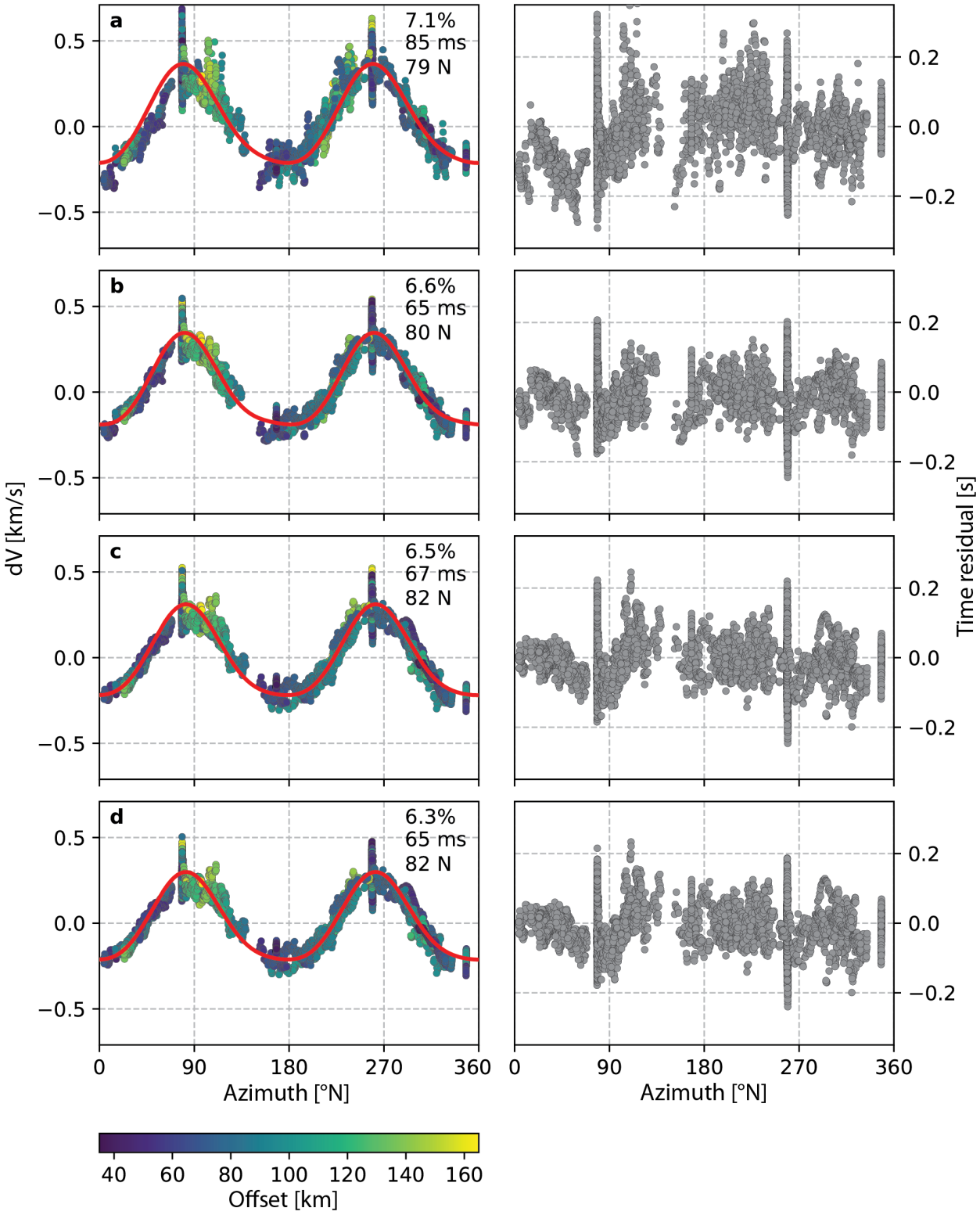
a
7.1%
85 ms
79 N
b
6.6%
65 ms
80 N
c
6.5%
67 ms
82 N
d
6.3%
65 ms
82 N
dV [km/s]
Time residual [s]
Azimuth [°N]
Azimuth [°N]
Offset [km]

**Figure 2-5.** Inversion result (red line) and fitted data (left column, dots colored by source–receiver offset) with corresponding percent anisotropy, RMSE, and fast direction azimuth (upper right corners), and residuals (right column). **(a)** Inversion with no statics, propagation correction using only the bin velocity model, and no gradients; **(b)** as in (a) but including static corrections; **(c)** with statics, ten iterations on the propagation corrections, and no gradients; and **(d)** with statics, ten iterations, and the preferred gradient model. See text for discussion.

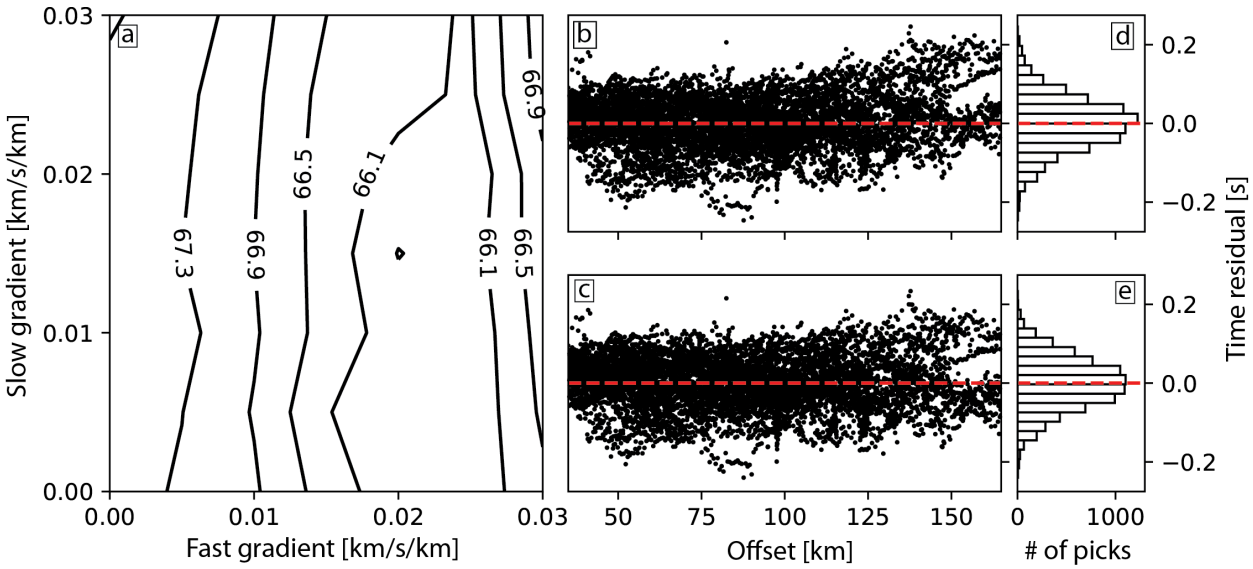


**Figure 2-6. (a)** Contours of RMSE in milliseconds for inversions of the NoMelt traveltime data with different gradient models show a sensitivity to vertical velocity gradient, with greater sensitivity to the fast-direction gradient than the slow, similar to what is seen with the synthetic data in Fig. 7. Our preferred model has a gradient of 0.02 km/s/km in the fast direction and 0 km/s/km in the slow direction. **(b)** Residuals from the model in Figure 5c, an inversion without gradients, show a slight correlation with offset, particularly for large offsets. **(c)** Residuals from the model in Figure 5d, inverted with the preferred gradient model, are flattened out at large offsets compared to (b). (**d, e)** Histograms show the distribution of time residuals for the two cases highlighted in (b) and (c).

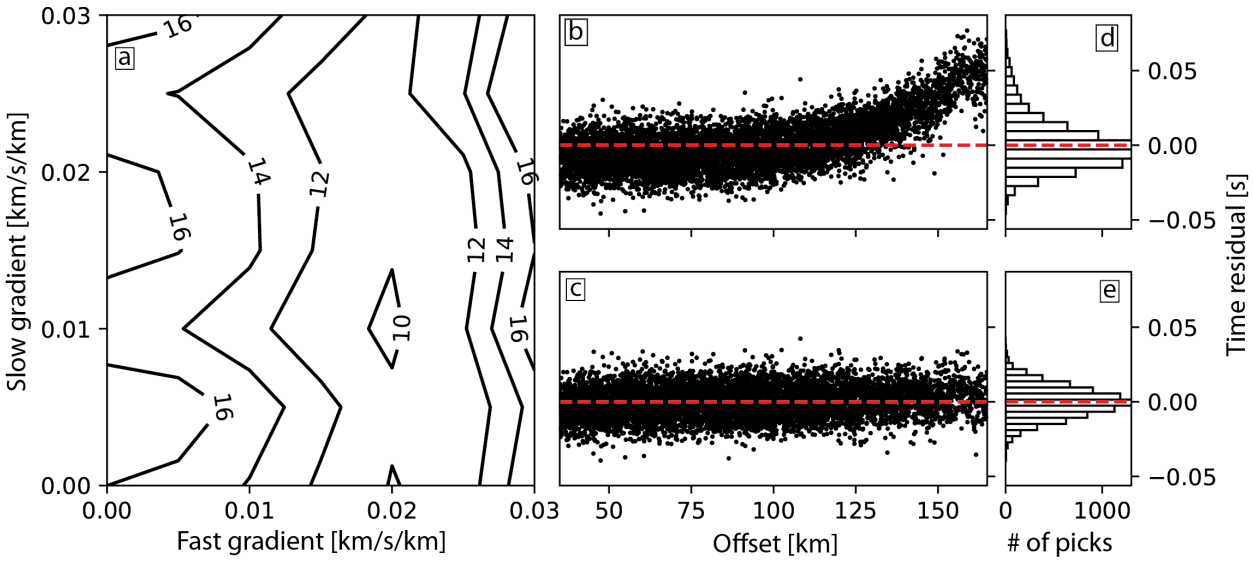


**Figure 2-7.** For synthetic data, generated using a velocity model with a 0.02 km/s/km gradient in the fast direction and 0 km/s/km in the slow direction, **(a)** contours of RMSE for inversions with different gradient models (i.e. fast/slow pairs) show that the gradient model is well resolved in the fast direction, but is more ambiguous in the slow direction. **(b)** Inverting without gradients leads to a correlation of the residuals with offset. **(c)** When the same synthetic traveltimes are inverted with the true gradient model, the offset correlation disappears. **(d, e)** Histograms show the distribution of time residuals for the two gradient cases highlighted in b and c.

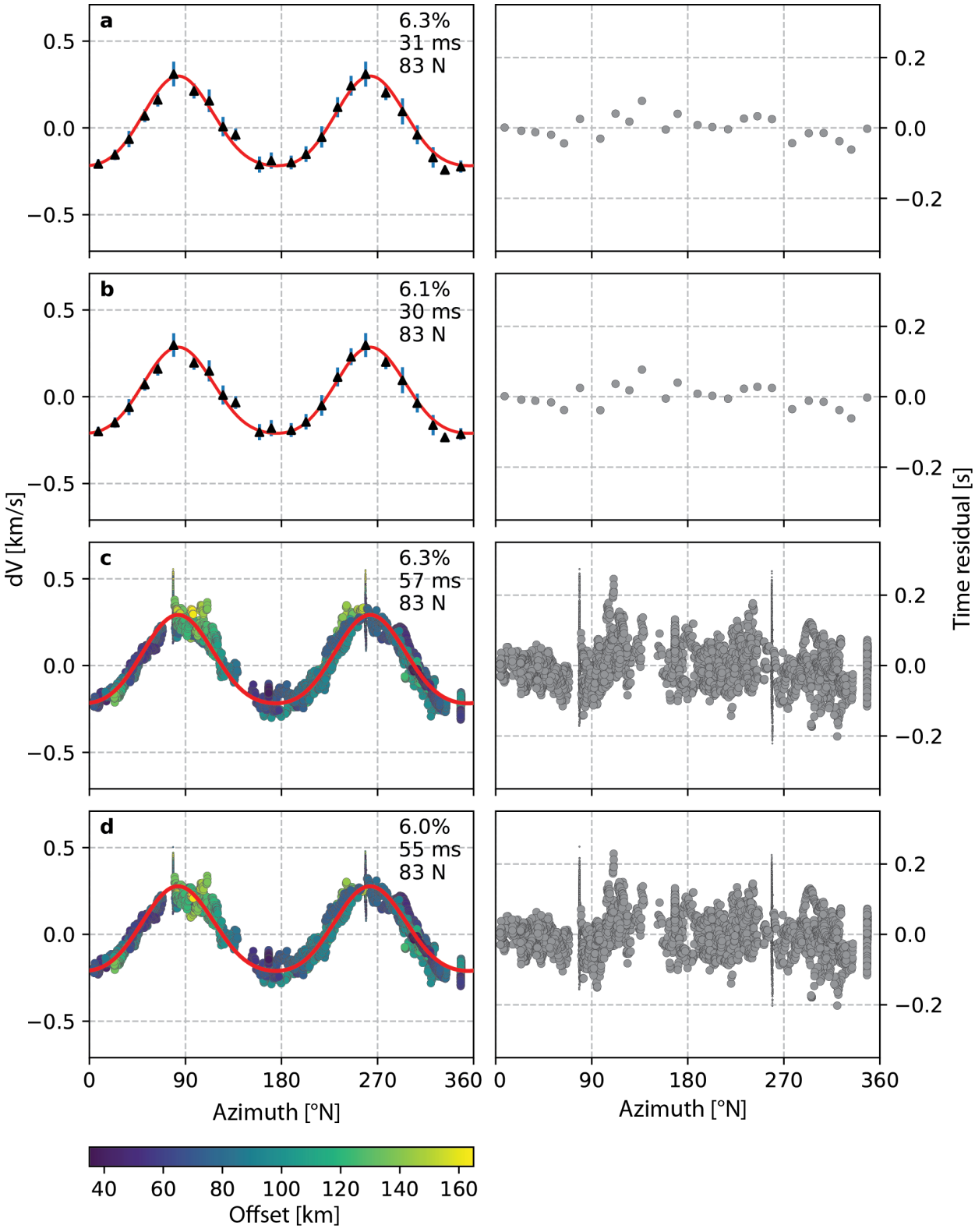
a
6.3%
31 ms
83 N
b
6.1%
30 ms
83 N
c
6.3%
57 ms
83 N
d
6.0%
55 ms
83 N
dV [km/s]
Time residual [s]
Azimuth [°N]
Azimuth [°N]
Offset [km]
40 60 80 100 120 140 160
0 90 180 270 360
0 90 180 270 360
0.5 0.0 −0.5
0.2 0.0 −0.2

**Figure 2-8. (a)** Inversion results for the NoMelt traveltime data with data averaged into 15° bins after the application of static and propagation corrections, including 10 iterations and no gradients; **(b)** as in (a) but with the preferred gradient model. **(c)** Inversion results for all of the NoMelt traveltime data and using data weights in the inversion as described in the text. Weights are indicated by the size of plotted points. This model includes 10 iterations and no gradients. **(d)** As in (c) but with the preferred gradient model.

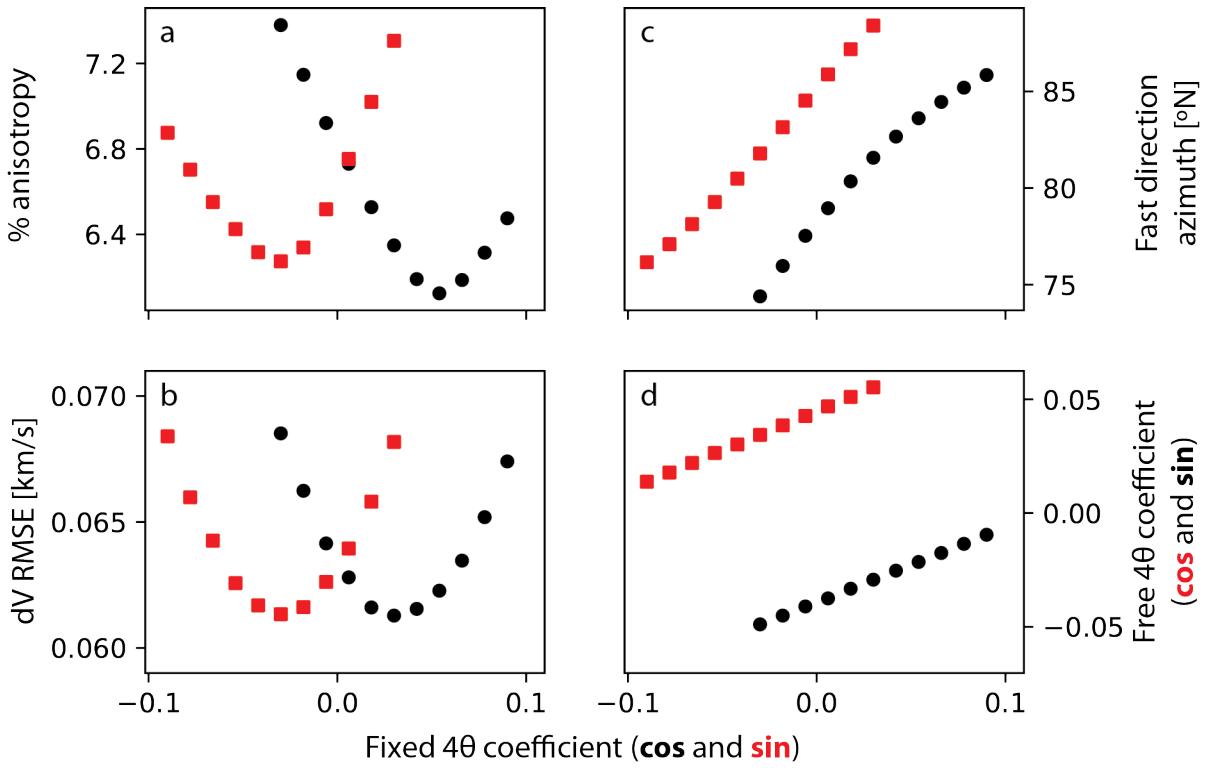


**Figure 2-9.** Velocity models were fit with each of the two $4\theta$ coefficients held constant at different values. Panels show the value of the fixed cosine (black circles) and sine (red squares) $4\theta$ coefficients versus **(a)** percent anisotropy; **(b)** RMSE of the velocity variation $dV$; **(c)** fast-direction azimuth; and **(d)** value for the free $4\theta$ coefficient.

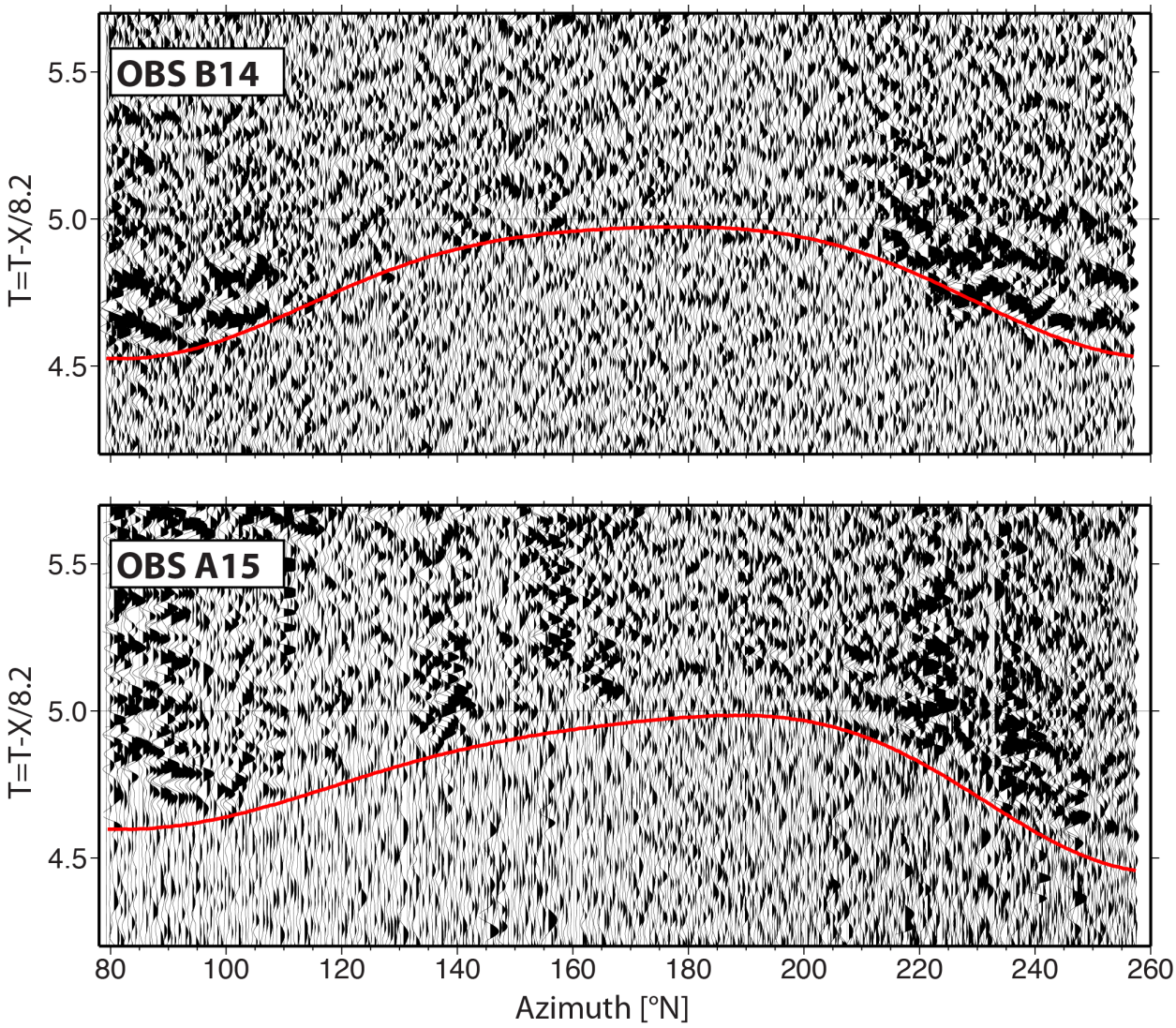


**Figure 2-10.** L04 data from OBS B14 and A15 shows good agreement between *Pn* first arrivals and arrival times predicted by our preferred anisotropic velocity model (red lines).

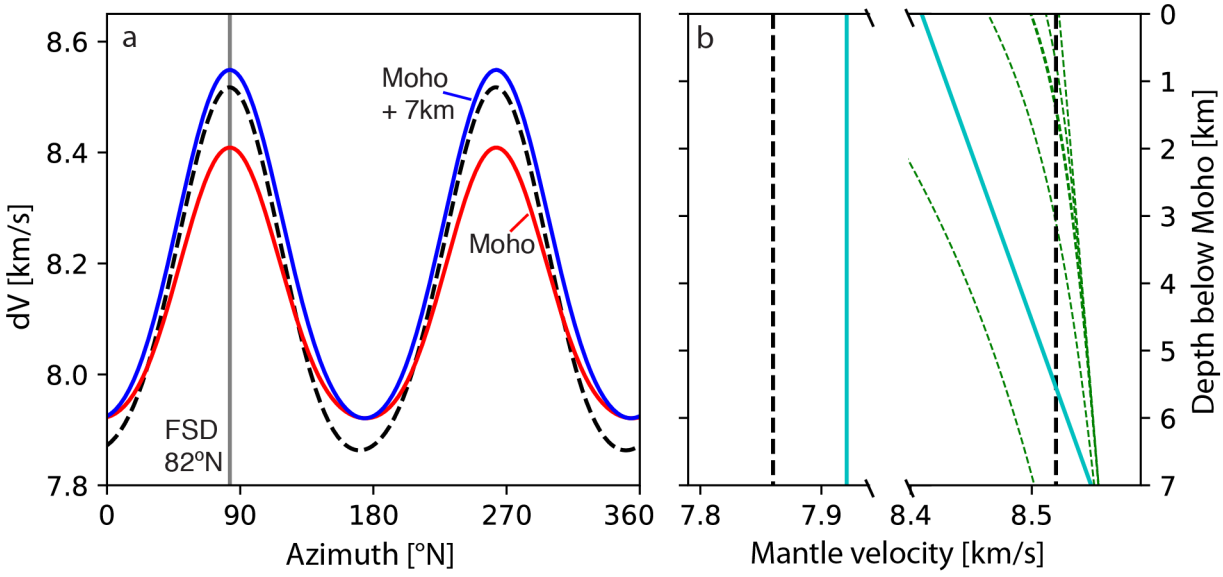


**Figure 2-11. (a)** The final model is shown at the Moho (red line) and 7 km below the Moho (blue line). An average model from ophiolite fabrics is shown for comparison (dashed black line) (Ben Ismaïl & Mainprice, 1998). The fossil spreading direction, 82°N, is marked by a grey line. **(b)** The velocities in the fast and slow directions are shown versus depth below the Moho for the final model (cyan) and an average ophiolite model (dashed black). Dotted green lines show predicted velocity variation due to crack closure in dunite samples based on experimentally measured parameters compiled in Table 4 of Greenfield and Graham (1996) and calculated using Equation 2 of that paper.

| | Anisotropy parameters | | Elasticity parameters | | | |
|---|---|---|---|---|---|---|
| | | | (km/s) | | (GPa) | |
| All data, no gradients (Figure 2-5c) | Mean $V_P$ (km/s) | 8.14 | A | 0.000 | $C_{11}$ | 207.30 |
| | % anisotropy | 6.5% | B | -0.257 | $C_{22}$ | 235.03 |
| | Azimuth of max $V_P$ (°N) | 82/262 | C | 0.063 | $C_{16}$ | 0.10 |
| | Fast gradient (km/s/km) | 0.0 | D | 0.038 | $C_{26}$ | 3.29 |
| | Slow gradient (km/s/km) | 0.0 | E | -0.028 | $C_{12} + 2C_{66}$ | 212.57 |
| All data, with gradients (Figure 2-5d) | Mean $V_P$ (km/s) | 8.14 | A | 0.000 | $C_{11}$ | 207.29 |
| | % anisotropy | 6.3% | B | -0.247 | $C_{22}$ | 233.94 |
| | Azimuth of max $V_P$ (°N) | 82/262 | C | 0.060 | $C_{16}$ | 0.07 |
| | Fast gradient (km/s/km) | 0.02 | D | 0.035 | $C_{26}$ | 3.18 |
| | Slow gradient (km/s/km) | 0.0 | E | -0.028 | $C_{12} + 2C_{66}$ | 212.66 |
| Binned data, no gradients (Figure 2-8a) | Mean $V_P$ (km/s) | 8.14 | A | 0.000 | $C_{11}$ | 207.29 |
| | % anisotropy | 6.3% | B | -0.252 | $C_{22}$ | 234.99 |
| | Azimuth of max $V_P$ (°N) | 83/263 | C | 0.057 | $C_{16}$ | 0.12 |
| | Fast gradient (km/s/km) | 0.0 | D | 0.035 | $C_{26}$ | 3.30 |
| | Slow gradient (km/s/km) | 0.0 | E | -0.020 | $C_{12} + 2C_{66}$ | 212.60 |
| Binned data, with gradients (Figure 2-8b) | Mean $V_P$ (km/s) | 8.14 | A | 0.000 | $C_{11}$ | 207.27 |
| | % anisotropy | 6.1% | B | -0.242 | $C_{22}$ | 233.88 |
| | Azimuth of max $V_P$ (°N) | 83/263 | C | 0.054 | $C_{16}$ | 0.08 |
| | Fast gradient (km/s/km) | 0.02 | D | 0.033 | $C_{26}$ | 3.21 |
| | Slow gradient (km/s/km) | 0.0 | E | -0.019 | $C_{12} + 2C_{66}$ | 212.73 |
| Weighted data, no gradients (Figure 2-8c) | Mean $V_P$ (km/s) | 8.14 | A | 0.000 | $C_{11}$ | 207.18 |
| | % anisotropy | 6.3% | B | -0.248 | $C_{22}$ | 233.90 |
| | Azimuth of max $V_P$ (°N) | 83/263 | C | 0.058 | $C_{16}$ | 0.53 |
| | Fast gradient (km/s/km) | 0.0 | D | 0.032 | $C_{26}$ | 2.61 |
| | Slow gradient (km/s/km) | 0.0 | E | -0.018 | $C_{12} + 2C_{66}$ | 213.22 |
| Weighted data, with gradients (Figure 2-8d) | Mean $V_P$ (km/s) | 8.13 | A | 0.000 | $C_{11}$ | 207.15 |
| | % anisotropy | 6.0% | B | -0.238 | $C_{22}$ | 232.71 |
| | Azimuth of max $V_P$ (°N) | 83/263 | C | 0.056 | $C_{16}$ | 0.53 |
| | Fast gradient (km/s/km) | 0.02 | D | 0.029 | $C_{26}$ | 2.47 |
| | Slow gradient (km/s/km) | 0.0 | E | -0.017 | $C_{12} + 2C_{66}$ | 213.39 |

**Table 2-1.** Parameters for anisotropy and elasticity obtained in this study. Coefficients A, B, C, D, and E correspond to Equation (4).

# Chapter 3

# Constraints on the depth, thickness, and strength of the G discontinuity in the central Pacific from S receiver functions

This chapter is being prepared for publication as: Mark, H. F., Collins, J. A., Lizarralde, D., Hirth, G., Gaherty, J. D., and Evans, R. L. Constraints on the depth, thickness, and strength of the G discontinuity in the central Pacific from S receiver functions.

### 3.1 Abstract

The relative motion of the lithosphere with respect to the asthenosphere implies the existence of a boundary zone that accommodates shear between the rigid plates and flowing mantle. This shear zone is typically referred to as the lithosphere-asthenosphere boundary (LAB), and its sharpness and physical mechanism have important implications for coupling between mantle convection and surface plate motion. Seismic observations have provided evidence for several physical mechanisms that might help enable relative plate motion, but how these mechanisms each contribute to the overall accommodation of shear remains unclear. Here we present receiver function constraints on the discontinuity structure of the oceanic upper mantle at the NoMelt site in the central Pacific, where local constraints on shear velocity, anisotropy, conductivity, and attenuation through the upper 300 km of the mantle provide a comprehensive picture of upper mantle structure. We image a seismic discontinuity at 50-55 km depth corresponding to a <5% drop in Vsv over 10-20 km. We interpret this feature as the Gutenberg discontinuity (G), and find that G is best explained by the presence of a dehydration boundary based on combined constraints from the receiver functions and the local conductivity model. The top of the discontinuity is shallower than a change in the strength and orientation of azimuthal anisotropy, suggesting that relative motion across the transition from lithosphere to asthenosphere is distributed over an interval that includes G and continues past the discontinuity to greater depths.

### 3.2 Introduction

Observations of surface plate motions and changes in seismic anisotropy in the upper mantle indicate that the lithosphere moves relative to the underlying asthenospheric mantle (e.g., Becker, 2008; Conrad et al., 2007; Savage, 1999; Solomon & Sleep, 1974; Wilson, 1965). This implies the existence of a transition where the shear strain between the rigid plate and flowing mantle is accommodated over some depth range. The transition is often referred to as the lithosphere-asthenosphere boundary (LAB), but whether it is actually a sharp, boundary-like feature or is instead a broader, more diffuse zone of deformation is not well understood (e.g., Fischer et al., 2010). The sharpness of the transition, and the physical changes occurring across it, have implications for coupling between the plates and the convecting mantle and, as a result, for the wavelength of mantle convection and the balance of forces that drive plate tectonics (e.g., Ghosh et al., 2008; Höink et al., 2011; Lenardic et al., 2006; Richards et al., 2001; Richards & Lenardic, 2018).

Several physical mechanisms have been proposed to explain the rheological transition from the lithosphere to the asthenosphere, but no single factor is able to explain all the relevant observations of the upper mantle. The primary factors thought to contribute to the rheological contrast are temperature, composition, and melt. Temperature strongly influences viscosity, and tomography models of the oceanic upper mantle show a broad gradient from fast seismic velocities in the shallow mantle to slower velocities in the asthenosphere which deepens with plate age and is thought to represent the effects of plate cooling (e.g., Beghein et al., 2014). However, the temperature dependence of rock properties cannot explain all seismic observations of the lithosphere (Faul & Jackson, 2005; Jackson et al., 2002; Stixrude & Lithgow-Bertelloni, 2005). In particular, thermal gradients are not sharp enough to produce the abrupt changes in seismic velocities, or seismic discontinuities, observed in the upper mantle (e.g., Fischer et al., 2010). Mantle composition also influences viscosity, and compositional gradients are expected within the upper mantle due to melting and melt extraction at mid-ocean ridges (Hirth & Kohlstedt, 1996; Phipps Morgan, 1997). Strong gradients in mantle water content could explain observations of seismic discontinuities at roughly constant depths in the oceanic upper mantle, which are too sharp to be explained by thermal gradients. Discontinuities observed at 50-100 km depth beneath the oceans are often referred to as the Gutenberg, or G, discontinuity (Gutenberg, 1959). However, these

discontinuity observations are spatially heterogeneous, and some studies have suggested that the depth of G varies with plate age (e.g., Schmerr, 2012; Tharimena et al., 2017), in contrast to the predictions for compositional gradients established during plate formation. The presence of melt can reduce mantle viscosity, and horizontal melt-rich layers at the base of the lithosphere could facilitate plate motion and explain discontinuity observations (Hammond & Humphreys, 2000; Kawakatsu et al., 2009; Rychert et al., 2018; Schmerr, 2012). However, melt is not expected to be stable beneath old, cold oceanic lithosphere far from the ridge axis although seismic discontinuities are still observed in these regions.

The NoMelt experiment offers an exceptional opportunity to address questions related to the structure of the oceanic upper mantle and the nature of the lithosphere-asthenosphere transition by providing multiple types of high-resolution geophysical data at a single location. The experiment deployed an array ocean bottom seismometers (OBS) and magnetotelluric (MT) instruments in the center of a stable spreading segment in the Pacific where the plate is ~70 Myr old and appears to have a simple tectonic history. Data from NoMelt have been used to constrain local shear velocity, azimuthal anisotropy, attenuation, and electrical conductivity through the shallow upper mantle (Lin et al., 2016; Ma et al., 2018; Matsuno & Evans, 2017; Russell et al., 2019; Sarafian et al., 2015). Smooth models for Vs and azimuthal anisotropy at the site agree well with tomographic models.

This study uses OBS receiver functions to constrain the upper mantle discontinuity structure at the NoMelt site. The receiver functions indicate that a discontinuity is present beneath the NoMelt array as a velocity decrease of <5% over >10 km starting at 50-55 km depth. We interpret this feature as the G discontinuity. The conductivity structure for the NoMelt site is not consistent with the presence of melt, indicating that G does not represent melt accumulation (Matsuno & Evans, 2017; Sarafian et al., 2015). The discontinuity could be explained by a dehydration boundary, the presence of which is also supported by the local conductivity structure (Sarafian et al., 2015). Changes in the strength and orientation of azimuthal anisotropy from local surface wave models appear to occur deeper than the top of the discontinuity imaged by receiver functions (Lin et al., 2016), although gradients in mineral fabric could still contribute to the observed discontinuity. The change in viscosity across a dehydration boundary could help to localize shear between the lithosphere and asthenosphere (e.g., Hirth & Kohlstedt, 1996; Karato, 2012), but azimuthal anisotropy measured at

the NoMelt site suggests that shear strain accommodation continues below the G discontinuity (Lin et al., 2016).

### 3.3 Methods

We image the seismic G discontinuity beneath the NoMelt array in the central Pacific using *S*-to-*p* receiver functions calculated from OBS records. After inspecting the data for quality, the receiver functions are calculated using the extended-time multitaper method (Helffrich, 2006; Park et al., 1987; Park & Levin, 2000; Shibutani et al., 2008). The receiver functions are corrected for moveout using velocity models based on local models for the NoMelt site (Lin et al., 2016; Lizarralde et al., 2018; Russell et al., 2019) and the PA5 model for a corridor in the western Pacific (Gaherty et al., 1996). After correcting for moveout with respect to a reference distance of 70°, the traces are stacked. Synthetic receiver functions are calculated in the same manner from reflectivity synthetic seismograms using a set of velocity models spanning a parameter space where the depth, thickness, and strength of G are varied. We extract two quantitative parameters from each receiver function stack: the time of the G conversion peak, and the width of the G peak in seconds. The parameters extracted from the receiver function stacks for the data are compared to predictions from the synthetic receiver function stacks, and the comparisons are used to estimate parameters for G beneath the NoMelt array.

#### 3.3.1 Geophysical context from NoMelt

The NoMelt experiment aimed to characterize the detailed seismic and electrical structure of the oceanic lithosphere-asthenosphere system in the central Pacific at a location where the plate does not appear to have experienced any substantial tectonic or magmatic disturbance since its formation. The experiment was conducted in the middle of a stable spreading segment between the Clarion and Clipperton fracture zones, where the plate is ~70 Myr old (Barckhausen et al., 2013). The experiment consisted of a ~1 year deployment of 26 broadband OBS and eight magnetotelluric instruments in the central Pacific, along with the acquisition of active-source seismic refraction and reflection data using 31 short-period OBS and a 6 km multi-channel streamer.

Data from NoMelt have been used to constrain the smooth seismic and electrical structure down to ~300 km beneath the instrument array. Surface waves have been used to infer local *S* velocity structure through the asthenosphere (Figure 3-1a, b, c, d) (Lin et al., 2016; Russell et al., 2019). The overall structure resembles regional models, with a high-velocity lid overlying a low-velocity zone (LVZ). Changes in the strength and orientation of azimuthal anisotropy with depth suggest that shallow fabric is locked into the lithosphere during plate spreading, and secondary convection or pressure gradient-driven return flow modify mineral fabric within the asthenosphere (Lin et al., 2016). Models for the electrical structure at the NoMelt site based on magnetotelluric data show a resistive lid ~60-80 km thick overlying more conductive mantle (Figure 3-1e) (Matsuno & Evans, 2017; Sarafian et al., 2015). This can be explained by a change in water content from a dry lid to an underlying region with greater hydrogen saturation within nominally anhydrous olivine, and it is inconsistent with the presence of interconnected melt beneath the lid. The attenuation structure derived from long-period Rayleigh waves crossing the NoMelt array can be modeled using two layers, with low attenuation ($Q > 300$) at shallow depths transitioning to high attenuation ($Q \sim 100$) past 50-100 km (Ma et al., 2018).

### 3.3.2 Data selection

During the NoMelt broadband OBS deployment, 28 circum-Pacific earthquakes occurred that meet our selection criteria of $M_W \geq 6.5$ and ranges between 50 and 90 degrees from the OBS array (Figure 3-2). The 50-90° range is suitable for *S*-to-*p* receiver functions targeting shallow upper mantle structure (Yuan et al., 2006). Terrestrial receiver function studies are often able to use events with magnitudes lower than $M_W$ 6.5 (e.g., Hopper et al., 2014), but larger events are needed for OBS studies to overcome microseismic noise in the submarine environment. The horizontal components of the seismograms are rotated to radial and transverse orientations.

The data are bandpass filtered to 4-35 seconds (0.0286-0.25 Hz). This passband is chosen to exclude most long-period noise from infragravity waves, tilt, and compliance, and to attenuate short-period microseismic noise, while retaining earthquake energy over a broad enough band for the receiver function deconvolution process to work. Visual inspection of the filtered seismograms reveals clear direct *P* and *S* phases for the majority of the events (Figure 3-3). Traces with no clear direct *S* arrival visible near the time predicted by the global velocity model *ak135* are excluded from subsequent

analyses. After quality control, we retain data for 204 station-event pairs from 19 events and 15 stations. The direct *S* arrival times are then picked by hand from the radial component.

### 3.3.3 Receiver function calculation

We calculate *S* receiver functions using the extended-time multitaper method (Helffrich, 2006; Park et al., 1987; Park & Levin, 2000; Shibutani et al., 2008). *S* receiver functions take advantage of the fact that the converted *p* phase from a discontinuity arrives at a seismic station before the parent *S,* so the converted phase is not mixed with reverberations in the coda of the direct phase as is often the case with *P* receiver functions for shallow discontinuities. The extended-time multitaper method windows the time-series data with a set of Slepian tapers before transformation to the frequency domain to obtain noise-resistant spectral estimates. Using overlapping windows for the spectral estimate produces receiver functions that preserve amplitudes for arbitrarily long time series (Helffrich, 2006; Park et al., 1987). We use 3 prolate eigentapers, a time-bandwidth product of 4, a taper length of 25 seconds, and 75% window overlap for the receiver function calculation (Shibutani et al., 2008). Before applying the tapers, the data are rotated from ZRT into LQT coordinates to separate upgoing *SV* (Q) from *P* (L). The Q component is trimmed to 20 seconds before and 30 seconds after the direct *S* arrival, and the L component is trimmed to 90 seconds before and 30 seconds after.

A moveout correction is applied to the receiver functions before stacking to correct for the fact that converted phase arrival times depend on epicentral distance. The moveout correction is referenced to an epicentral distance of 70°, and it is calculated using a velocity model with a set discontinuity structure. The choice of the moveout velocity model is discussed in Section 3.3.6.

### 3.3.4 Synthetic resolution tests

Synthetic tests demonstrate that individual receiver functions and sparse stacks are affected by earthquake source parameters and station geometry, but robust inferences about the presence of upper mantle discontinuities can be made based on stacks with a sufficiently large number of traces (~200 or more). We calculate and analyze receiver functions from reflectivity synthetic seismograms using models of increasing complexity to illustrate how event moment tensors, source-station back

azimuth, epicentral distance, and the presence or absence of a G discontinuity influence both individual receiver functions and stacks (Figure 3-6). For these synthetic cases, the moveout velocity model corresponds to the known velocity model used to calculate the synthetic seismograms (Figure 3-4).

A clear signal from the G discontinuity can be seen in receiver function stacks when effects from source and station parameters are minimized, and when the synthetics are calculated over a relatively wide frequency band. This is demonstrated by a set of synthetic receiver functions calculated for a velocity model with a G discontinuity present at 60 km depth, using a single moment tensor and back azimuth for all traces and filtering to ~1.4-35 seconds (0.029-0.7 Hz) (Figure 3-6a). This set of synthetics can be thought of as an ideal scenario, since the actual data require filtering to a narrower band to avoid contamination from the primary microseism peak. The source-station ranges for the synthetics match those in the OBS data, yielding a set of 204 traces. A negative lobe is present in the stack of all traces at the time expected for a conversion from G. The strength of the signal from G decays with epicentral distance from ~55-75°. This expected, as the transmission coefficient for a converted *Sp* phase decreases significantly with increasing epicentral distance (Figure 3-5). Traces near ~80° show an anomalously strong and broad negative peak, indicating that individual traces or small numbers of traces are not reliable indicators of upper mantle structure. However, these anomalous traces do not dominate the stack, and the G peak in the stack is fairly sharp. The G peak in the stack sits between the Moho side lobe, a filtering artifact visible at ~3.5 seconds before direct S, and a low-amplitude negative part of the receiver function past ~10 seconds (Figure 3-6a).

The receiver function stack still shows a peak at the time predicted for the conversion from the G discontinuity for synthetics filtered to the narrower frequency band required for the observations (4-35 seconds, 0.029-0.25 Hz), (Figure 3-6b). The G peak in the receiver function stack is slightly less sharp than the high-frequency case (Figure 3-6a). In particular, the G peak is less distinct from the excess negative part of the receiver function past ~10 seconds, although the amplitude and the width of the main peak are similar. This demonstrates that the shape of the negative lobe in the receiver functions is influenced by the filter and the frequency band as well as the particular model for upper mantle structure.

The strength of the signal from G in the synthetic receiver functions varies with epicentral distance, with most of the energy coming from 65-75°. This contrasts with calculated *S*-to-*p* transmission coefficients, which predict that the G conversion should be strongest near 55° and amplitudes should monotonically decay with epicentral distance (Figure 3-5). The weak signal in the 55-65° range could be due to interference from crustal phases, which can be observed in the synthetic seismograms and may obscure the *Sp* phase in some offset ranges. There are also more traces from 65-75° in the data set than from 55-65° (Figure 3-6g), so the weaker signal at shorter distances could indicate that noise is not being stacked out as effectively in the more sparsely populated distance bins.

Repeating the synthetic seismogram calculation for a velocity model with no G discontinuity results in a receiver function stack with no significant negative peak (Figure 3-6c). This supports the conclusion that the feature seen in the stack of traces from the model with G present is not a false positive (Figure 3-6b). While the stacked traces from the no-G model are moveout-corrected using a model with G at 60 km depth, inspection of the receiver functions before applying the moveout correction shows that slight shifts of the moveout trajectory corresponding to different G depths would also not align a coherent signal.

Adding further details of source and station parameters changes individual synthetic receiver functions but does not obscure the signal from G in the stack. We incorporate the back azimuths from the observations (Figure 3-6d) and the moment tensors (Figure 3-6e), and the negative peak corresponding to the G conversion is still clearly present in stacks. This demonstrates that it is possible to extract a signal from G even when earthquake source parameters and station geometry are not uniform.

The observed receiver functions show a negative lobe in the overall stack that we interpret as coming from a conversion at the G discontinuity (Figure 3-6f), and the observations are broadly similar to the synthetics that include all available source and station parameters (Figure 3-6e). As with the synthetics, individual receiver function traces from the observations are not clearly diagnostic of upper mantle structure (Figure 3-7). However, the moveout-corrected stack of the

observations has a large negative lobe near the time expected for a conversion from a shallow upper mantle discontinuity. The time and width of the negative lobe are discussed in detail in Section 3.4.

Bootstrap stacks of synthetic receiver functions indicate that the 204 traces in the data set can provide a reasonable proxy for the arrival time of the *S*-to-*p* converted phase from G, but the uncertainty associated with the G peak time measured from a given receiver function stack is non-negligible for this quantity of data. For the synthetics, the time of the negative lobe corresponding to G approaches the predicted time for the G conversion as the number of traces in the stack increases (Figure 3-8). For bootstrap stacks of 30 traces, a negative lobe in the stack may be more than 0.6 seconds off from the predicted time for the G conversion, while for subsamples of 180 traces, the time of the negative lobe is within ~0.2 seconds of the predicted time. The uncertainty in the time of the G conversion due to sample size is incorporated into subsequent analyses using jackknife resampling.

### 3.3.5 Quantifying the effects of upper mantle structure on receiver function stacks

We quantify the relationships between features of receiver function stacks and the depth, thickness, and strength of G for a suite of 1D velocity models and corresponding synthetic receiver function stacks. The velocity models are based on a combination of local constraints from other analyses of NoMelt data (Lin et al., 2016; Lizarralde et al., 2018; Russell et al., 2019) and regional models for Pacific seismic structure (Gaherty et al., 1996). We vary the depth, strength, and thickness of the G discontinuity while holding the crustal structure constant, and generate a suite of 168 velocity models spanning a parameter space where the top of G is at 50-80 km depth, the thickness of the discontinuity is between 0 and 20 km, and the velocity drop at G is between 3.4 and 8.6% for Vsv. The velocity gradient between the Moho and G varies with the strength of G. The ranges for the depth and strength of G were chosen based on previous observations of G (e.g., Collins, 2002; Gaherty et al., 1996; Kawakatsu et al., 2009; Kumar & Kawakatsu, 2011; Tan & Helmberger, 2007), and the maximum thickness of 20 km was chosen based on the limits of resolution for *S*-to-*p* receiver functions (Rychert et al., 2007). For each of the 168 velocity models in this parameter space, we calculate a set of synthetic seismograms and corresponding receiver functions that mimic the observations in terms of back azimuths, epicentral distances, and moment tensors (one example is shown in Figure 3-6e). Each set of synthetic receiver functions is stacked using the generating

velocity model for the moveout correction, and the velocity model is also used to calculate a prediction for when the G conversion arrives relative to the direct *S* phase. We refer to these synthetics, where the same velocity model is used both to generate the synthetic seismograms and to perform the moveout correction for the synthetic receiver functions, as "matched" cases.

The receiver function stack for each velocity model is analyzed to extract two main features of the stack: the time of the maximum amplitude of the G conversion peak relative to the direct *S* arrival time, and the width of the G peak in seconds. The G peak time is picked as the local minimum of the receiver function within a time window around where the G conversion is expected to arrive. The G peak width is estimated by fitting a Gaussian to the identified G peak. For synthetic receiver function stacks, the fits to the G peaks are reasonable and the full width at tenth maximum (FWTM) provides a good estimate of total peak width (Figure 3-9a, b).

The depth, thickness, and strength of G all influence both the time and the width of the G peak extracted from the synthetic receiver function stacks. The strongest relationships between G parameters and G peak features are shown in Figure 3-10. The time of the G peak relative to the direct *S* arrival scales with the depth and thickness of the G discontinuity in the velocity model (Figure 3-10a, b). The G peak is earlier for cases where the G discontinuity is deeper and thicker, and the effect of depth is stronger than the effect of transition thickness. A given G peak time can be explained by several different models, with trade-offs between the depth and thickness of G: a deeper and thinner discontinuity can result in the same G peak time as a shallower and thicker discontinuity (Figure 3-10b). The G peak time does not perfectly match the time predicted by raytracing for most cases (Figure 3-10a). This is likely due to the filtering process, as the time of the G peak tends to be closer to the predicted time when the synthetics are calculated at higher frequencies and filtered to a wider band. We proceed with the narrower filter band since it is needed to deal with microseismic noise present in the OBS data, and note that even though the predicted times are not perfectly accurate, they are within ~1 second of the G peak time for all synthetic cases. The width of the G peak varies inversely with the strength of G, and the range of variation is larger for deeper discontinuities (Figure 3-10c). Peak width is also expected to scale with the thickness of G (Rychert et al., 2007).

Many receiver function studies seek to match the shape of receiver functions through forward-modeling (e.g., Byrnes et al., 2015; Olugboji et al., 2016); in contrast, we limit our analysis to two discrete quantities, the time and width of the G peak. We do not attempt to match the overall shape of the G peak because the synthetics showed that the shape of the peak depends on a variety of factors besides the discontinuity parameters (Figure 3-6a, b). Further, the suite of matched synthetics shown in Figure 3-10 demonstrates that the two quantities extracted from the stacks are sufficiently sensitive to the depth, thickness, and strength of G to provide useful bounds on those discontinuity parameters.

### 3.3.6 Recovering G parameters from receiver function stacks

The relationships between receiver function stack features and G parameters for matched synthetic cases described in Section 3.3.5 can be used to estimate G parameters from receiver function stacks when the discontinuity structure is not known. This is done for a set of receiver functions using a gridsearch method over a parameter space where the depth, thickness, and strength of G are varied. The process of estimating G parameters from a set of receiver functions is demonstrated for two representative synthetic cases in Figure 3-11. In each case, we take synthetic receiver functions from a single, known velocity model and calculate moveout corrections and corresponding receiver function stacks for 168 velocity models where G is at 50-80 km depth and corresponds to a 3.4-8.6% drop in Vsv over 0-20 km. We refer to the set of receiver function stacks for all the velocity models as a "mismatched" set, since all but one of the stacks use a model for the moveout correction that does not match the generating model. Each stack in the mismatched set is analyzed and compared to the predictions from matched cases (Figure 3-10), and these comparisons are used to determine which velocity models in the parameter space could explain the synthetics.

In the first case (Figure 3-11a, b, c), synthetic seismograms are calculated for a model where the G discontinuity sits at 55 km depth and corresponds to a 5.2% drop in Vsv over 5 km. From these synthetic seismograms, we calculate a mismatched set of 168 receiver function stacks, and measure the time and relative amplitude of the G peak in each stack. The uncertainty associated with the measured time of the G peak in each stack is estimated by stacking the receiver functions using jackknife resampling. The time of the G peak in the stacks is stable regardless of the model used for moveout because we pin the moveout correction to a 70° epicentral distance, and most of the traces

in the stack are at ranges close to 70° (Figure 3-11a). However, the difference between the measured G time and the time predicted by raytracing varies across models.

The matched synthetics indicate that the G peak should be within 1 second of the predicted time (Figure 3-10a), so velocity models where that criterion is not met are considered unable to explain the receiver functions (shaded regions in Figure 3-11a). The G peak time is thus constrained to the range of times from models where the measured and predicted G times are no more than 1 second apart. For this synthetic case, the range of G peak times is 7.11-7.45 s before the direct *S* arrival. The set of viable models is further narrowed down by comparing this range of times to the matched synthetic cases. G peak times between 7.11 and 7.45 s before the direct *S* correspond to a G depth of 50-59 km and a G thickness of 0-13 km from the matched synthetic cases (Figures 3-10b, 3-11b).

The G peak width decreases with increasing strength of G for the matched synthetic cases, but increases with G strength for the subset of mismatched cases that are able to explain the measured G time. We constrain the strength of G based on the intersections of these opposite trends, giving a Vsv drop of >5.2% (Figures 3-10c, 3-11c).

By applying these successive constraints, we obtain a final set of velocity models within our parameter space where the predictions for both the time and relative amplitude of the G peak match the values measured for synthetic stacks within uncertainty. We estimate that the top of G is between 50 and 59 km depth, and the discontinuity corresponds to a Vsv of 5.2% or more over 0-13 km thickness. These bounds include the generating model, which had G at 55 km with 5 km thickness and a 5.2% Vsv drop, thus showing that we are able to recover the parameters for G within uncertainty. Notably, the constraint on the strength of G is weak, the true value is barely within the bounds of the estimate. The constraints on the G parameters are interdependent because estimating three G parameters based on two values extracted from the receiver function stacks is an underdetermined problem.

The process of estimating G parameters is demonstrated for a second set of synthetic seismograms calculated using a model where G starts at 75 km depth, and Vsv drops by 4.3% over 10 km down to 85 km (Figure 3-11d, e, f). The range of G peak times in the mismatched set of stacks is 9.75-10.4 s before the direct *S* arrival, which is wider than in the previous case. This is likely related to the fact

that the G in the generating model is a gradient over 10 km, as thicker G discontinuities are expected to produce wider negative lobes from the G conversion in stacks (Rychert et al., 2007). The top of G is estimated to be between 69 and 80 km with a thickness of 0-20 km and a Vsv drop of 4-6.4%. These bounds include the generating model.

### 3.4 Results

We analyze the OBS data using the procedure outlined in Section 3.3.6 with one modification. For stacks of the observations, the G peak is less regular in shape than in the synthetics and inspection of the Gaussian fits shows that they tend to be wider than the G peak. The full width at half maximum (FWHM) is therefore used to estimate peak width for the observations in order to exclude both the small negative tail of the G peak and part of the negative lobe adjacent to the Moho conversion (Figure 3-9c). Part of the negative lobe adjacent to the positive peak from the Moho is likely due to the Moho side lobe, a small negative peak that appears in receiver functions as a result of the filtering process. While the side lobe is clearly visible in the synthetics, it is not distinct from the G peak in the observations. However, a change in the slope of the negative lobe on the side adjacent to the Moho peak suggests a contribution from the side lobe which must be accounted for in measuring the G peak width (Figure 3-9c).

Using successive constraints based on comparing the observed receiver function stacks to the matched synthetics, we estimate that the top of the G discontinuity is at 50-64 km depth, corresponding to a <5.4% drop in Vsv over 0-20 km (Figure 3-12). Again, since we are estimating three G parameters based on two values extracted from the receiver function stacks, the problem is underdetermined and the bounds on the parameters are mutually dependent. For example, for G at 50 km depth, a velocity drop of no more than 4.8% is estimated to occur over >15 km, whereas for G at 60 km depth, the maximum velocity drop is 5.4% and the transition thickness is 0-8 km.

The absolute amplitude of the G peak in the observations is smaller than the amplitudes in the synthetic cases. This is likely due in part to the presence of microseismic noise in the data, but models have also shown that the thickness and strength of a discontinuity influence receiver function amplitudes (Rychert et al., 2007). The low amplitude of the G peak in the observed receiver functions suggests a preference for a wider and weaker discontinuity. Therefore, while the data can

be explained by a narrower and stronger discontinuity at 60 km depth, we prefer a model where G is present at 50-55 km depth with a thickness of 10-20 km and a Vsv drop of <5%.

The mapping between peak times and discontinuity depths for receiver functions depends on the velocity model prescribed for shallow structure above the discontinuity. We minimize the effects of shallow structure by using independent constraints specific to the NoMelt site to set our crustal velocity model (Lizarralde et al., 2018; Russell et al., 2019) (Figure 3-13), but some uncertainty remains due primarily to sediments. The high Vp/Vs ratio of marine sediments means that small differences in sediment thickness results in large differences in the relative arrival times of direct and converted phases. We explore the sensitivity of the constraints on G parameters to shallow structure by varying sediment thickness and Vp/Vs within ranges observed at nearby IODP drill sites (Gealy, 1971; Pälike et al., 2010a, 2010b; Shipboard Scientific Party, 2002). For the highest Vp/Vs (3.2) and the maximum sediment thickness we tested (200 m), the range of models that could explain the observations expands slightly to include depths up to 67 km with Vsv drops up to 6.3%. However, a deeper discontinuity at 67 km is still required to be thin (0-5 km) relative to the models with shallower discontinuities.

### 3.5 Discussion

Receiver functions from NoMelt are consistent with the presence of a seismic discontinuity at 50-55 km depth corresponding to a decrease of up to 5% in Vsv as a gradient over 10-20 km, which we interpret as the G discontinuity. The primary factors proposed to explain the presence of seismic discontinuities in the upper mantle are compositional gradients, changes in mineral fabric, and accumulations of partial melt. Electrical conductivity measured at the NoMelt site indicates that G is unlikely to be related to melt in this location (Matsuno & Evans, 2017; Sarafian et al., 2015). While the observations from NoMelt cannot conclusively rule out mineral fabrics and anisotropy as an explanation for G, the local seismic and electrical structure suggest that G is best explained by the presence of a dehydration boundary (Figure 3-14). Surface wave measurements from NoMelt show a change in the strength and orientation of azimuthal anisotropy that appears to be deeper than the top of G (Lin et al., 2016), and this apparent separation between G and the observed change in anisotropy suggests that G does not represent a discrete LAB. Rather, G may mark the beginning of a distributed shear zone between the lithosphere and asthenosphere.

While partial melt significantly reduces seismic velocities and has been invoked to explain observations of the G discontinuity both in young oceanic lithosphere (Rychert et al., 2018) and across the oceans (Kawakatsu et al., 2009; Schmerr, 2012), the electrical structure at the NoMelt site is not consistent with the presence of a conductive layer indicative of partial melt accumulation (Sarafian et al., 2015). The magnitude of the velocity reduction associated with partial melt is highly dependent on the melt geometry, and models suggest that even a small melt fraction of 1% could produce up to a 7.9% reduction in Vs for melt in connected tubules and films at grain boundaries (Hammond & Humphreys, 2000; Hirschmann, 2010). However, this kind of connected melt would be highly conductive and should therefore have a signal in the magnetotelluric data. Features interpreted as melt-rich channels at the base of the lithosphere have been observed at some locations in magnetotelluric studies (e.g., Naif et al., 2013). The absence of such a signal at the NoMelt site indicates that G is not a partial melt layer at this location. However, the receiver functions do not preclude the presence of crystallized melt trapped in the lithosphere due to inefficient melt extraction.

The top of the G discontinuity appears to be shallower than the change in the strength and orientation of azimuthal anisotropy observed at 70-100 km beneath the NoMelt array (Lin et al., 2016). The observed change in azimuthal anisotropy coincides with the seismic low velocity zone (LVZ), similar to basin-wide observations that show an age-dependent transition in azimuthal anisotropy following the LVZ across the Pacific (e.g., Beghein et al., 2014; Burgos et al., 2014; Debayle & Ricard, 2013). The rotation of the fast direction away from the paleospreading direction observed at ~80 km depth at the NoMelt site has been interpreted as representing a transition from mineral fabric locked into the lithosphere to fabric dominated by subsequent asthenospheric flow patterns such as pressure gradient-driven return flow and/or secondary convection (Lin et al., 2016). In this interpretation, the presence of G at a shallower depth than the change in anisotropy suggests that although G may be part of the lithosphere-asthenosphere transition, shear continues to be accommodated in the mantle below the discontinuity. Notably, proximal SS precursor observations have suggested that two seismic discontinuities are present in the upper mantle near the NoMelt site, at depths of ~50 and 90 km (Tharimena et al., 2017). These depths agree well with G and with the depth of the change in azimuthal anisotropy in the surface wave model.

Although the G discontinuity appears to be shallower than the observed changes in azimuthal anisotropy, a contribution to G from changes in mineral fabrics cannot be definitively ruled out. Radial anisotropy at the NoMelt site has only been directly measured down to 35 km (Russell et al., 2019), but basin-wide models see strong positive gradients at 50-70 km depth independent of plate age (Auer et al., 2015; Burgos et al., 2014; Nettles & Dziewoński, 2008) which matches the depth of G observed in this study. Mantle flow models indicate that strong gradients in mineral fabrics manifesting as gradients in radial anisotropy can form as a natural consequence of corner flow and plate-driven shear near mid-ocean ridges, irrespective of whether water or melt is present (Navid Hedjazian et al., 2017).

The observed G discontinuity could be explained by the presence of a dehydration boundary. The electrical structure is consistent with the presence of a 60-80 km thick resistive lid, indicative of a dry layer above mantle material with a higher water content (Matsuno & Evans, 2017; Sarafian et al., 2015). This agrees well with models that predict a dehydration boundary at ~60-70 km depth within the oceanic upper mantle due to the extraction of water during melting at mid-ocean ridges (Hirth & Kohlstedt, 1996). Models suggest that the resulting contrast in water content could generate a decrease of up to ~5% in Vs through the mechanism of elastically accommodated grain boundary sliding (Karato, 2012). The observed depth of G agrees well with both the transition in the electrical structure and the model predictions for a dehydration boundary, and a Vsv drop of 5% or less could explain the receiver functions. It is notable that multi-phase seismic velocity models for nearby corridors across the Pacific plate also show evidence for a sharp discontinuity around 60-70 km depth that has been interpreted as a dehydration boundary (Gaherty et al., 1996; Tan & Helmberger, 2007).

The combined measurements of the electrical, seismic, and discontinuity structures at the NoMelt site suggest that the G discontinuity is best explained by a dehydration boundary. The G could thus represent the beginning of the transition from the lithosphere to the asthenosphere as the viscosity change associated with dehydration could localize some shear at G, but the observation of a deeper gradient in azimuthal anisotropy indicates that relative motion between the plate and underlying mantle is accommodated over a larger depth interval. While crystallized melt and/or changes in mineral fabrics and anisotropy cannot be ruled out as explanations for the observed discontinuity,

we prefer the dehydration boundary model because it is able to explain aspects of the upper mantle structure from independent analyses of both seismic and electromagnetic data.

### 3.6 Conclusions

We have imaged the G discontinuity at the NoMelt site in the central Pacific, and combined constraints from the receiver functions, smooth seismic structure, and electrical structure at this site indicate that the observed G discontinuity does not correspond to partial melt but can be explained by the presence of a dehydration boundary. Our preferred model for G from the receiver functions has a Vsv drop of <5% as a gradient over 10-20 km starting at 50-55 km depth. In this interpretation, G does not represent a discrete lithosphere-asthenosphere boundary, but could be associated with the beginning of a transition zone between the rigid plate and the deforming mantle.

This study demonstrates the utility of combining different types of geophysical measurements to investigate local upper mantle structure. The context provided by local constraints on the seismic and electrical structure of the mantle enables us to better interpret the receiver function results, and the receiver functions in turn add a constraint that can be used to refine the seismic models for the NoMelt site in the future.

### 3.7 Acknowledgments

We thank the Captain and crew of the R/V *Marcus G. Langseth* and the engineers and technicians from the Scripps Institution of Oceanography and the Woods Hole Oceanographic Institution, who provided instruments through the National Science Foundation's Ocean Bottom Seismograph Instrument Pool (OBSIP). The professionalism and expertise of these individuals were key to the success of the NoMelt experiment. We also thank Emily Hopper for her helpful advice on receiver functions. The OBS data described here are archived at the IRIS Data Management Center (http://www.iris.edu) under network code ZA 2011-2013. The map in Figure 3-2 was made using the Generic Mapping Tool, GMT (Wessel et al., 2013). This work was supported by NSF grant OCE-0928663 to D. Lizarralde, J. Collins, and R. Evans, NSF grant OCE-0927172 to G. Hirth, NSF grant OCE-0928270 to J. Gaherty, and an NSF Graduate Research Fellowship to H. Mark.

### 3.8 Figures

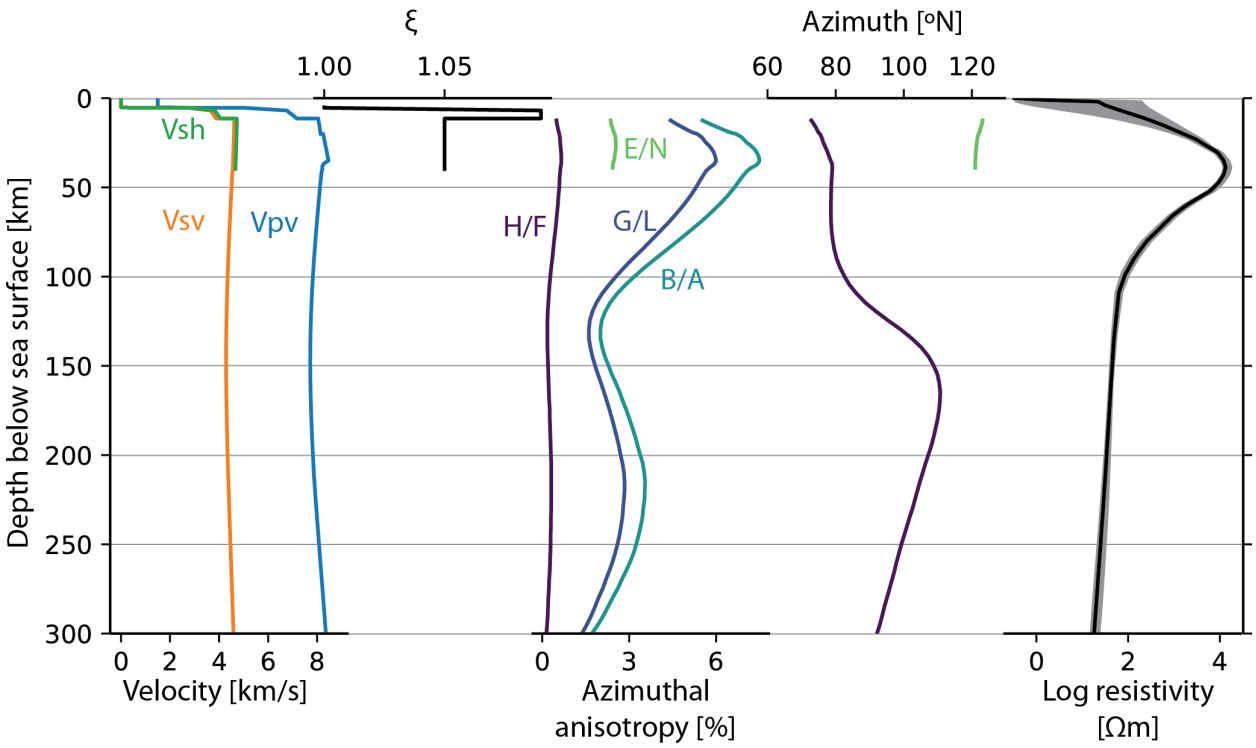


**Figure 3-1.** Local constraints on seismic and electrical structure from NoMelt, including seismic velocities, radial anisotropy, and the strength and orientation of azimuthal anisotropy from Lin et al. (2016) and Russell et al. (2019); and electrical resistivity from Sarafian et al. (2015). See Russell et al. for a description of the different azimuthal anisotropy terms.

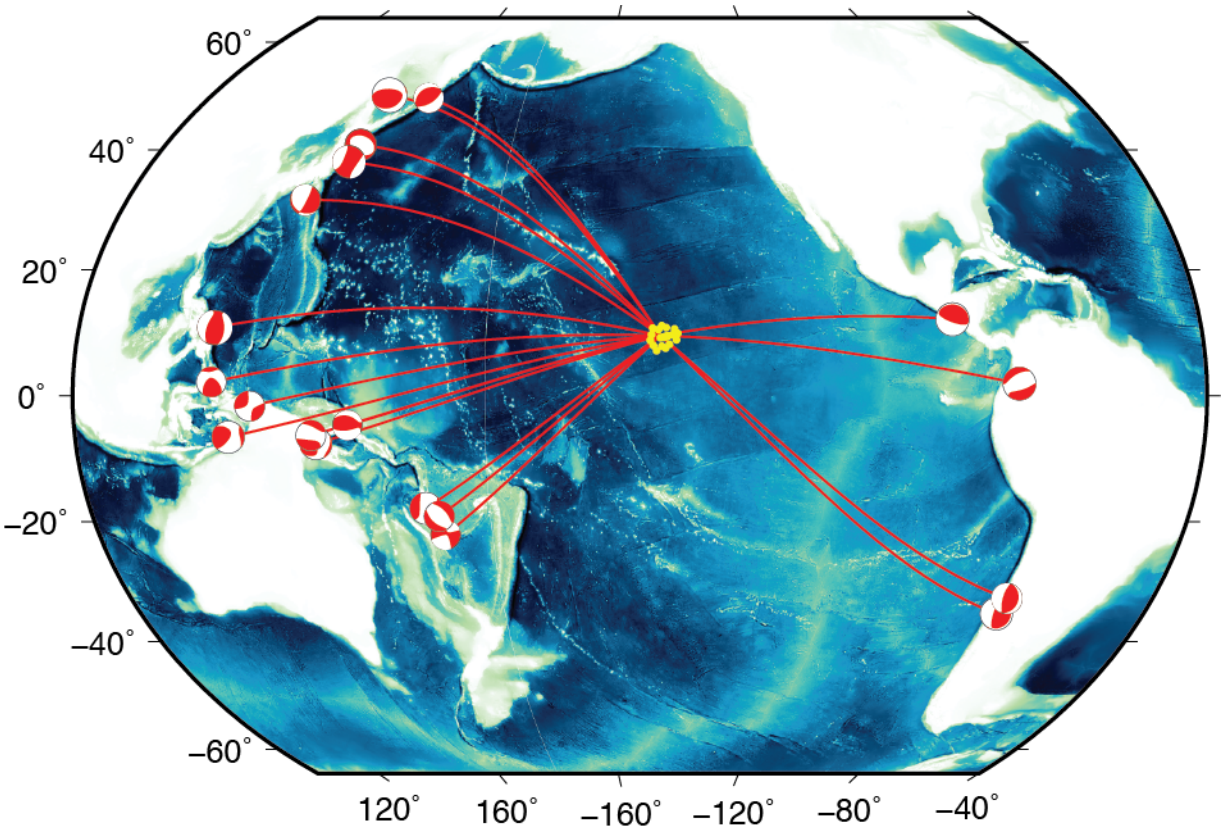


**Figure 3-2.** Map of the Pacific showing the location of the NoMelt broadband OBS array (yellow dots), and the locations and focal mechanisms of the 19 events used in this study (beachballs).

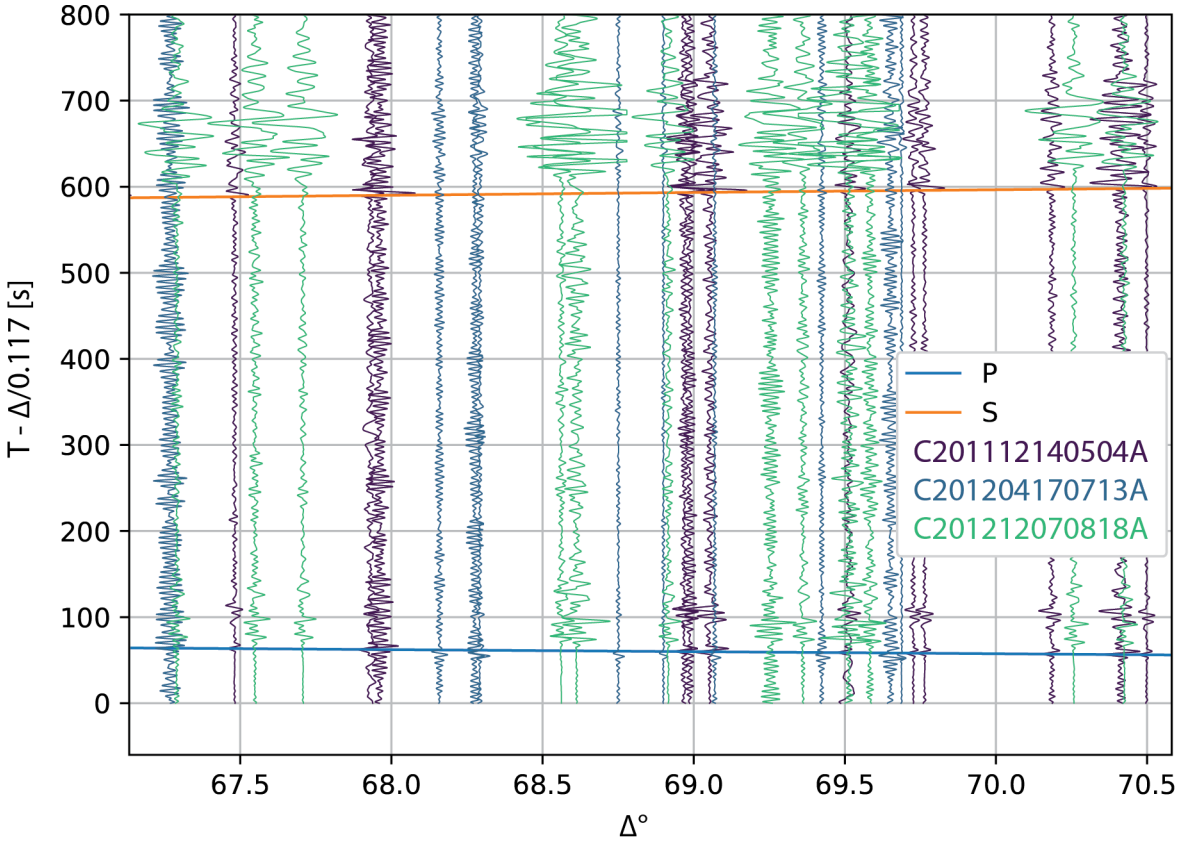


**Figure 3-3.** A record section showing radial component data from three events at similar distances from the NoMelt array, with direct phase arrival times predicted for the global velocity model *ak135* shown by the blue (*P*) and orange (*S*) horizontal lines. Traces are color-coded by event. Event C201204170713A (blue), which occurred near Eastern New Guinea, shows little or no energy near the predicted arrival times, so data from that event was excluded from the receiver function analysis. In contrast, the other two events shown (C20112140504A, near Eastern New Guinea, purple; and C20121207818A, offshore Japan, green) have clear direct phase arrivals.

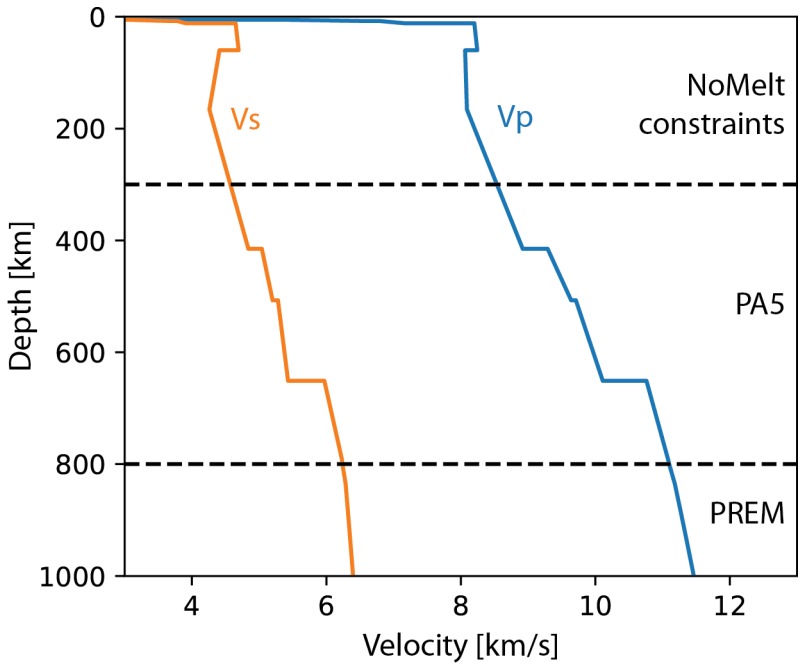


**Figure 3-4.** The seismic velocity model used to calculate the synthetics in Figure 3-6 (except for 3-6c). 0 km corresponds to the sea surface. The upper 300 km of the model are modified from the model of Lin et al. (2016) and Russell et al. (2019), with the addition of a step-function discontinuity at 60 km where Vsv drops by 6.4%. Between 300 and 800 km, the model follows PA5 (Gaherty et al., 1996). From 800 km down to the outer core boundary, the model follows PREM (Dziewonski & Anderson, 1981). The model is truncated at the outer core boundary.

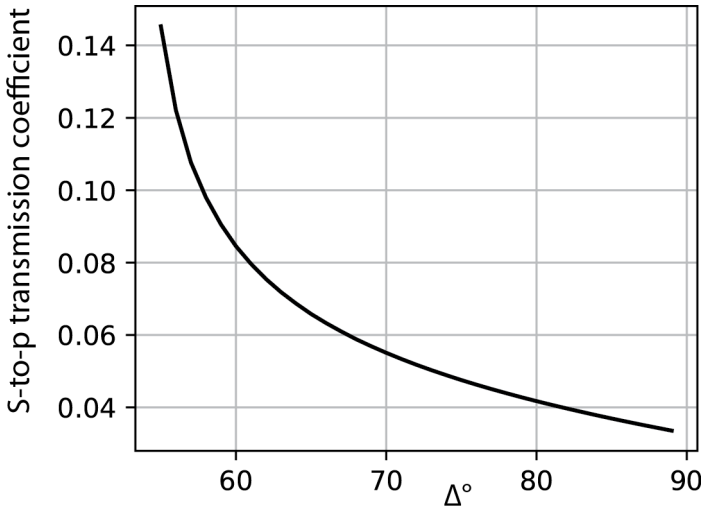


**Figure 3-5.** *S*-to-*p* transmission coefficients as a function of epicentral distance for the velocity model shown in Figure 3-4. The strength of the converted phase decreases sharply with increasing epicentral distance. For events closer than ~55°, ray theory does not predict a converted phase from a discontinuity at 60 km depth.

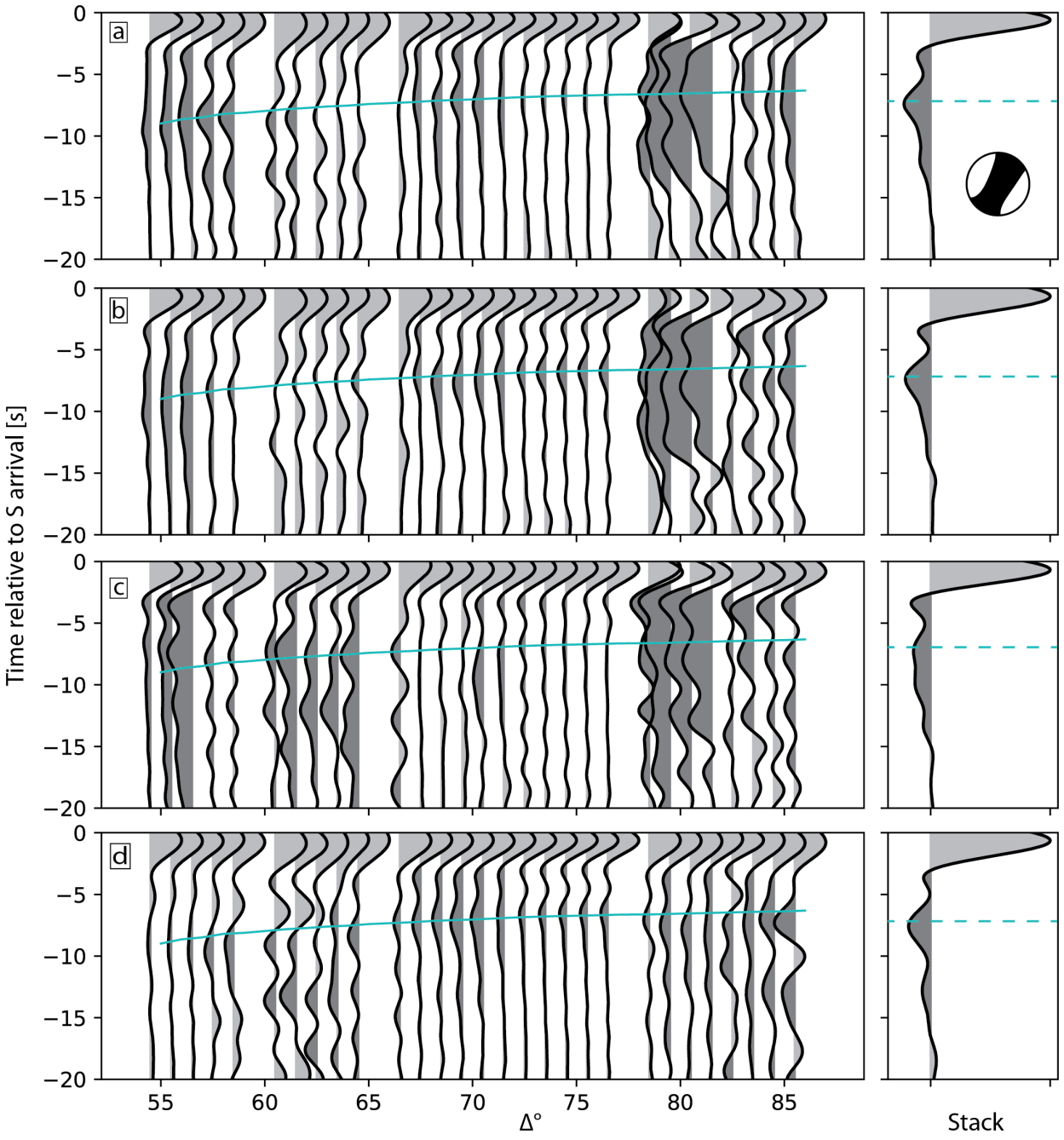
a
b
c
d
0
−5
−10
−15
−20
Time relative to S arrival [s]
55
60
65
70
75
80
85
Δ°
Stack

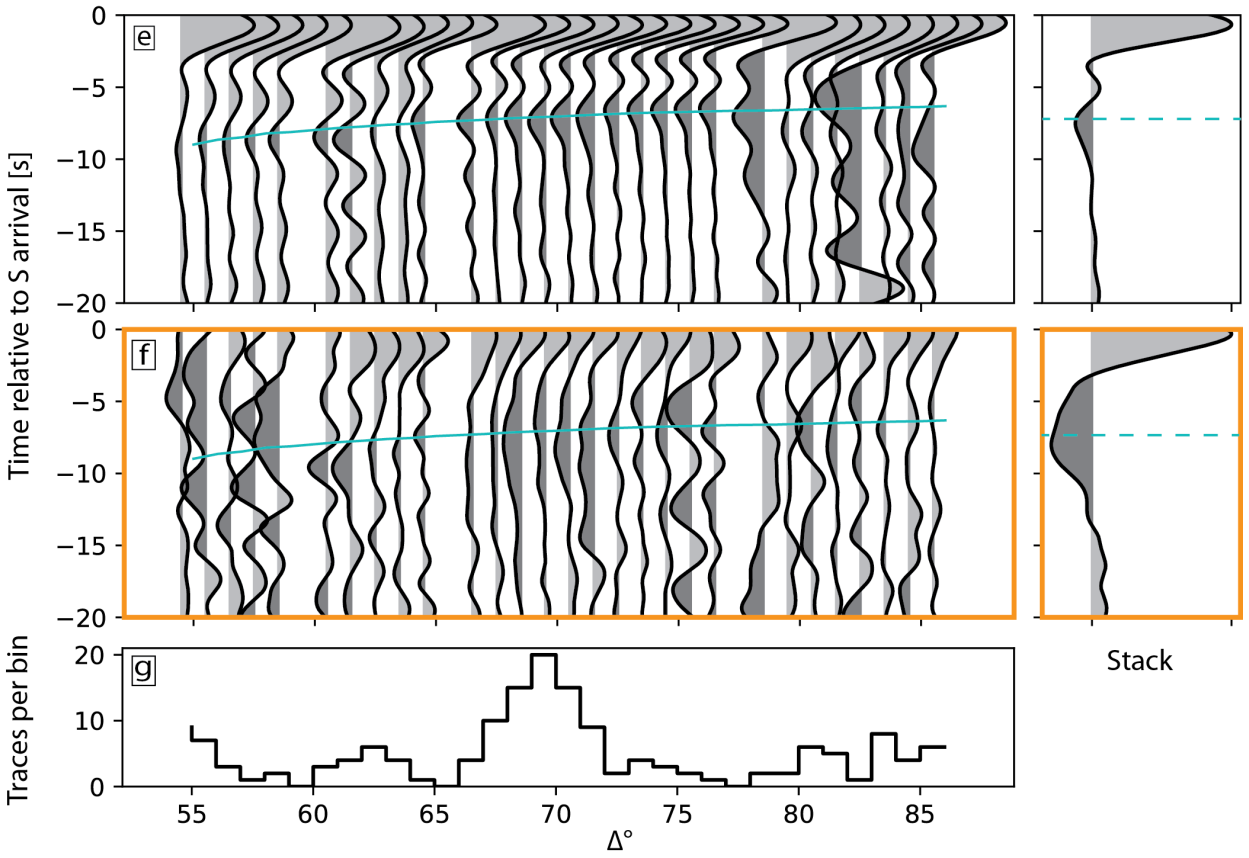


**Figure 3-6.** Receiver functions ordered by epicentral distance (left column), along with moveout-corrected stacks (right column). Predicted times for the G conversion are shown by light blue lines in the left column and dashed light blue lines in the right column. **(a)** Synthetic receiver functions for a velocity model with G present at 60 km depth (Figure 3-4), calculated for a frequency band of ~1.4-35 seconds (0.029-0.7 Hz). A single back azimuth and moment tensor are used for all traces. The focal mechanism corresponding to the moment tensor is shown next to the stack. Epicentral distances correspond to the data set. **(b)** Synthetics for the same velocity model as in (a), calculated for a frequency band of 4-35 seconds (0.029-0.25 Hz). Back azimuths, moment tensors, and epicentral distances are as in (a). **(c)** Synthetics for a velocity model with G absent. Back azimuths, moment tensors, and epicentral distances are as in (a). The moveout correction for the stack is calculated using the velocity model with G present at 60 km (Figure 3-4). **(d)** Synthetics for the same velocity model as in (a). One moment tensor is used for all traces; back azimuths and epicentral distances correspond to the data set. **(e)** Synthetics for a velocity model with G present at 60 km.

Moment tensors, back azimuths, and epicentral distances all mimic the data set. **(f)** The observed receiver functions. The moveout correction for the stack is done using a velocity model with G present at 60 km depth (Figure 3-4). **(g)** Histogram showing the number of traces in each bin for all sets of receiver functions.

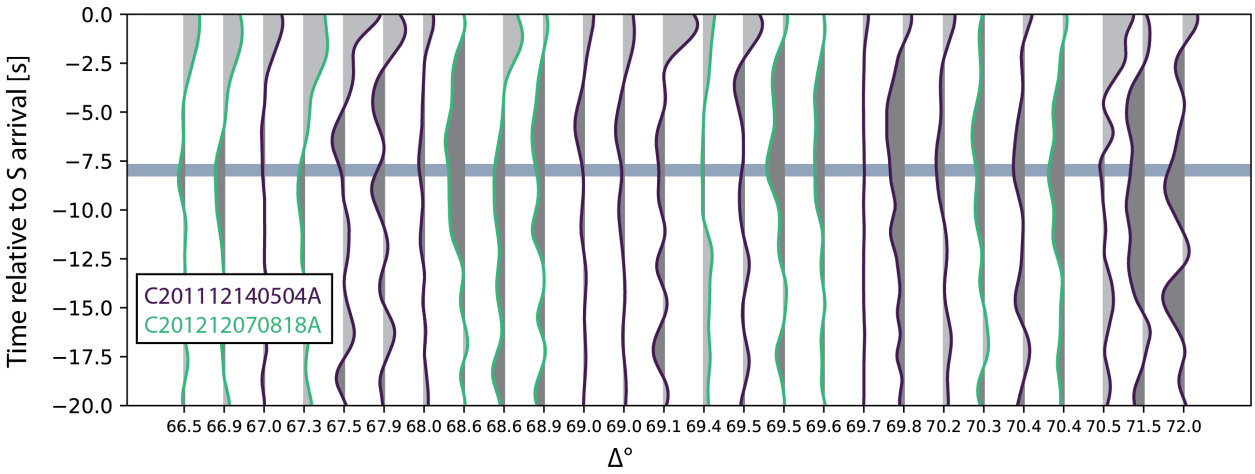


**Figure 3-7.** Individual receiver functions from two events. Traces from C201112140504A, which occurred near Eastern New Guinea, are plotted as purple lines; and traces from C201212070818A, which occurred near offshore Japan, are plotted as green lines. The blue bar indicates the range of arrival times of G observed in stacks of all the observations. All traces are plotted in order of increasing epicentral distance but with even spacing for clear visibility. While some traces have energy around the G arrival time from the stack (~8 seconds), others do not, and the individual traces are noisy overall.

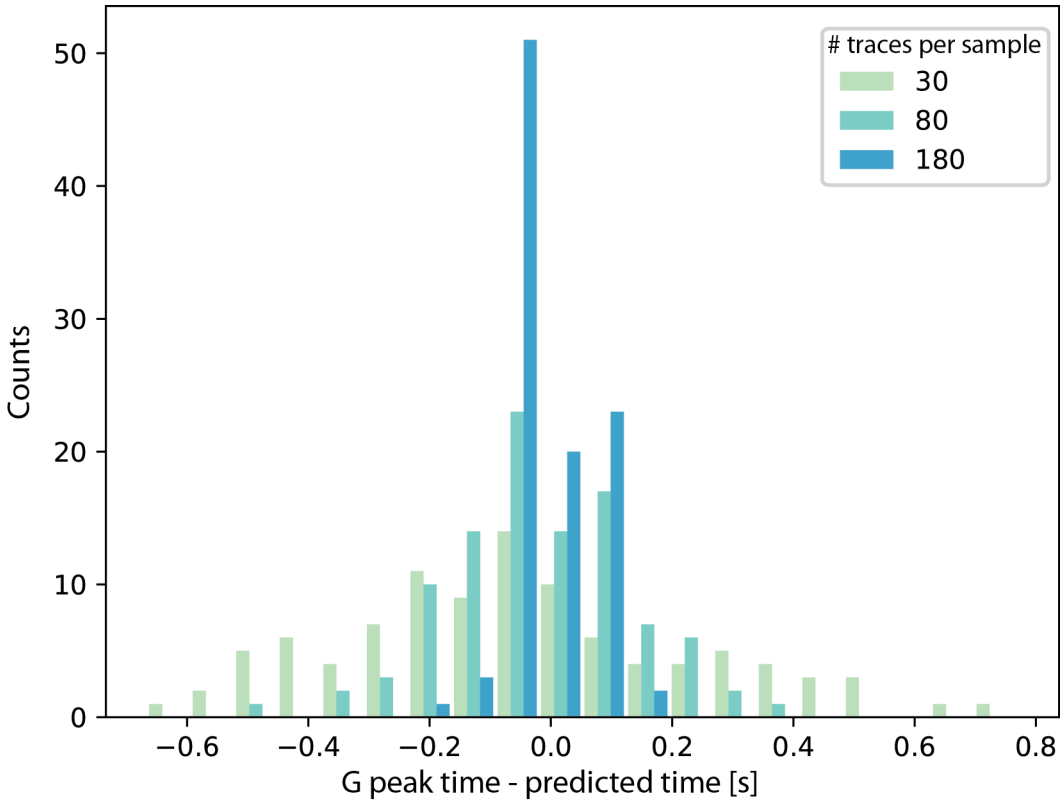


**Figure 3-8.** Histograms of the difference between the measured and predicted G peak times for stacks of 30-, 80-, and 180-trace subsamples of synthetic receiver functions. The synthetics were calculated using a model with G at 70 km and a step function drop of 6.4% in Vsv. 100 bootstrap samples were taken for each sample size. The distribution narrows significantly as the bootstrap sample size increases.

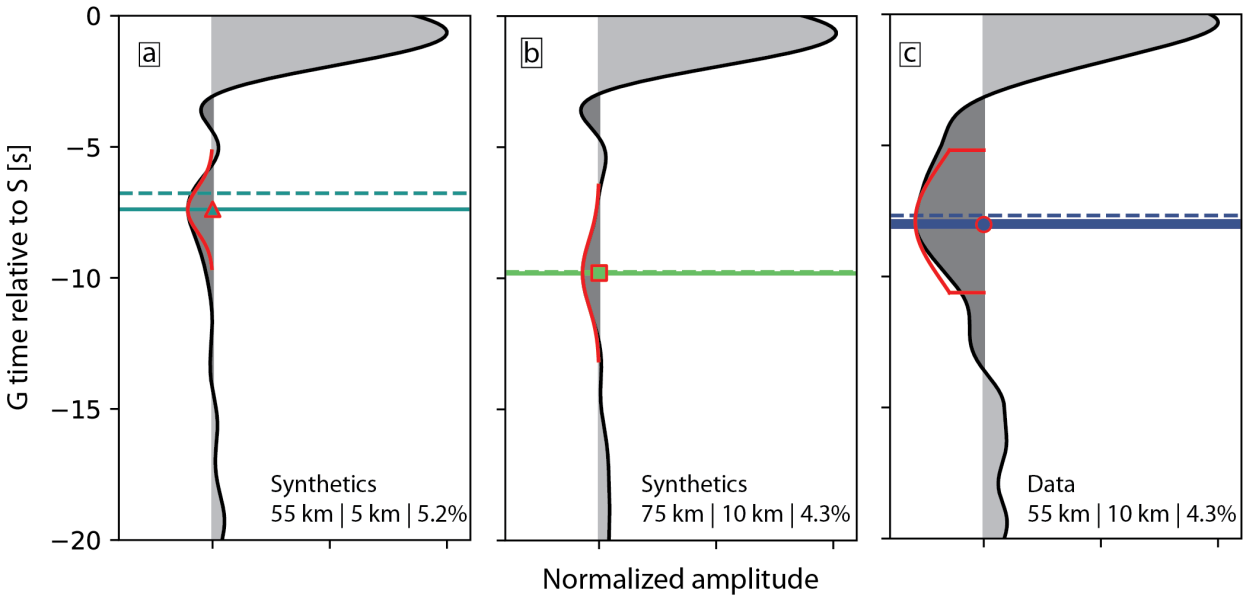


**Figure 3-9.** Receiver function stacks for two matched synthetic cases, and for the data with a representative moveout correction applied. The stacks are shown by the black lines and gray shading, and the Gaussian fits to the G peaks are shown by red lines. The maximum amplitude of the G peak is marked on each plot by a symbol outlined in red, and horizontal shaded bands span the range of G peak times obtained by stacking the receiver functions with jackknife resampling. Dashed lines show the predicted time for the G peak based on the moveout correction model used for the stack. **(a)** Matched synthetic receiver function stack with G as a 5.2% drop in Vsv over 5 km, starting at 55 km. **(b)** Matched synthetic receiver function stack with G as a 4.3% drop in Vsv over 10 km, starting at 75 km. **(c)** Receiver function stack from NoMelt data, with moveout corrections calculated in a model where G is a 4.3% drop in Vsv over 10 km, starting at 55 km.

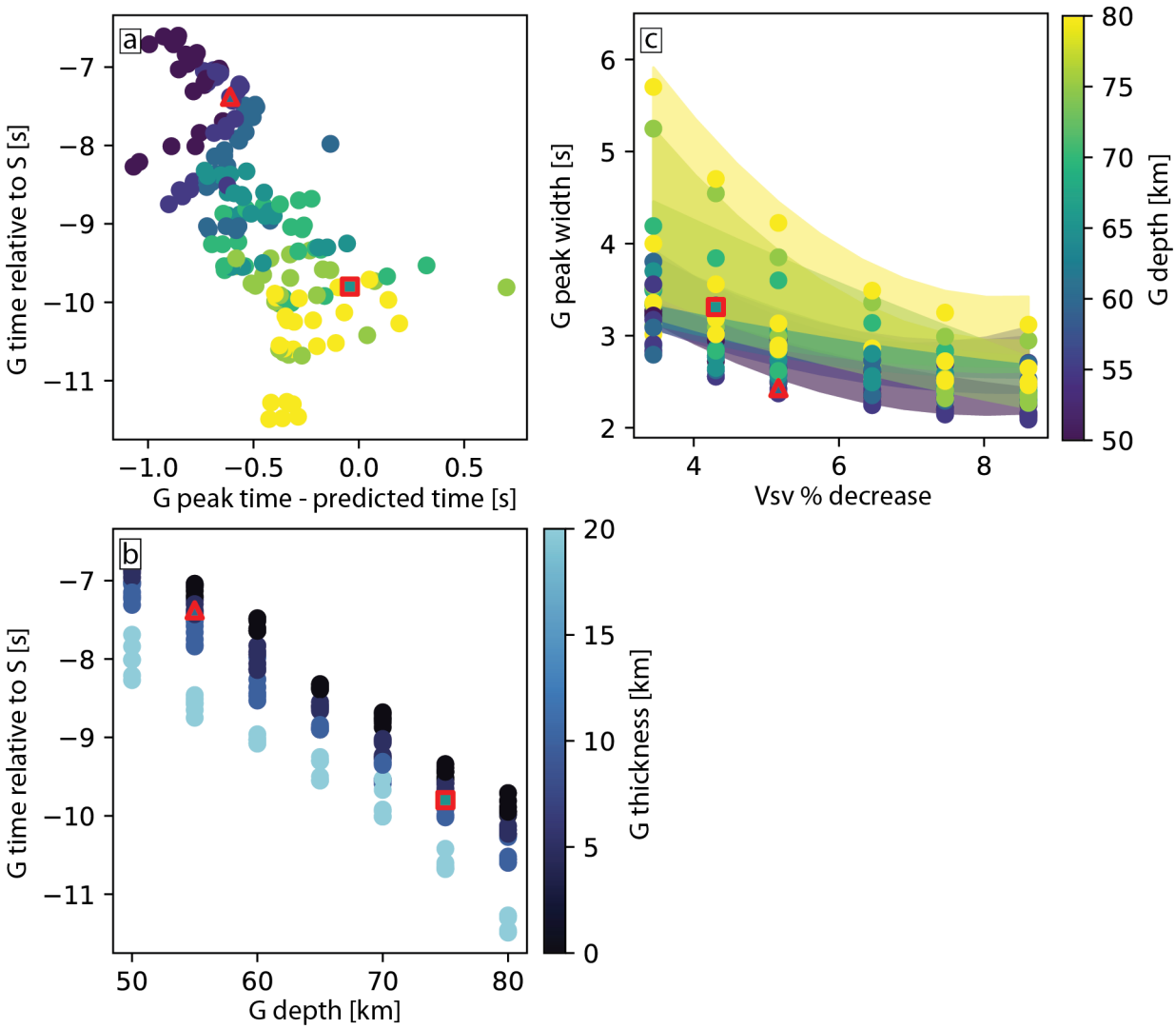


**Figure 3-10.** Results from receiver function stacks for matched synthetic cases, where the velocity model used for moveout corrections matches the model used to generate the synthetics. Points outlined in red correspond to cases shown in Figures 3-9 and 3-11. **(a)** Time of the G peak relative to a ray-theoretical prediction versus the time of the G peak relative to the direct *S* arrival in receiver function stacks. All peak times are within 1 second of the predicted time. **(b)** Depth of the top of G versus the time of the G peak relative to the direct *S* arrival. The time of the G peak varies with both the depth and the thickness of G. **(c)** Percent decrease in Vsv at G versus the width of the G peak in seconds. The peak width varies with the depth and the strength of G. The range of peak widths spanned for each G depth are shown by the shaded regions.

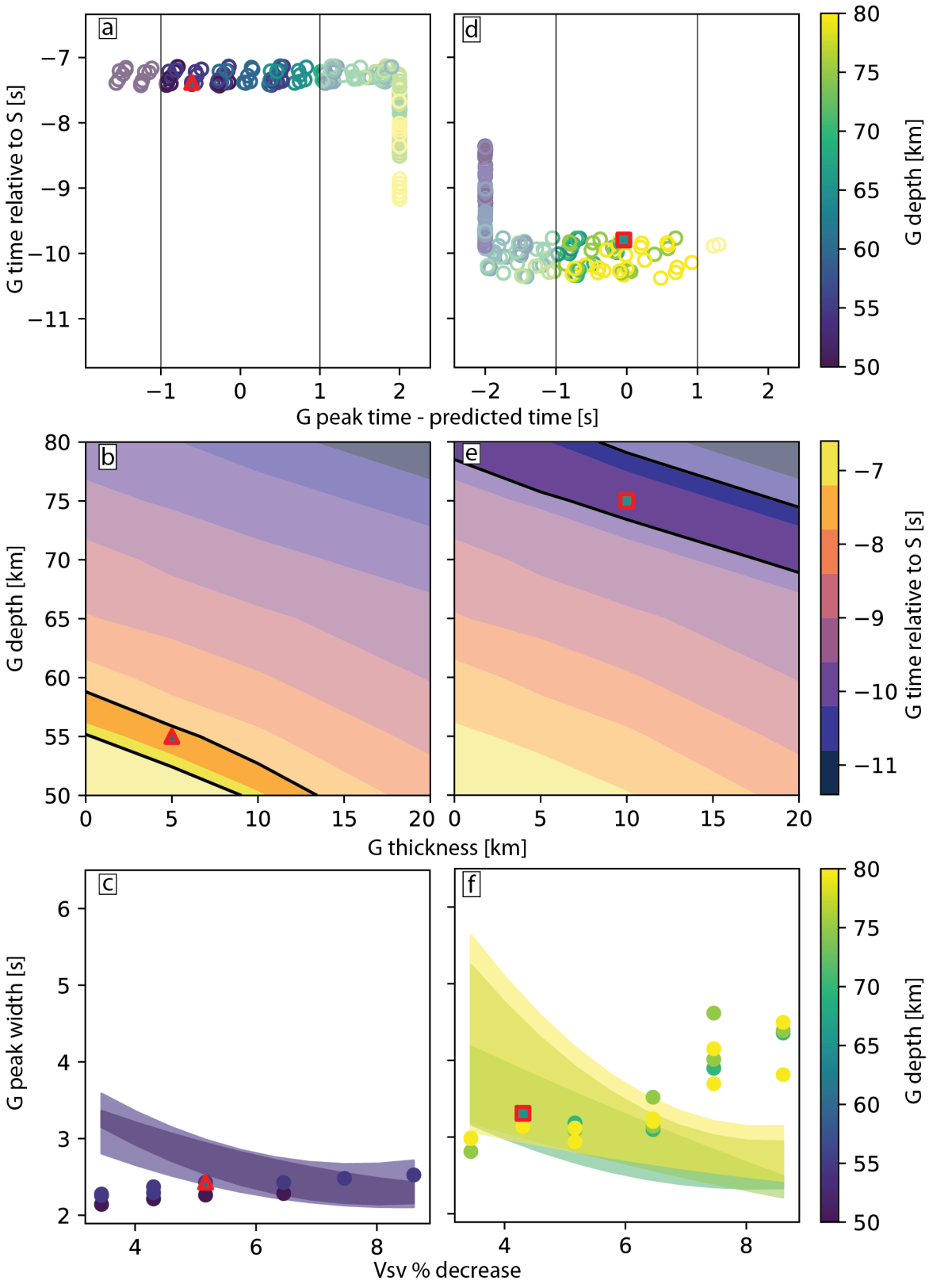
a
d
b
e
c
f
G time relative to S [s]
G peak time - predicted time [s]
G depth [km]
G thickness [km]
G time relative to S [s]
G peak width [s]
Vsv % decrease
G depth [km]

**Figure 3-11.** Constraining G parameters for synthetics generated in two velocity models: **(a, b, c)** G at 55 km depth, 5 km thickness, 5.2% Vsv drop, and **(d, e, f)** G at 75 km depth, 10 km thickness, 4.3% Vsv drop. Symbols outlined in red mark the matched cases, where the moveout velocity model matches the known generating model. **(a, d)** Open circles show the time of G relative to ray-theoretical predictions versus the time of the G peak relative to the direct *S* arrival for stacks of synthetics calculated with mismatched moveout corrections. The apparently anomalous G peak times correspond to models where the predicted time was so far from the G peak in the stack that the algorithm used to select the peak time failed to properly locate the peak. **(b, e)** Depth of G versus thickness of G, with color contours showing the time of the G peak relative to direct *S* predicted for matched synthetics from Figure 3-10b. The black lines bound the region where the time of G in the stacks from (a, d) matches the predictions from the matched synthetic cases. **(c, f)** G peak width in seconds versus the strength of G. Points show the values for models falling within the allowed region outlined in (b, e), and shaded regions show the predictions for matched synthetics from Figure 3-10c.

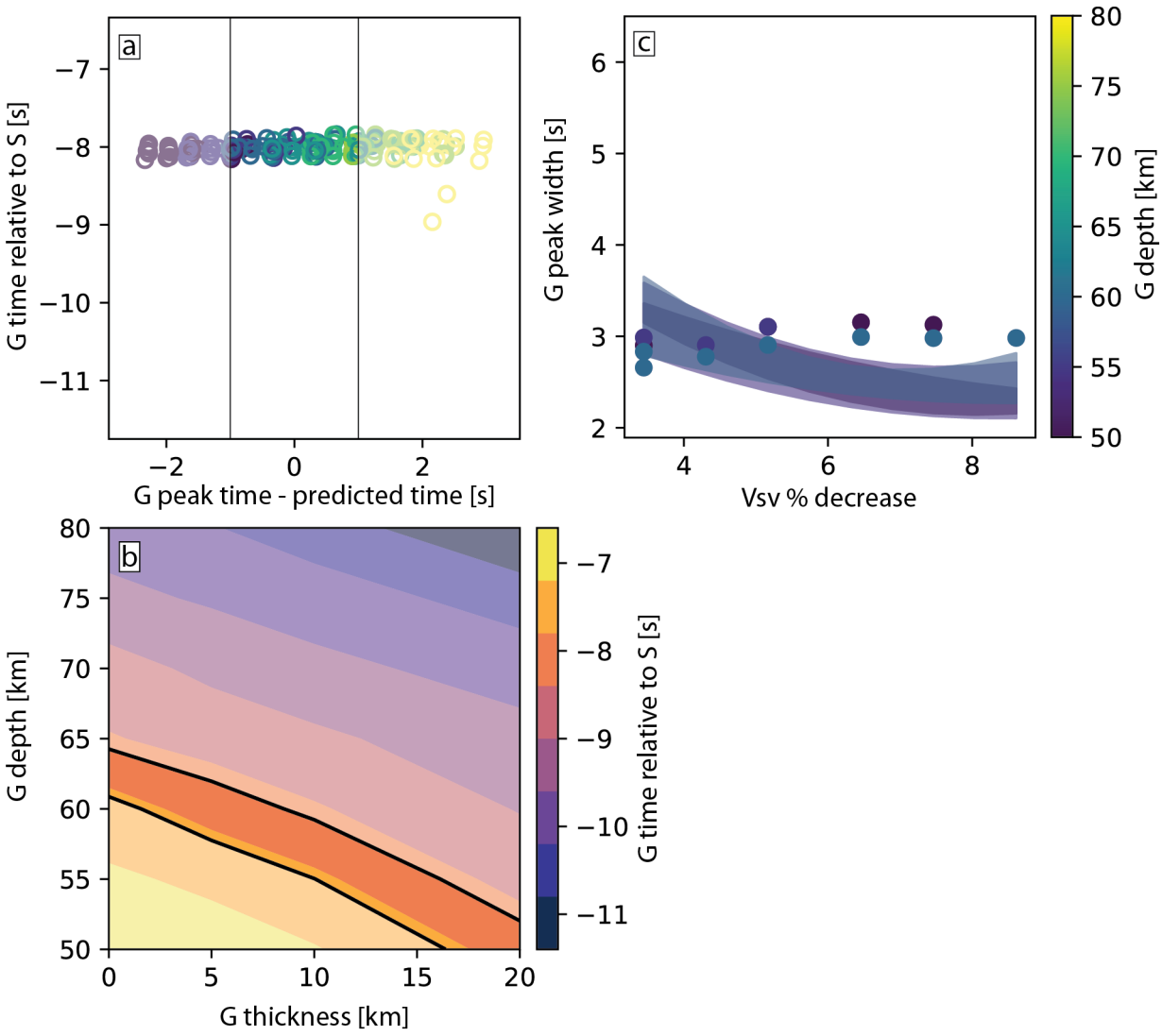


**Figure 3-12.** Constraining G parameters for the data. **(a)** Time of the G peak relative to ray-theoretical predictions versus the time of the G peak relative to the direct S. The G peak in the stack is 7.7-8.24 seconds before the direct *S* arrival. **(b)** Thickness of G versus depth of G, with color contours showing the time of the G peak predicted for matched synthetics from Figure 3-10b. The black lines bound the region where the time of G in the stacks from (a) matches the time from the matched synthetics. **(c)** Strength of G versus the width of the G peak. Points show the values for models falling within the allowed region outlined in (b), and shaded regions show the ranges for matched synthetics from Figure 3-10c.

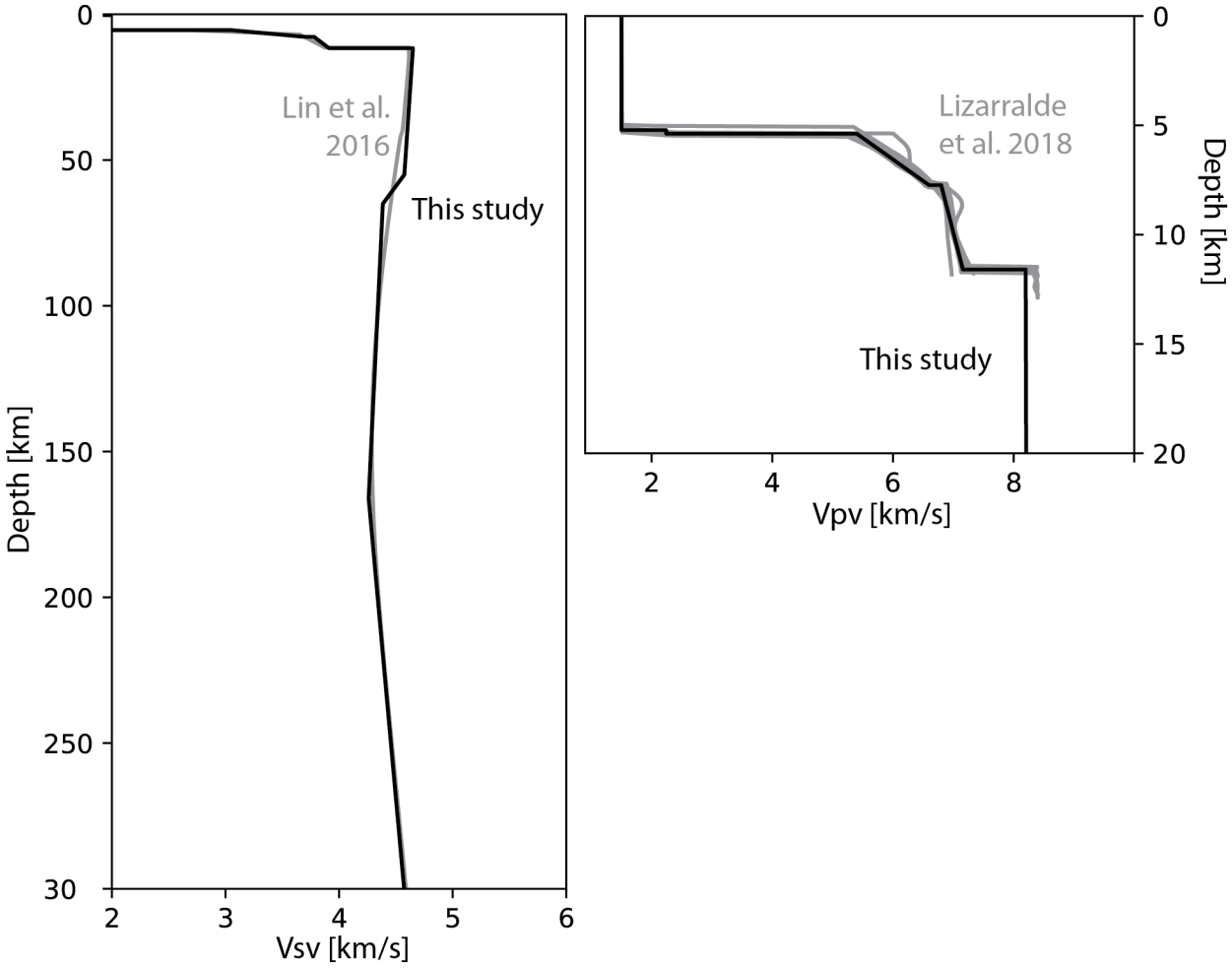


**Figure 3-13.** The preferred velocity structure based on the receiver functions in black compared to the Vs model from surface waves (grey, left) and the crustal Vp model below several individual OBS from active-source data (gray, right) (Lin et al., 2016; Lizarralde et al., 2018). 0 km depth corresponds to the sea surface.

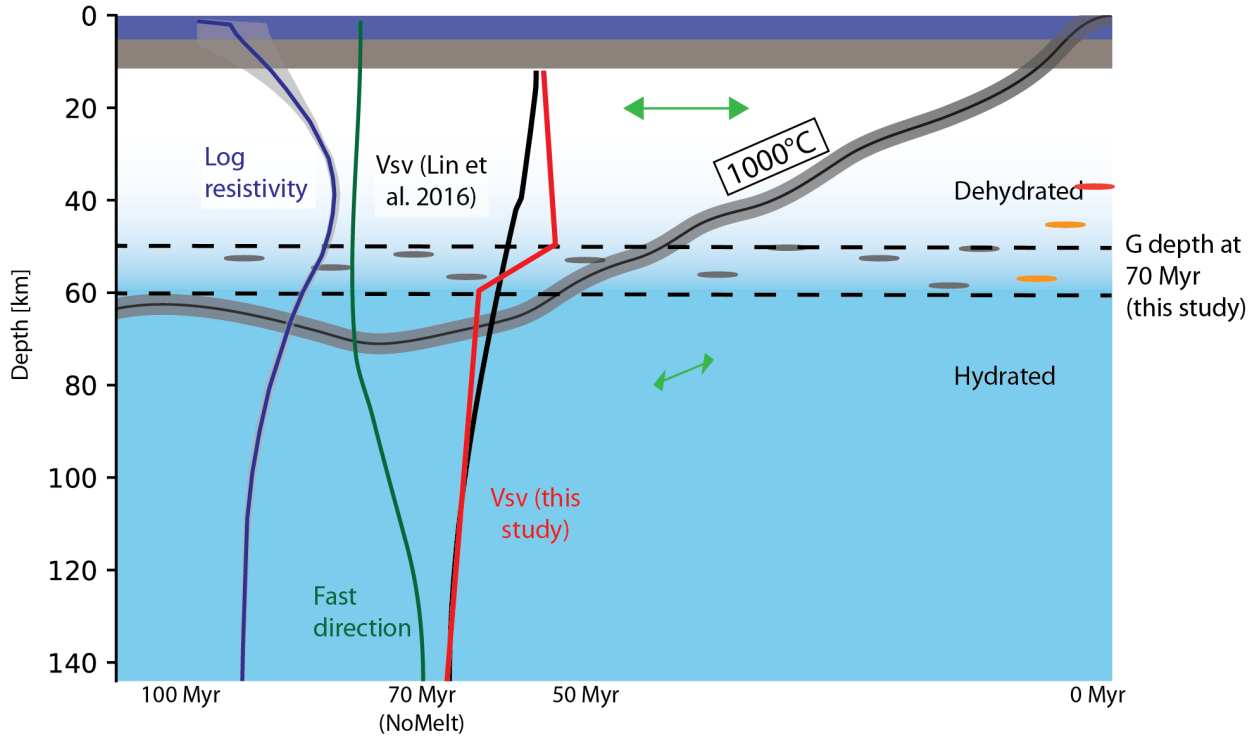


**Figure 3-14.** Schematic illustration of a potential structure for the oceanic upper mantle. Hydration in the mantle is shown by blue background shading, green arrows represent the change in the orientation of azimuthal anisotropy with depth, and gray and red ellipses represent trapped pockets of melt that might be present within the mantle. Models for Vsv, the fast direction of azimuthal anisotropy, and log resistivity from NoMelt are from this study, Lin et al. (2016), and Sarafian et al. (2015). A basin-averaged 1000°C isotherm for the Pacific from Ritzwoller et al. (2004) is plotted in black.

# Chapter 4

# Controls on mid-ocean ridge normal fault seismicity across spreading rates from rate-and-state friction models

This chapter was originally published as: Mark, H. F., Behn, M. D., Olive, J.-A., & Liu, Y. (2018). Controls on mid-ocean ridge normal fault seismicity across spreading rates from rate-and-state friction models. Journal of Geophysical Research: Solid Earth, 123, 6719-6733. 

## 4.1 Abstract

Recent seismic and geodetic observations have led to a growing realization that a significant amount of fault slip at plate boundaries occurs aseismically and that the amount of aseismic slip varies across tectonic settings. Seismic moment release rates measured along the fast-spreading East Pacific Rise suggest that the majority of fault slip occurs aseismically. By contrast, at the slow-spreading Mid-Atlantic Ridge seismic slip may represent up to 60% of total fault displacement. In this study, we use rate-and-state friction models to quantify the seismic coupling coefficient, defined as the fraction of total fault slip that occurs seismically, on mid-ocean ridge normal faults and investigate controls on fault behavior that might produce variations in coupling observed at oceanic spreading centers. We find that the seismic coupling coefficient scales with the ratio of the downdip width of the seismogenic area $(W)$ to the critical earthquake nucleation size $(h^*)$. At mid-ocean ridges, $W$ is expected to increase with decreasing spreading rate. Thus, the relationship between seismic coupling and $W/h^*$ predicted from our models explains the first order variations in seismic coupling coefficient as a function of spreading rate.

## 4.2 Introduction

Seismic and geodetic measurements over the last decade have revealed that plate boundary strain can be accommodated by a spectrum of fault slip behavior (e.g., Miller et al., 2002; Peng & Gomberg, 2010; Wech et al., 2009). While earthquakes are the most dramatic end member of that spectrum, it has become increasingly clear that aseismic slip over a variety of timescales contributes significantly to total fault displacement in some tectonic settings (e.g., Bird et al., 2002; Dragert et al., 2001; Frohlich & Wetzel, 2007; Schwartz & Rokosky, 2007; Sobolev & Rundquist, 1999; Vidale & Houston, 2012). Understanding the partitioning of seismic versus aseismic displacement on faults is important from a hazards perspective, as unquantified aseismic slip adds uncertainty to risk assessments for faults with the potential to generate large earthquakes (e.g., Dixon et al., 2014; Linde et al., 1996; Linde & Silver, 1989). Further, some studies suggest that aseismic slip events can trigger large earthquakes (e.g., Kato et al., 2012; Radiguet et al., 2016; Segall et al., 2006).

Compiled observations from a range of plate boundaries have been used to show that the proportion of seismic versus aseismic fault slip varies across settings (e.g., Bird & Kagan, 2004; Frohlich & Wetzel, 2007; Sobolev & Rundquist, 1999). Variable slip modes have been observed and modeled for crustal faults, in particular for convergent (e.g., Houston et al., 2011; Liu & Rice, 2005, 2007; Miller et al., 2002; Wech et al., 2009) and transform plate boundaries (e.g., Brune et al., 1969; Froment et al., 2014; Johnson et al., 2006; Linde et al., 1996; Liu et al., 2012; McGuire, 2008; McGuire et al., 2005, 2012; Roland et al., 2012).

Several studies have also addressed seismic behavior and the potential for aseismic slip on faults at divergent plate boundaries (e.g., Biemiller & Lavier, 2017; Calais et al., 2008; Cowie et al., 1993; Olive & Escartín, 2016; Sobolev & Rundquist, 1999). Observations support a range of behavior from seismic and aseismic fault slip across different ridges and ridge segments (Cowie et al., 1993; Olive & Escartín, 2016). However, interpretation of these variations has been limited due to the lack of quantitative models for seismic cycles on mid-ocean ridge normal faults.

The partitioning of fault slip can be described in a time-average sense by the seismic coupling coefficient, $\chi$, which we define as the fraction of fault slip that occurs seismically. The seismic coupling coefficient can be estimated directly by measuring fault displacement and comparing the

moment release predicted for this displacement to the observed seismic moment release (e.g., Cowie et al., 1993). However, this method is labor-intensive, requires high-resolution topographic maps of large areas, and may be skewed by mass-wasting processes and erosion of seafloor fault relief (e.g., Cannat et al., 2013; Goff & Tucholke, 1997). Thus, in practice, coupling is often estimated by comparing seismic moment release rates with estimates of the long-term accumulation of slip on a fault from geodetic data or tectonic reconstructions.

Seismic coupling is observed to vary across convergent (e.g., Frohlich & Wetzel, 2007; Pacheco et al., 1993; Scholz & Campos, 2012; Tichelaar & Ruff, 1993) and transform boundaries (e.g., Boettcher & Jordan, 2004; Frohlich & Wetzel, 2007; Rundquist & Sobolev, 2002) and can vary between different subduction zones, from $\chi = 0.1$ (mostly aseismic) to 1.0 (fully coupled) (e.g., Scholz & Campos, 2012). Coupling also varies between 0 and 1 along strike in individual subduction zones, over length scales of 200–600 km (Métois et al., 2012; Pacheco et al., 1993; Scholz & Campos, 2012). For transform boundaries, Frohlich and Wetzel (2007) found a systematic decrease in the seismic coupling coefficient with relative plate velocity, from ≥4 to ~0. By contrast, Boettcher and Jordan (2004) showed that for a global dataset of 65 mid-ocean ridge transform faults with slip rates from 15 to 150 mm/yr, the coupling coefficient was roughly constant at 0.15.

Several hypotheses have been proposed to explain variations in seismic coupling. One class of models argues that thermal structure and fault geometry exert the primary control on seismic coupling (Boettcher et al., 2007; Liu et al., 2012; Solomon et al., 1988). Together these two factors control the size of the seismogenic zone, defined as the area where earthquakes are able to nucleate (e.g., Scholz, 1998). Other studies, citing experimental evidence that the frictional properties of hydrous minerals such as serpentine differ significantly from those of their anhydrous counterparts (Escartín et al., 1997; Hirth & Guillot, 2013; Reinen et al., 1991, 1994), have proposed that fault zone material properties and/or heterogeneities associated with hydrous alteration or pore pressure exert a primary control on seismic coupling by enabling the nucleation of aseismic slip transients (Liu & Rice, 2005, 2007; McGuire et al., 2012; Roland et al., 2012). It has also been suggested that the magnitude of the normal force acting on the subduction interface controls seismic coupling on megathrusts (Scholz & Campos, 1995, 2012).

A compilation of the available datasets from mid-ocean ridges shows that the seismic coupling coefficient on oceanic normal faults varies inversely with spreading rate (Figure 4-1). Cowie et al. (1993) found the coupling coefficient for faults bounding the fast-spreading East Pacific Rise to be less than 0.01. By contrast, estimates derived using teleseismic and hydroacoustic data from the slow-spreading Mid-Atlantic Ridge indicate coupling coefficients of 0.1–0.3 for symmetric ridge segments and 0.4–0.6 for segments characterized by the presence of large-offset detachment faults (Olive & Escartín, 2016). Frohlich and Wetzel (2007) found a similar systematic variation in the coupling coefficient across a range of spreading rates using teleseismic moment release rates. Moreover, the variation in coupling with spreading rate appears to be robust even with the uncertainty introduced by assumptions regarding fault geometry and magmatism (Olive & Escartín, 2016). Several of these studies suggested that variations in fault thermal structure and the size of the seismogenic zone are responsible for the range of seismic coupling coefficients observed across different ridge spreading rates (Cowie et al., 1993; Solomon et al., 1988). However, they did not address the specific reason why faults near fast–spreading mid–ocean ridges may be more prone to slipping aseismically when they are also known to occasionally generate moderately large earthquakes (e.g., Mw~5–6 along the EPR, Ekström et al., 2012). To date, tests of such hypotheses (e.g., Olive & Escartín, 2016) have relied on extrapolation of rate-and-state models for strike-slip faults (e.g., Liu et al., 2012) to normal fault systems, thus precluding a quantitative assessment of the effects of normal fault geometry on seismic coupling.

In this study, we examine the effects of steady-state thermal structure, spreading rate, and fault geometry on the seismic coupling coefficient for mid-ocean ridge normal faults by using rate-and-state friction models to simulate fault slip on seismic cycle time scales. These new models provide a framework for interpreting observations from mid-ocean ridges. We show that seismic coupling varies systematically with the ratio of the seismogenic layer thickness to the characteristic nucleation size. Based on a comparison of our numerical results to natural systems, we argue that lithologic variations are not required to explain the variability in seismic coupling with spreading rate at mid-ocean ridges and that seismogenic layer thickness, together with the fraction of extension accommodated by magma intrusion, is the primary control on seismic behavior of oceanic normal faults.

### 4.3 Modeling seismic cycles on normal faults

Laboratory experiments have shown that the frictional resistance on an interface depends on the slip velocity during sliding, the *rate;* and on the history of slip on the surface, the *state* (e.g., Dieterich, 1972, 1978, 1979; Marone, 1998; Rice, 1993; Rice & Ruina, 1983; Ruina, 1983). The rate effect is seen during abrupt velocity changes, where friction increases or decreases proportionally to the velocity steps. When sliding velocity is not changing or the fault remains stationary, the dynamic friction varies according to the amount of time static contact is maintained under a load (Beeler et al., 1994; Dieterich, 1978). This rate-and-state frictional behavior can be quantified as a law relating shear and normal stress through a friction coefficient that depends on slip velocity and an empirical state variable $\theta$. The formulation is closed through a second law that describes the time evolution of $\theta$ (Dieterich, 1972, 1978, 1979; Marone, 1998; Rice, 1993).

In this study, we use a single state variable friction law:

$$\tau = \bar{\sigma}\left[f_0 + a\ln\left(\frac{V}{V_0}\right) + b\ln\left(\frac{V_o\theta}{D_c}\right)\right] \quad (1)$$

Here $\bar{\sigma}$ is the effective normal stress given by $\bar{\sigma} = \sigma - p$ where $p$ is the pore pressure, $f_0$ is a reference friction coefficient corresponding to a reference slip velocity $V_0$ at steady state (Ruina, 1983), and $D_c$ is the critical slip distance (Table 4-1). From a physical perspective, rate-and-state friction describes how asperity contacts on a fault surface evolve over time; $D_c$ represents the characteristic length scale over which a population of contacts on an interface changes from one steady state to another during sliding. The parameters $a$ and $b$ are temperature- and pressure-dependent properties of the material. In steady-state, the derivative of the rate-and-state friction coefficient with respect to velocity is proportional to $(a-b)$ (e.g., Scholz, 1998). When $(a-b) < 0$, small increases in slip velocity will result in a drop in the friction coefficient and slip will accelerate. This behavior is referred to as *velocity-weakening*. On the other hand, when $(a-b) > 0$, an increase in slip velocity will result in an increase in the friction coefficient, leading to a negative feedback on slip behavior known as *velocity-strengthening*. Slip instabilities (earthquakes) nucleate in velocity-weakening areas. Values of $(a-b)$ have been measured in the lab for some materials and

conditions (e.g., Blanpied et al., 1995; He et al., 2007). Assuming a typical geotherm, the $(a-b)$ profile for a typical crustal fault is characterized by a shallow region of velocity-strengthening material above a velocity-weakening zone where earthquakes nucleate. At greater depths the fault transitions back to velocity-strengthening as temperature and pressure increase (Scholz, 1998). Here we refer to the velocity-weakening region as the seismogenic zone.

In our simulations, a regularized version of the friction law is used when $V < 0.001$ mm/yr:

$$\tau = a\bar{\sigma}\sinh^{-1}\left[\frac{V}{2V_0}\exp\left(\frac{f_0 + b\ln(V_0\theta/D_c)}{a}\right)\right] \quad (2)$$

Equation (2) can be derived by solving Equation (1) for $V$ and replacing the factor $\exp(\tau/a\,\bar{\sigma})$ with $[\exp(\tau/a\,\bar{\sigma}) - \exp(-\tau/a\,\bar{\sigma})]$ to account for the possibility of backward slip when the slip velocity slows to near zero (Ben-Zion & Rice, 1997; Lapusta et al., 2000; Rice & Ben-Zion, 1996). The regularized law in Equation (2) avoids the singularity at $V = 0$ that occurs in the full friction law.

The critical slip distance $D_c$ is directly related to the critical earthquake nucleation size $h^*$, which is the minimum length scale that must fail in order for a slip instability to occur. Rate-and-state models with $h^*$ smaller than the dimensions of a grid cell will produce spurious results as single cells can generate instabilities independently of one another. To properly simulate stick-slip behavior, the model requires a critical nucleation size larger than a single cell. This is done by setting $h^*$ to be sufficiently large relative to the model grid size, and then relating $h^*$ to $D_c$ through the expression

$$h^* = \frac{2\mu b D_c}{\pi(b-a)^2\bar{\sigma}} \quad (3)$$

where $\mu$ is the shear modulus (Rubin & Ampuero, 2005).

During steady-state sliding, the state variable $\theta$ can be thought of as the average contact time of asperities on the interface (Dieterich, 1979; Ruina, 1983). This intuitive definition points to two main effects on the time evolution of $\theta$. The first is the slip velocity, which has a direct effect on how long asperities remain in contact. The second is the duration of periods of no slip, referred to in lab experiments as "hold" periods, during which recrystallization and fault "healing" can occur.

Expressions for the time rate of change of $\theta$ can be formulated in different ways to emphasize one or the other of these effects. Here we follow Liu et al. (2012) and employ the "aging" law for our calculations. The aging law, defined as

$$\frac{d\theta}{dt} = 1 - \frac{\theta V}{D_c} \tag{4}$$

retains the time-dependence of state variable evolution (Beeler et al., 1994; Dieterich, 1978, 1979; Marone, 1998). This allows friction to evolve on stationary contacts as is observed in laboratory experiments, as well as during sliding. Setting the left-hand side of Equation (4) to zero, it can be seen that the steady-state value of the state variable is $\theta_{ss} = D_c/V$.

The model couples the rate-and-state friction law and state variable evolution with quasi-static elasticity, in order to quantify the effect of slip on the spatial and temporal distribution of shear stress on the fault:

$$\tau(x,\xi,t) = \int_{-L/2}^{L/2}\int_{0}^{D} k(x-x',\xi,\xi')\left[\delta(x',\xi',t) - V_{pl}t\right]dx'd\xi' - \eta\frac{\partial\delta(x,\xi,t)}{\partial t} \tag{5}$$

Here $\tau$ is the shear stress, $x$ and $\xi$ are distance measured along-strike and downdip on the fault plane, $t$ is time, $\delta$ is slip distance, $V_{pl}$ is the "plate" velocity or forcing velocity, $L$ is the along-strike dimension of the fault, $\eta$ is a viscous damping factor, and $k$ is the stiffness kernel which we obtain from closed-form solutions (Okada, 1992) based on the fault geometry. The two terms on the right-hand side of Equation (5) describe the quasi-static equilibrium connection between shear stress and slip, and the effects of viscous damping at very high slip rates, respectively. The damping term can be thought of as the energy dissipated by seismic waves. The damping factor $\eta$ is chosen to be $\mu/2c$, where $\mu$ is the shear modulus and $c$ is the shear wave speed. This value of $\eta$ ensures that the slip velocity is bounded by a value on the order of $c\Delta\tau/\mu$ where $\Delta\tau$ is an average stress drop for a slip instability (Lapusta & Liu, 2009; Rice, 1993). The double integral term in Equation (5) is an approximation to the full elastodynamic response and does not reproduce wave propagation effects along the fault during a slip instability. In the exact solution the product of stiffness $k$ and slip $\delta$ would be a convolution in time to account for the finite velocity at which stress alterations due to

slip propagate along the fault. Using the quasi-static approximation communicates those stress changes along the fault instantaneously to avoid the computational expense of the time convolution. Therefore, although it cannot be used to model dynamic rupture processes, this approach provides a good approximation for timescales covering several earthquake cycles (Lapusta & Liu, 2009).

To simulate slip on a two-dimensional fault plane we use a boundary integral approach to calculate the evolution of slip velocity through time. Differentiating the friction law and the quasi-static elastic relation gives two equations for the time derivative of $\tau$, which can be equated and solved to find the time derivative of the slip velocity. The fault surface is discretized into rectangular grid cells with the slip velocity $V$ and state variable $\theta$ specified in each cell. The discretized stiffness kernel is calculated for each grid cell using closed-form solutions for shear displacement on a fault plane in an elastic half-space (Okada, 1992). For a plate rate $V_{pl}$ we impose an initial slip velocity $V_0$ as the portion of the horizontal plate velocity resolved on the fault surface, and set the initial state variable to a value slightly out of steady state at $\theta_0 = D_c/(1.1 * V_0)$. The model then evolves both quantities in time using the time derivative of velocity and the aging law for state variable evolution given by Equation (4) (Beeler et al., 1994; Rice, 1993; Ruina, 1983). The model steps forward in time using a 5th-order Cash-Karp Runge-Kutta method with an adaptive stepsize control (Cash & Karp, 1990).

For each simulation we specify the thermal gradient, fault dip, forcing velocity, and along-strike fault length (Figure 4-2, Table 4-2). The friction parameter $(a - b)$ is mapped onto the fault surface based on the imposed temperature structure, using relationships from laboratory data for either granite or gabbro (Blanpied et al., 1995; He et al., 2007).

We use the modeled cumulative fault slip to calculate the seismic coupling coefficient for each simulation. The coupling coefficient is determined from the ratio of seismic slip (defined when the slip velocity exceeds the threshold velocity) to the total fault slip (defined as plate rate times the total elapsed time). We excluded slip near the edges of faults because edge effects tend to suppress slip close to the boundaries. We found that running simulations for 300 years allowed sufficient time for the coupling coefficient to converge to a stable value. The coupling coefficient for each simulation is taken to be the value at the end of the run, and the uncertainty in the coupling coefficient is estimated from the range of values over the run excluding the first simulated earthquake, which

induces a large jump in coupling coefficient as the system adjusts to the initial conditions (see Liu et al., 2012, Figure 3) (Table 4-2).

### 4.4 Rate-and-state model results

In our simulations, the imposed thermal gradient (Figure 4-2a) determines the distribution of the friction parameter $(a - b)$, which in turn sets the downdip width of the seismogenic zone ($W$) (Figure 4-2b and 4-3a, e). Figure 4-3 compares the general behavior of a simulation case with large $W$ (Figure 4-3a–d) versus a case with moderate $W$ (Figure 4-3e–h). At each time step, we calculate the maximum slip velocity on the fault (Figure 4-3c, g). Slip instabilities are easily identified as sharp spikes in the maximum velocity time series. The model also calculates the cumulative distance that the fault has slipped, averaged over the seismogenic zone. Cumulative slip is tracked at regular time intervals to capture the progress of interseismic slip. Slip is also tracked when the maximum slip rate exceeds a given velocity threshold to capture coseismic slip (Figure 4-3b, f). To test the sensitivity of our results to the assumed threshold velocity, we tracked coseismic slip using two threshold velocities of 1 mm/s and 5 mm/s.

For the case with $W = 9.1$ km, earthquakes occur across almost the entire width of the fault at regular intervals (Figure 4-3b, c). By contrast, when $W = 5.7$ km, earthquakes occur at irregular intervals and do not rupture all the way across the fault (Figure 4-3f, g). We quantify the differences between the two simulations by calculating the ratio of the cumulative seismic slip to the total slip throughout each simulation, averaged over the seismogenic zone (Figure 4-3d, h). The coupling coefficient decreases slowly during interseismic periods and increases abruptly when earthquakes occur. Over time the jumps in coupling due to earthquakes become smaller, as the cumulative total slip increases and each successive event has a smaller effect on the ratio. In the case with larger $W$, the coupling coefficient converges to a stable value of 0.69 assuming a threshold velocity of 1 mm/s (Figure 4-3d). For the case with smaller $W$, a larger fraction of the total fault slip occurs aseismically, so the coupling coefficient converges to a much lower value of 0.19 (Figure 4-3h). We find that these estimates are not strongly sensitive to the choice of the threshold velocity for seismic slip. For example, if we assume a threshold of 5 mm/s instead of 1 mm/s, the coupling coefficients for these two simulations decrease to 0.67 and 0.11, respectively.

We systematically investigated the effects of fault dip, thermal gradient, plate rate, and along-strike fault length on seismic coupling in the model (Figure 4-4; Table 4-2). As anticipated, the plate rate used to drive the model does not affect the seismic coupling coefficient (Figure 4-4a) because it does not appear in the state variable evolution law or the rate-and-state friction law. This also demonstrates that the seismic coupling coefficient calculated at the end of each model run was not influenced by using the plate rate as the initial condition for the fault slip rate when spinning up the model. However, the earthquake recurrence interval does decrease systematically with increasing spreading rate when all other variables are held equal. This is expected because the plate rate is required to calculate the accumulated stress in Equation (5).

To mimic the typical length of mid-ocean ridge normal faults, we examined along-strike fault lengths of 25–50 km and found that seismic coupling was not affected by the along-strike fault length within that range. In test cases using a much smaller along-strike dimension similar to or smaller than $W$, we found that very short faults $(L < W)$ suppress earthquake nucleation in the model, suggesting that an equivalent characteristic nucleation length is also required for the along-strike dimension.

Variations in fault dip and the vertical thermal gradient have a pronounced influence on the coupling coefficient (Figures 4-4b & 4-4c, respectively). Specifically, when $h^*$ is held constant coupling increases with decreasing fault dip and for colder thermal gradients. To interpret these variations we ran an additional series of models holding spreading rate, fault dip, and the vertical thermal gradient constant and varying $h^*$. These simulations show that the seismic coupling coefficient increases systematically with decreasing $h^*$, consistent with previous results on thrust (e.g., Liu & Rice, 2007) and strike-slip (e.g., Liu et al., 2012) faults. We therefore infer that the sensitivity of seismic coupling to fault dip and thermal gradient is related to their respective roles in controlling the down-dip width of the seismogenic layer $W$. For constant $h^*$, the coupling coefficient scales with $W$ regardless of whether $W$ is changed by varying the thermal structure or the fault dip.

Our model results indicate that seismic coupling on normal faults is strongly controlled by the down-dip width of the seismogenic zone $W$ relative to the critical nucleation patch size $h^*$. Following Liu et al. (2012), we quantify this relationship by plotting the seismic coupling coefficient $\chi$ against the dimensionless ratio $W/h^*$ for each run (Figure 4-5). We completed 110 model runs in

which $W$ and $h^*$ were varied independently by systematically changing fault dip, lithology, thermal gradient, and $D_C$. In all these runs, the seismic coupling coefficient was primarily sensitive to the value of $W/h^*$ regardless of which parameter was changed (Table 4-2). Specifically, we find that $\chi$ goes to zero (completely aseismic slip) for $W/h^* \leq 1.3$, jumps to ~0.7 for $W/h^* > 2$, and increases to ~0.90 when $W/h^*$ exceeds 5.

There were no resolvable differences in the seismic coupling coefficient between simulations where frictional parameters were based on laboratory data from gabbro versus granite samples. Figure 4-5 shows that seismic coupling for both materials falls along the same trend with $W/h^*$. The details of the distribution of $(a-b)$ as a function of depth are slightly different for the two materials, with gabbro reaching slightly less negative values compared to granite (Figure 4-2b) (Blanpied et al., 1995; He et al., 2007). However, in both cases the overall profile for a crustal fault goes from shallow velocity-strengthening, through a velocity-weakening seismogenic zone, and back to velocity-strengthening at depth. The $(a-b)$ distribution sets the value of $W$, and $(a-b)$ also factors into the value of $h^*$ through Equation (3); thus, the differences in frictional parameters between these two materials are reflected in $W/h^*$.

## 4.5 Discussion

The models presented above indicate that the seismic coupling coefficient for normal faults scales with the ratio of the width of the seismogenic layer to the critical earthquake nucleation size ($W/h^*$). We now contrast these model results with previous rate-and-state models of oceanic transform faults, and compare our new normal fault simulations with observations from mid-ocean ridge normal faults. Finally, we extend our results to a case with much thicker lithosphere to test whether our models also apply to continental rift systems.

### 4.5.1 Comparison of seismic coupling in oceanic normal and transform fault models

The scaling relationship between $\chi$ and $W/h^*$ that we derive for normal faults is similar in form to the relationship found by Liu et al. (2012) for oceanic transform faults (Figure 4-5). For suites of models the seismic coupling coefficient increases abruptly over a narrow range of $W/h^*$ values between 1 and 2. However, in the case of transform faults, Liu et al. (2012) found the seismic

coupling coefficient reached a fully coupled value of 1 for $W/h^* > 2$. By contrast, we find that normal faults do not become fully coupled for $W/h^*$ values up to ~7.

Seismic coupling may be lower in the normal fault models because the faults we examined here are shorter in their along-strike dimension compared to the transform fault cases examined by Liu et al. (2012). To mitigate edge effects in our models we excluded fault slip adjacent to the fault edges from the summations of cumulative moment release; however, the length of the faults may limit the total seismic moment release. The along-strike lengths of the transform fault models of Liu et al. (2012) mimicked the lengths of natural oceanic transforms, while the normal fault lengths in this study were chosen to match the observed lengths of normal fault scarps on the seafloor. The transform models with the longest faults (500 km) resulted in distinctly higher seismic coupling than the shorter transforms (100–300 km) before full coupling is reached (Liu et al., 2012). To test whether along-strike length was limiting the coupling coefficient in our models we ran cases with 400 and 500 km long normal faults, and found that increasing the along-strike fault length resulted in seismic coupling closer to that observed in transform models with similar $W/h^*$. In reality, such large along–strike fault lengths are not representative of oceanic normal faults, where first and second order spreading segments are typically <100 km in length (e.g., Macdonald et al., 1991, 1992). This underscores the importance of basing quantitative interpretations of oceanic normal fault behavior on models calculated with appropriate fault geometries.

Another difference between our normal fault models and those calculated for oceanic transforms is that the normal fault models include effects due to varying fault dip on seismic coupling beyond the dependence of $W$ on dip. This dip effect derives from the influence of the free-surface, and will be more pronounced for normal faults as their average depth is less than that of a transform fault with the same value of $W$. However, most of our model runs were for relatively steep normal faults (<25% of the model runs used fault dips less than 50°), so free surface effects alone are unlikely to account for the difference between the normal and transform fault models.

### 4.5.2 Implications for seismic coupling at mid-ocean ridges

We quantitatively compare the predictions of our models with observations at mid-ocean ridges. To do this, we first fit the model outputs of $W/h^*$ versus $\chi$ with the empirical function

$$\chi = 10^{c_1 + \tan^{-1}\left(\frac{\frac{W}{h^*} - c_2}{c_3}\right)} \quad (6)$$

This functional form was chosen because it follows the shape of an asymmetric sigmoid, thereby fitting both the region of low $W/h^*$ where $\chi$ is flat at 0 and the gradual increase in $\chi$ for large $W/h^*$. Equation (6) was fit to the model results with the Python package *scipy.optimize* using nonlinear least-squares and a trust-region minimization algorithm (Voglis & Lagaris, 2004). The individual model runs were binned before fitting because the full dataset is heavily weighted toward runs with $W/h^* \sim 2$. Fitting without bins favors a function with a sharp corner near $W/h^* \sim 2$ at the expense of fitting runs with $W/h^* > 5$. Using this approach, we obtained optimal parameters of $c_1 = -1.60$, $c_2 = 1.46$, and $c_3 = 0.16$ (Figure 4-5).

To compare these estimates of coupling to data from natural systems, we use observations of moment release rate normalized by spreading rate and segment length. The coupling coefficient can be related to the normalized moment release rate $\dot{M}_0$ by

$$\chi = \frac{\dot{M}_0 \sin\varphi}{V_{pl}\mu H(1 - M)} \quad (7)$$

where $H$ is the thickness of the seismogenic layer, and $M$ is the fraction of plate separation accommodated by magmatism (i.e., not on faults) (Buck et al., 2005; Olive & Escartín, 2016). Combining Equation (7) with our functional fit to the model results (Equation (6)), we solve for the moment release rate as a function of seismogenic layer thickness, and then explore the sensitivity of this relation to the assumed values of $M$ and $h^*$. Earthquakes in the oceanic lithosphere are generally observed to occur shallower than the 600°C isotherm (e.g., Bergman & Solomon, 1984; W.-P. Chen & Molnar, 1983; Mckenzie et al., 2005; Wiens & Stein, 1984), and the transition from velocity-weakening to velocity-strengthening in olivine is also thought to occur near that temperature (Boettcher et al., 2007). Thus, we relate the seismogenic layer thickness to the observed spreading rate using the thermal model of Montési and Behn (2007). Specifically, we calculate the on-axis depth to the 600°C isotherm, assuming a high thermal diffusivity of $\kappa = 4 \times 10^{-6}\ \mathrm{m^2/s}$ in order to

account for the effects of hydrothermal circulation (Phipps Morgan et al., 1987; C. A. Stein & Stein, 1992).

Figure 4-6a shows observations from mid-ocean ridges with curves calculated using Equation (7) with constant $h^*$ and varying $M$. With $h^* = 1$ km, the mid-ocean ridge data are best fit by $M = 0.85 - 0.95$, and are ill fit by much smaller $M$ values. Figure 4-6b shows the same data, but with curves using constant $M = 0.9$ and varying $h^*$. The mid-ocean ridge data appear best fit by a value of $h^* \sim 1$ km and observations for seismogenic layer thicknesses <5 km cannot be fit by $h^* > \sim 2.5$ km.

A least-squares fit to the observations from mid-ocean ridges gives best-fit parameters of $M = 0.93$ and $h^* = 1.6$ km. The $M$ value is roughly consistent with previous observations of seismic moment release (Solomon et al., 1988) and cumulative fault slip (Behn & Ito, 2008; Escartín et al., 1999; Howell et al., 2016), which indicate that 70–90% of plate separation at mid-ocean ridges is accommodated by magma intrusion.

The value of $h^*$ in natural systems is a topic of some debate. Laboratory measurements of $D_c$ predict very small $h^*$ ($D_c \sim 10\ \mu$m, $h^* \sim 5$ m) (Boettcher et al., 2007), while rate-and-state models such as those used in this and other studies (e.g., Liu et al., 2012; Liu & Rice, 2007) require $D_c$ and $h^*$ orders of magnitude larger than the laboratory values in order to fit observations. Here, we find that although an $h^*$ of 5 m can fit observations at large seismogenic layer thickness ($H > 8 - 10$ km), the optimal value $h^* = 1.6$ km is much larger in line with previous rate-and-state modeling studies. It is noteworthy that $D_c$ may scale with gouge size (e.g., Marone & Cox, 1994), in which case laboratory measurements on small samples would not be directly applicable to much larger natural faults.

If $h^*$ represents the minimum length scale that must fail in order to nucleate an earthquake, then $h^*$ values on the order of kilometers pose a problem for small earthquakes. For example, with the $h^*$ values used in our models, we cannot produce earthquakes with $M_W < 4$, which involve rupture lengths shorter than ~1 km. Some studies suggest that the nucleation length scale varies with the size of the following event (Dodge et al., 1996; Ellsworth & Beroza, 1995), while others have argued

that the self-similarity of earthquake rupture processes breaks down below some threshold for small earthquakes (e.g., Jin et al., 2000). Either possibility would allow for different characteristic nucleation length scales to govern different scales of earthquakes. For example, small repeating earthquakes of $M_W < 4$ can be simulated within a velocity–weakening asperity of $h^*$~50–100 m embedded in a velocity–strengthening background (T. Chen & Lapusta, 2009). In this case, seismic coupling at the scale of the asperity directly scales with the ratio of the patch size to $h^*$. Small events may thus be related to asperity-scale processes while larger events could be controlled by mechanical processes averaged over many asperities. Further, $h^*$ may vary spatially due to fault zone heterogeneity, allowing different scales of events to occur on different parts of a fault.

In summary, the value of $h^*$ in natural systems remains a question, as models like ours do not fully agree with laboratory values. The observations are best fit by $h^* = 1.6$ km, a much larger value than has been previously obtained from laboratory experiments. Detailed studies of the source parameters of small earthquakes $(M_W < 4)$ may help bridge the gap between laboratory measurements of $h^*$ and the nucleation length scales of large faults.

An important outcome of our modeling is that the expected variations in ridge thermal structure and fault geometry are sufficient to generate the variations in seismic coupling observed at mid-ocean ridges, and that material heterogeneities are not required to explain the observations. Of course, hydrous alteration and fluid circulation play an important role in fault zones, and incorporating heterogeneous materials in models can provide insight into higher-order complexities of the seismic cycle (e.g., Barbot et al., 2012). However, the fact that our model accurately predicts seismic coupling at mid-ocean ridges using a reasonable $M$ value shows that hydrous alteration and heterogeneous fluid pressures are not required to explain first-order trends of seismic coupling across mid-ocean ridges.

### 4.5.3 Seismic coupling in thicker lithosphere: Applications to continental rift systems

Our model predicts that fault geometry and ridge thermal structure control seismic coupling on oceanic normal faults through their influence on the width of the seismogenic zone, in agreement with observations from mid-ocean ridges. However, the mid-ocean ridge data shown in Figure 4-6

are limited to relatively thin oceanic lithosphere ($H < \sim 10$ km). Moreover, even at slow spreading ridges the fraction of extension accommodated by magma is thought to be relatively high with $M > 0.7$ (Behn & Ito, 2008), with the exception of regions immediately adjacent to detachment faults (Behn & Ito, 2008; Tucholke et al., 2008), which ultimately account for a small fraction of total ridge length. Thus, to further test the applicability of our normal fault models, we must look toward data from systems with thicker lithosphere and lower magma fluxes, such as continental rifts.

Existing estimates of seismic coupling for continental rift systems are based on global averages of seismic moment release rates, and are not significantly different from estimates of coupling for slow-spreading mid-ocean ridges (Bird & Kagan, 2004; Olive & Escartín, 2016). This could be due to the large uncertainty in estimates of seismic coupling for continental rifts. Globally averaged estimates of coupling in continental rifts rely on assumptions for the fault dip and thickness of the seismogenic layer. Using data from multiple rift systems involves large uncertainties on these assumptions, which in turn propagates into large uncertainty in the inferred seismic coupling coefficient. Moreover, most individual rifts lack seismic catalogs of sufficient time length to capture multiple seismic cycles, precluding estimates of seismic coupling for individual rifts.

To address these limitations, we estimated seismic coupling for the Corinth rift, a single, well-studied rift system located in the Gulf of Corinth where tighter constraints can be placed on fault dip and seismogenic layer thickness based on local structural geology and seismic data. We chose to focus on the Corinth rift because a local seismic catalog spanning 40+ years was available for analysis (Makropoulos et al., 2012), complete down to $M_L = 3.7$ (Wiemer & Wyss, 2000). Extensive information is also available on regional structure, and the distribution of seismicity suggests that the seismogenic layer is between 10 and 20 km thick (Armijo et al., 1996; Beckers et al., 2015; Bell et al., 2009; Bernard et al., 1997; Briole et al., 2000; Chouliaras et al., 1997; Clément et al., 2004; Lambotte et al., 2014; Micarelli et al., 2003; Moretti et al., 2003; Rigo et al., 1996; Taylor et al., 2011; Zelt et al., 2005). We estimated the seismic coupling coefficient for the Corinth rift using both the local catalog with moment conversions (Deichmann, 2006, 2017; Hanks & Boore, 1984; Papazachos et al., 1997), and data from the ISC catalog (International Seismological Centre, 2017). The methods used to calculate the coupling coefficient are described in detail in the Supplemental Information. We find that faults in the Corinth rift are likely to be fully or almost fully coupled, with a coupling coefficient

of 1 ± 0.3. This is significantly different from observations at slow-spreading mid-ocean ridges where the coupling coefficients are ~0.1–0.6 (Olive & Escartín, 2016).

Predictions from our normal fault models can match the normalized moment release rate for the Corinth rift with $M = 0$, consistent with the absence of magmatic activity in this rift, and with the same approximate $h^*$ value of 1 km as fits the mid-ocean ridge data (Figure 4-6a). We stress that the Corinth rift is only one example of coupling in a continental rift and cannot be used to conclude that our models apply across all divergent plate boundaries. However, it does suggest that these models may be applicable in thicker lithosphere and in settings with different time-averaged magmatic strain accommodation. As previously mentioned, it is difficult to estimate coupling in most individual rift systems because of a lack of data, but future studies should test the model predictions presented here by estimating seismic coupling in other locations where sufficient data can be found.

### 4.6 Conclusions and perspectives

Analysis of earthquake catalogs at mid-ocean ridges reveals that the energy associated with repeated seismic ruptures falls short of the moment release expected for observed long-term slip on normal faults. This observation suggests that aseismic slip is essential to the accumulation of offset on mid-ocean ridge normal faults.

One end-member explanation is that the fault surface is mechanically heterogeneous and only hosts a few patches capable of rupturing in a seismic manner. Normal faulting earthquakes as large as $M_w \sim 5 - 6$ (typically associated with rupture lengths ~10 km) have, however, been observed at fast-spreading ridges, suggesting that the weak seismic coupling characteristic of these settings cannot be explained solely by seismogenic slip being confined to small, isolated patches. Further, the heterogeneity model provides no straightforward explanation for why the seismic moment deficit is greater at faster spreading mid-ocean ridges.

The alternative explanation we consider here postulates that a reduction in the size of the seismogenic zone hinders the nucleation of slip instabilities on normal faults. This favors a mixed mode of slip where normal fault growth occurs through both aseismic transients and earthquakes that repeatedly rupture the same areas. The hotter thermal regime associated with faster spreading

rates reduces the extent of the seismogenic zone, which shifts the balance towards fewer earthquakes, more aseismic transients, and lower seismic coupling. This explanation is favored by models of strike-slip and thrust faults, but had not previously been tested in models with the specific geometry of normal faults.

In this study, we present a suite of normal fault models to test whether variations in the size of the seismogenic zone could produce the range of seismic coupling observed in natural systems. Our models show that this effect can account for the observed trend of seismic moment release rate versus seismogenic layer thickness (Figures 4-1 and 4-6), provided the characteristic nucleation size of earthquakes ($h^*$) is of order 1 km. The models fit observations from mid-ocean ridges with $M = 0.85 - 0.95$, and can explain observed moment release rates in the Corinth rift with $M = 0$. We find a relationship between seismic coupling and $W/h^*$ similar to that seen in transform fault models, but the shorter length of mid-ocean ridge normal faults may limit seismic coupling for large $W/h^*$ compared with long oceanic transforms.

While our models show that variations in the width of the seismogenic zone can explain the first order trends in observations from mid-ocean ridges, other factors may also contribute to local variability. For example, fault behavior likely also reflects the combined effects of frictional heterogeneities, geometric complexity of the fault zone, and some degree of tectono-magmatic interaction, as well as the finite extent of the seismogenic zone. A satisfying mechanism or combination of mechanisms to explain segment-to-segment variability will need to account for not only the magnitude of the seismic deficit at mid-ocean ridges, but also for the trends in seismic deficit across spreading rates. Future work building on this understanding of first-order controls on seismic coupling for normal faults can begin to target more complex controls on normal fault seismicity. Models could combine a rate-and-state framework with time-dependent magmatism to look at the effects of dike intrusions on seismic cycles. Further, seismic and geodetic observations of discrete continental rifting events from well-instrumented rift systems (e.g., Calais et al., 2008; Ebinger et al., 2010; Keir et al., 2006) can help us understand the interplay between magmatism and tectonic extension at divergent boundaries over a wider range of seismogenic layer thicknesses and $M$ values than are found in the oceans.

## 4.7 Acknowledgments and Data

Funding was provided by an NSF Graduate Research Fellowship (HM), NSF Awards OCE-10-61203 (MB, YL) and EAR-10-10432 (MB) and a WHOI IR&D Award (MB). We thank P. Cowie and L. Lavier for their thoughtful reviews of this paper. The data used are listed in the references and Table 4-2.

### 4.8 Figures and tables

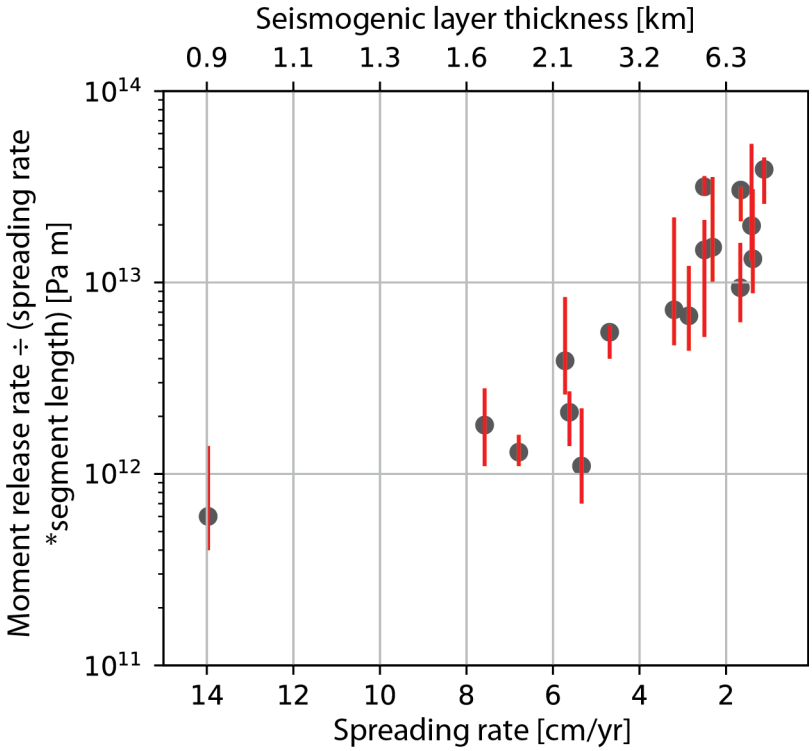


**Figure 4-1.** Seismic moment release rate at divergent plate boundaries normalized by boundary length and spreading rate (a proxy proportional to the seismic coupling coefficient, Frohlich & Wetzel, 2007; Olive & Escartín, 2016), plotted against spreading rate and seismogenic layer thickness. Seismogenic layer thickness estimated from the on-axis depth of the 600ºC isotherm as predicted by the model of Montési and Behn (2007). See Section 4.5 for details.

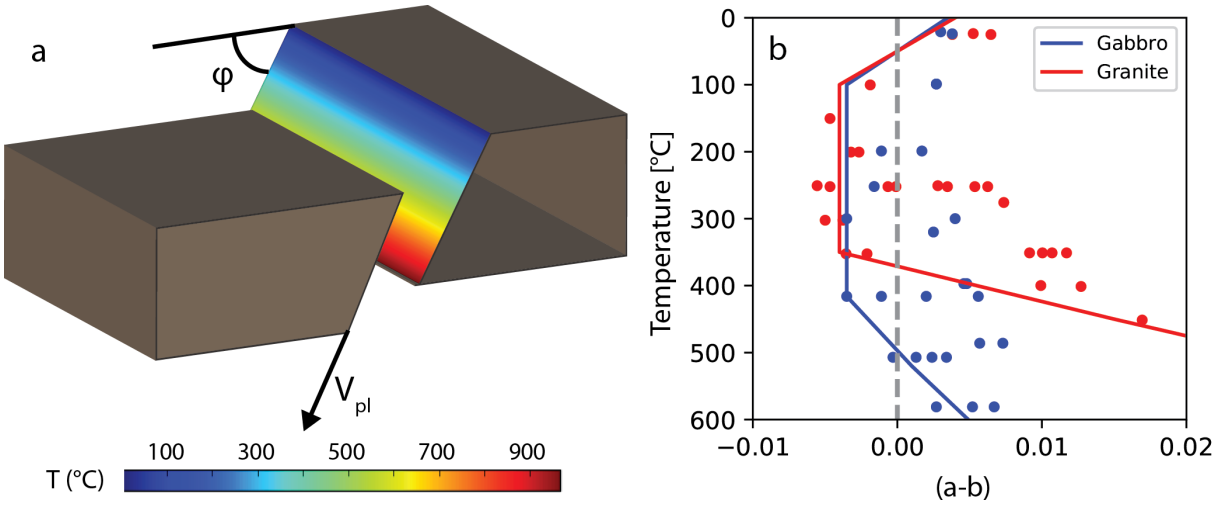


**Figure 4-2. (a)** 3-D schematic diagram of the model setup showing fault dip ($\varphi$), imposed slip velocity at the base of the fault ($V_{pl}$), and temperature on the fault plane. **(b)** Frictional parameter $(a - b)$ for gabbro (blue) and granite (red) are shown as a function of temperature. Dots show data from laboratory experiments (Blanpied et al., 1995; He et al., 2007); curves show simplified fits to these data used in our simulations. The scatter in the data at each temperature is due to experimental runs at different normal stress conditions and/or different size steps for velocity increases or decreases.

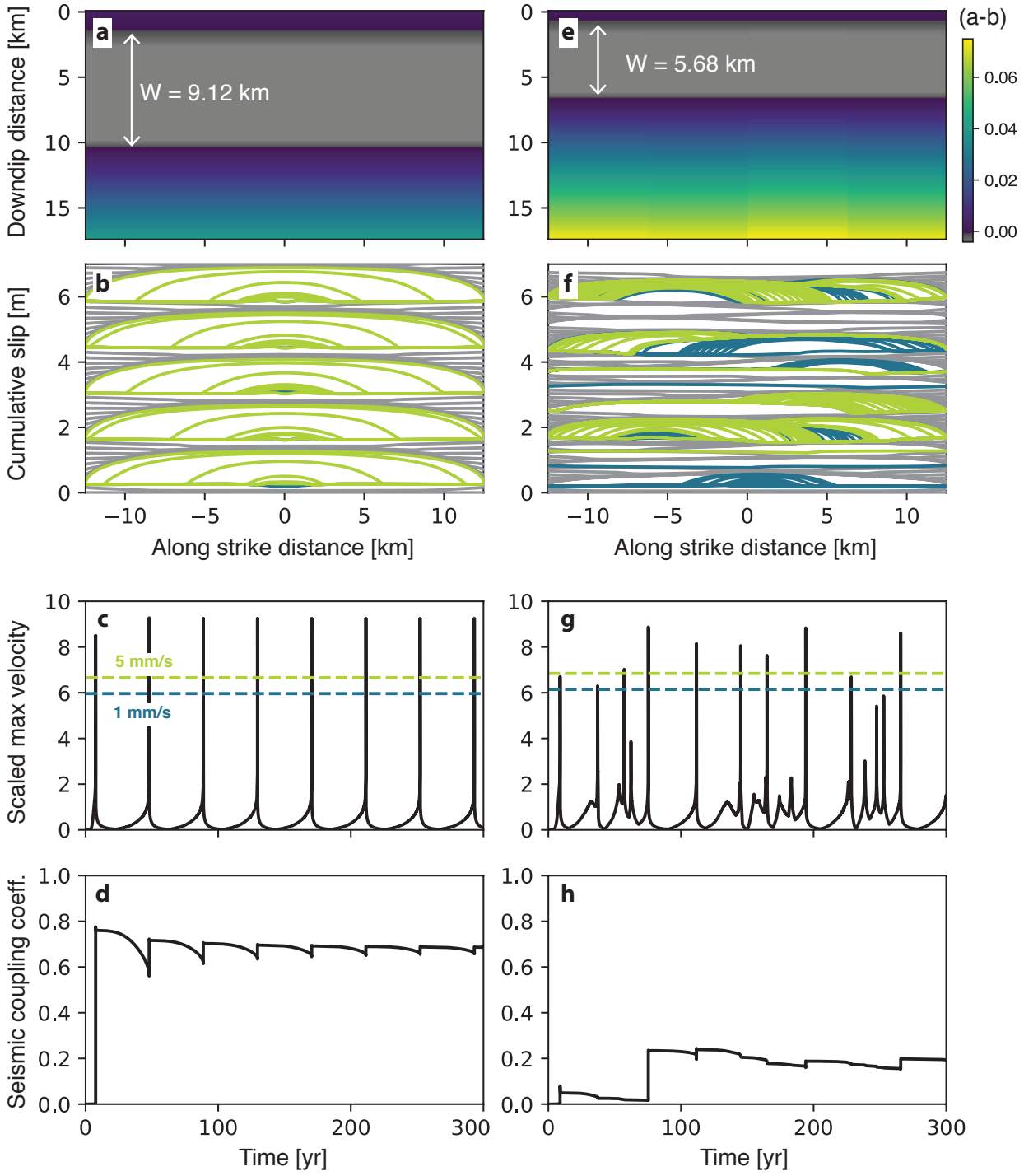
a
W = 9.12 km
e
W = 5.68 km
(a-b)
0.06
0.04
0.02
0.00
Downdip distance [km]
b
f
Cumulative slip [m]
Along strike distance [km]
Along strike distance [km]
c
g
5 mm/s
1 mm/s
Scaled max velocity
d
h
Seismic coupling coeff.
Time [yr]
Time [yr]

**Figure 4-3.** Model results for two simulations, with $W = 9.1$ km (*d40t55hs10*, left column) and $W = 5.7$ km (*u1hs12*, right column). Both simulations use $h^*$~3.5 km and $V_{pl} = 4.5$ cm/yr. **(a, e)** Imposed distribution of $(a - b)$ on the fault surface. **(b, f)** Cumulative slip contours averaged over the seismogenic zone. Grey lines show interseismic slip, contoured at 5-year intervals. Blue lines show slip at velocities >1 mm/s, contoured at 200-second intervals. Green lines show slip at velocities >5 mm/s, contoured at 15-second intervals. **(c, g)** Log of maximum slip velocity scaled by the plate rate, as a function of time. **(d, h)** Seismic coupling coefficient through time.

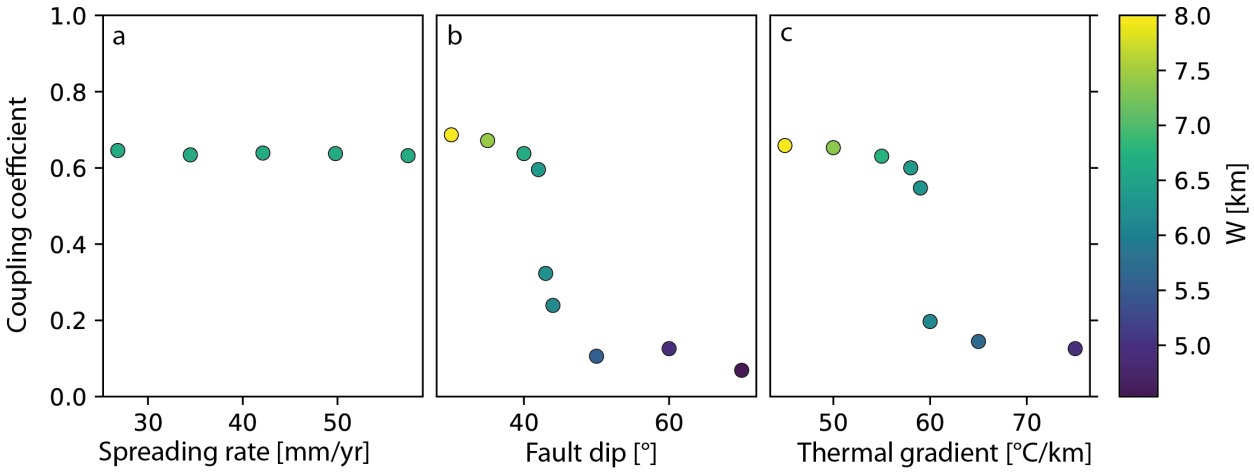


**Figure 4-4.** Calculated seismic coupling coefficient as a function of **(a)** spreading rate, **(b)** fault dip, and **(c)** vertical temperature gradient. $h^*$ is ~3.6 km in all model runs, and points are colored by the width of the seismogenic zone. We find that spreading rate does not affect seismic coupling; however, coupling varies systematically with fault dip and the vertical thermal gradient. As discussed in the text, we infer the sensitivity of the coupling coefficient to fault dip and thermal gradient is related to the influence of these parameters on the width of the seismogenic zone.

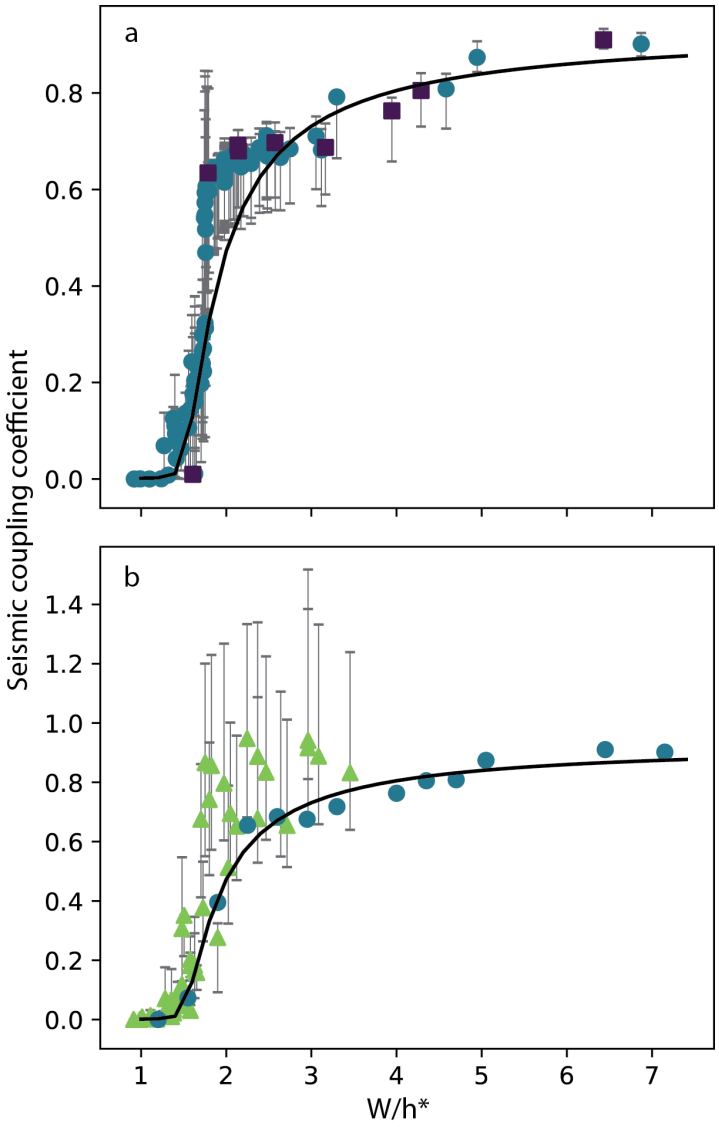


**Figure 4-5. (a)** Seismic coupling coefficient plotted against $W/h^*$ for all model runs listed in Table 4-2: purple squares correspond to runs with $(a-b)$ based on granite (Blanpied et al., 1995), and blue circles are for runs with $(a-b)$ based on gabbro (He et al., 2007). Uncertainty estimates are based on the range of coupling excluding the first slip instability of each model run. The black line shows the fit of Equation (6) to the binned data points shown in the lower panel (see Section 4). **(b)** Results from the transform fault models of Liu et al. (2012) are plotted as green triangles, and bin averages of the points in (a) are shown by blue circles. The black line is again the fit to the bin averages.

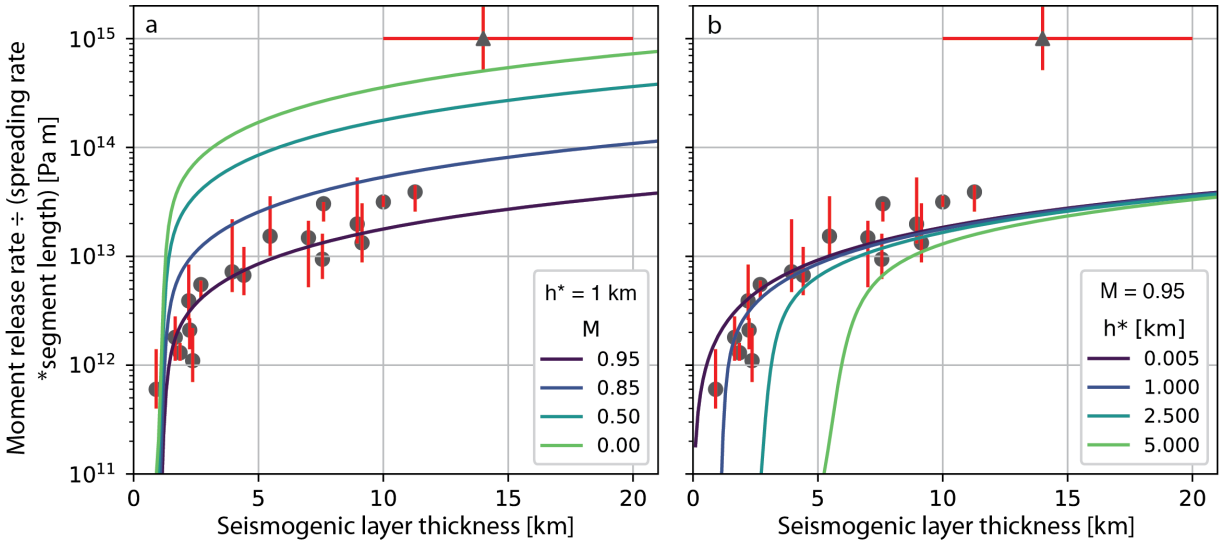


**Figure 4-6.** Observations of seismic moment release rate normalized by spreading rate and segment length versus estimated seismogenic layer thickness for mid-ocean ridges (circles, Frohlich & Wetzel, 2007; Olive & Escartín, 2016) and the Corinth rift (triangle, this study). The moment release rate for Corinth is calculated using a spreading rate of 13 mm/yr and a segment length of 90-107 km. **(a)** Model predictions (colored lines) are calculated assuming different values of $M$ and $h^* = 1$ km. The mid-ocean ridge data are best fit by $M$ between 0.85 and 0.95, while the Corinth rift point falls closest to the $M = 0$ line. This is consistent with expectations for the amount of magmatic strain accommodation in these settings. **(b)** Model predictions (colored lines) calculated from the empirical fit in Figure 4-5 with $M = 0.95$ and different values of $h^*$. In thinner lithosphere, the data are best fit by $h^* \sim 1$ km, while in thicker lithosphere, multiple values of $h^*$ fit the data equally well.

**Table 4-1.** List of model parameters and their values or ranges.

| Variable | Meaning | Value/units |
|---|---|---|
| $\boldsymbol{V_{pl}}$ | Plate rate | 25–75 mm/yr |
| $\boldsymbol{\frac{dT}{dz}}$ | Vertical thermal gradient | 45–127 °C/km |
| $\boldsymbol{\varphi}$ | Fault dip | 25–70° |
| $\boldsymbol{L}$ | Along-strike fault length | 25–50 km |
| $\boldsymbol{D_C}$ | Critical slip distance | 3–18 mm |
| $\boldsymbol{h^*}$ | Critical earthquake nucleation length scale | 1.0–6.6 km |
| $\boldsymbol{W}$ | Downdip width of seismogenic zone | 4.5–11.5 km |
| $\boldsymbol{\mu}$ | Shear modulus | 30 GPa |
| $\boldsymbol{(a-b)}$ | Friction parameter | –0.004–0.015, dimensionless |
| $\boldsymbol{c}$ | Shear wave speed | 3.044 km/s |
| $\boldsymbol{\eta}$ | Viscous damping factor | $\mu/2c$ |

**Table 4-2.** Model input parameters and calculated seismic coupling coefficients for all simulations run in this study. Each row of the table corresponds to one simulation, with a run name given in the first column. Subsequent columns contain values for $W/h^*$, $W$ [km], $h^*$ [km], the seismic coupling coefficient, the lower bound of the seismic coupling coefficient, the upper bound of the seismic coupling coefficient, fault dip [°], along-strike fault length [km], plate rate [mm/yr], and thermal gradient [°C/km].

| Model run | W/h* | W [km] | h* [km] | Coupling coeff. $\chi$ | $\chi$ lower bound | $\chi$ upper bound |
|---|---|---|---|---|---|---|
| d30w6hs10 | 0.92017 | 6.09375 | 6.62238 | 0 | 0 | 0 |
| u3hs20 | 0.98926 | 5.68329 | 5.74499 | 0.00017 | 0 | 0 |
| u2hs20 | 0.98926 | 5.68329 | 5.74499 | 0.00017 | 0 | 0 |
| u8hs18 | 1.09918 | 5.68329 | 5.17049 | 0.00002 | 0 | 0 |
| u3hs16 | 1.23658 | 5.68329 | 4.59599 | 0.00041 | 0.00003 | 0.00055 |
| h8d70t75 | 1.27083 | 4.55185 | 3.58179 | 0.069 | 0.00084 | 0.13741 |
| u1hs15 | 1.31901 | 5.68329 | 4.30874 | 0.00803 | 0.00001 | 0.01269 |
| h8d60t75 | 1.37894 | 4.93905 | 3.58179 | 0.12583 | 0.09186 | 0.15138 |
| d25whsC10 | 1.39642 | 6.02161 | 4.31217 | 0.1101 | 0.00429 | 0.16707 |
| d40w6hs10 | 1.40419 | 6.01628 | 4.28453 | 0.09392 | 0.06449 | 0.1445 |
| u1hs14 | 1.41323 | 5.68329 | 4.02149 | 0.04214 | 0.00054 | 0.04689 |
| u10hs10 | 1.42826 | 4.5331 | 3.17386 | 0.08101 | 0.00179 | 0.14951 |
| t80hs10 | 1.47068 | 4.66842 | 3.17433 | 0.06244 | 0.01763 | 0.17969 |
| u3hs13 | 1.52194 | 5.68329 | 3.73424 | 0.13615 | 0.00035 | 0.17883 |
| h8d50t75 | 1.55891 | 5.58368 | 3.58179 | 0.1059 | 0.01515 | 0.26577 |
| cth8t65 | 1.57858 | 5.68329 | 3.60026 | 0.14453 | 0.00667 | 0.19201 |
| d30whsC10 | 1.59585 | 6.02141 | 3.77317 | 0.24305 | 0.10265 | 0.33962 |
| g2hs16 | 1.60772 | 7.91601 | 4.92375 | 0.00979 | 0.00357 | 0.01495 |
| d45w6hs10 | 1.60894 | 5.96621 | 3.70817 | 0.17649 | 0.02447 | 0.2942 |
| d30hs10 | 1.63047 | 8.55469 | 5.24676 | 0.01082 | 0.01013 | 0.01467 |
| d60hs10 | 1.63047 | 4.93905 | 3.02922 | 0.15981 | 0.13009 | 0.37863 |
| u9hs10 | 1.63047 | 4.93905 | 3.02922 | 0.20457 | 0.13009 | 0.37863 |
| d48hs10 | 1.63047 | 5.75573 | 3.5301 | 0.19619 | 0.05828 | 0.31389 |
| d40hs10 | 1.63047 | 6.65437 | 4.08125 | 0.17648 | 0.013 | 0.2052 |
| d70hs10 | 1.63047 | 4.55185 | 2.79174 | 0.23907 | 0.16103 | 0.35756 |
| d50hs10 | 1.63047 | 5.58368 | 3.42458 | 0.20257 | 0.06429 | 0.30178 |
| t75hs10 | 1.63047 | 4.93905 | 3.02922 | 0.15981 | 0.13009 | 0.37863 |
| u1hs12 | 1.64877 | 5.68329 | 3.447 | 0.19371 | 0.01676 | 0.24375 |
| ht8t65 | 1.67329 | 5.68329 | 3.39648 | 0.2273 | 0.09038 | 0.28761 |
| cth8t60 | 1.70467 | 6.1569 | 3.61178 | 0.19693 | 0.03482 | 0.2219 |
| h8d44t75 | 1.71911 | 6.15748 | 3.58179 | 0.23922 | 0.09126 | 0.27329 |
| u3hs115 | 1.72045 | 5.68329 | 3.30337 | 0.26544 | 0.09934 | 0.26786 |

| Model run | W/h* | W [km] | h* [km] | Coupling coeff. $\chi$ | $\chi$ lower bound | $\chi$ upper bound |
|---|---|---|---|---|---|---|
| u1hs115 | 1.72045 | 5.68329 | 3.30337 | 0.29828 | 0.08317 | 0.29931 |
| d48w6hs10 | 1.73318 | 5.99227 | 3.45738 | 0.22284 | 0.07813 | 0.2631 |
| t72hs10 | 1.73321 | 5.14203 | 2.96677 | 0.27024 | 0.12766 | 0.31168 |
| u8hs1135 | 1.74319 | 5.68329 | 3.26028 | 0.54152 | 0.31889 | 0.55561 |
| cth8t59 | 1.74997 | 6.29222 | 3.59561 | 0.54723 | 0.24826 | 0.54991 |
| u8hs113 | 1.7509 | 5.68329 | 3.24592 | 0.57294 | 0.34272 | 0.58234 |
| h8d43t75 | 1.75102 | 6.27178 | 3.58179 | 0.32317 | 0.0867 | 0.40514 |
| d35whsC10 | 1.75199 | 6.0218 | 3.43712 | 0.5936 | 0.35259 | 0.59932 |
| d49w6hs10 | 1.75621 | 5.97809 | 3.40397 | 0.3127 | 0.1558 | 0.35029 |
| t71hs10 | 1.75673 | 5.20968 | 2.96555 | 0.51739 | 0.22532 | 0.52629 |
| u2hs1125 | 1.75868 | 5.68329 | 3.23156 | 0.4694 | 0.19314 | 0.47871 |
| h7d70t65 | 1.76242 | 5.23775 | 2.97192 | 0.60618 | 0.439 | 0.62381 |
| u8hs112 | 1.76654 | 5.68329 | 3.21719 | 0.59969 | 0.38602 | 0.60595 |
| d50w6hs10 | 1.77538 | 5.96612 | 3.36048 | 0.60018 | 0.38712 | 0.61315 |
| t70hs10 | 1.77755 | 5.27734 | 2.96889 | 0.61192 | 0.41452 | 0.61486 |
| h8d42t75 | 1.78469 | 6.39239 | 3.58179 | 0.59556 | 0.34563 | 0.60138 |
| g1t85 | 1.78661 | 6.02158 | 3.37039 | 0.63448 | 0.48098 | 0.65626 |
| cth8t58 | 1.79259 | 6.42753 | 3.58562 | 0.6001 | 0.3905 | 0.60693 |
| u1hs11 | 1.79865 | 5.68329 | 3.15975 | 0.5964 | 0.42765 | 0.60986 |
| cvh8v75 | 1.85783 | 6.65437 | 3.58179 | 0.63215 | 0.46459 | 0.65006 |
| cvh8v45 | 1.85783 | 6.65437 | 3.58179 | 0.63414 | 0.47428 | 0.65803 |
| cvh8v55 | 1.85783 | 6.65437 | 3.58179 | 0.63897 | 0.47059 | 0.65501 |
| h8d40t75 | 1.85783 | 6.65437 | 3.58179 | 0.63756 | 0.4674 | 0.65239 |
| cvh8v35 | 1.85783 | 6.65437 | 3.58179 | 0.64563 | 0.47865 | 0.6616 |
| d40whsC10 | 1.87177 | 6.02158 | 3.21706 | 0.64049 | 0.47751 | 0.65882 |
| n40w6hs10 | 1.89185 | 6.01628 | 3.1801 | 0.64203 | 0.47774 | 0.65927 |
| cth8t55 | 1.89762 | 6.76582 | 3.56543 | 0.63066 | 0.49836 | 0.67089 |
| t67hs10 | 1.90142 | 5.54798 | 2.91781 | 0.6444 | 0.49965 | 0.67342 |
| h7d60t65 | 1.91233 | 5.68329 | 2.97192 | 0.64161 | 0.50222 | 0.67521 |
| v45hs10 | 1.97852 | 5.68329 | 2.87249 | 0.6601 | 0.52129 | 0.68969 |
| v55hs10 | 1.97852 | 5.68329 | 2.87249 | 0.64001 | 0.51819 | 0.68713 |
| u8hs10 | 1.97852 | 5.68329 | 2.87249 | 0.6601 | 0.52129 | 0.68969 |
| v75hs10 | 1.97852 | 5.68329 | 2.87249 | 0.65096 | 0.51331 | 0.68309 |
| v25hs10 | 1.97852 | 5.68329 | 2.87249 | 0.65671 | 0.53008 | 0.69695 |
| v65hs10 | 1.97852 | 5.68329 | 2.87249 | 0.65025 | 0.51557 | 0.68496 |
| u6hs10 | 1.97852 | 5.68329 | 2.87249 | 0.63604 | 0.51074 | 0.67672 |
| as5hs10 | 1.97852 | 5.68329 | 2.87249 | 0.00057 | 0.00055 | 0.00078 |
| u7hs10 | 1.97852 | 5.68329 | 2.87249 | 0.6361 | 0.51075 | 0.67671 |
| as10hs10 | 1.97852 | 5.68329 | 2.87249 | 0.19192 | 0.12997 | 0.26281 |
| u1hs10 | 1.97852 | 5.68329 | 2.8725 | 0.61501 | 0.49551 | 0.65846 |
| u2hs10 | 1.97852 | 5.68329 | 2.8725 | 0.62493 | 0.535 | 0.71748 |
| u5hs10 | 1.97852 | 5.68329 | 2.8725 | 0.64479 | 0.51425 | 0.68539 |

| Model run | W/h* | W [km] | h* [km] | Coupling coeff. $\chi$ | $\chi$ lower bound | $\chi$ upper bound |
|---|---|---|---|---|---|---|
| v35hs10 | 1.97852 | 5.68329 | 2.87249 | 0.66281 | 0.52511 | 0.69285 |
| t65hs10 | 1.97852 | 5.68329 | 2.87249 | 0.6601 | 0.52129 | 0.68969 |
| as500_01 | 1.97852 | 5.68329 | 2.87249 | 0.66755 | 0.66755 | 0.77058 |
| Aas500 | 1.97852 | 5.68329 | 2.87249 | 0.68373 | 0.65058 | 0.74443 |
| d50whsC10 | 2.03127 | 6.02159 | 2.96444 | 0.66062 | 0.52236 | 0.69078 |
| n50whsC10 | 2.03128 | 6.02159 | 2.96444 | 0.66062 | 0.52236 | 0.69078 |
| cth8t50 | 2.05187 | 7.37475 | 3.59415 | 0.65304 | 0.52697 | 0.6955 |
| h8d35t75 | 2.08201 | 7.45732 | 3.58179 | 0.67164 | 0.53746 | 0.70401 |
| ht8t55 | 2.09924 | 6.76582 | 3.22299 | 0.65542 | 0.52989 | 0.69632 |
| d60whsC10 | 2.12099 | 6.02158 | 2.83904 | 0.66527 | 0.53801 | 0.70301 |
| d60w6hs10 | 2.12099 | 6.02158 | 2.83904 | 0.66527 | 0.53801 | 0.70301 |
| g1t75 | 2.13624 | 6.90114 | 3.23051 | 0.6922 | 0.56281 | 0.72332 |
| g2hs12 | 2.14363 | 7.91601 | 3.69281 | 0.68007 | 0.56276 | 0.72344 |
| d70whsC10 | 2.16999 | 6.0216 | 2.77494 | 0.67418 | 0.54429 | 0.70693 |
| sn34hs10 | 2.17313 | 5.68329 | 2.61526 | 0.64679 | 0.51826 | 0.6848 |
| n70w6hs10 | 2.20343 | 6.04835 | 2.74497 | 0.67454 | 0.54459 | 0.70722 |
| u4hs12 | 2.29075 | 7.37475 | 3.21935 | 0.65396 | 0.52909 | 0.69271 |
| cth8t45 | 2.29277 | 8.2543 | 3.60015 | 0.65863 | 0.54125 | 0.70762 |
| h8d30t75 | 2.38839 | 8.55469 | 3.58179 | 0.68676 | 0.5661 | 0.72645 |
| d70w6hs10 | 2.39086 | 6.04835 | 2.52978 | 0.68477 | 0.5516 | 0.71486 |
| u3hs8 | 2.47315 | 5.68329 | 2.298 | 0.70168 | 0.57957 | 0.73729 |
| u1hs8 | 2.47315 | 5.68329 | 2.298 | 0.71161 | 0.58358 | 0.74035 |
| d40t55hs10 | 2.48217 | 9.11557 | 3.67242 | 0.68652 | 0.56075 | 0.72259 |
| t55hs10 | 2.48217 | 6.76582 | 2.72577 | 0.66938 | 0.553 | 0.71486 |
| g1t65 | 2.57236 | 7.91601 | 3.07734 | 0.69718 | 0.58335 | 0.73904 |
| h7d40t65 | 2.57648 | 7.65708 | 2.97192 | 0.69018 | 0.55723 | 0.72078 |
| ht8t45 | 2.63668 | 8.2543 | 3.13056 | 0.66654 | 0.55685 | 0.71918 |
| u4hs10 | 2.74891 | 7.37475 | 2.68279 | 0.68434 | 0.57109 | 0.72737 |
| u4hs9 | 3.05434 | 7.37475 | 2.41451 | 0.71066 | 0.60051 | 0.75157 |
| t45hs10 | 3.11765 | 8.2543 | 2.6476 | 0.68208 | 0.56572 | 0.72542 |
| g1t55 | 3.16395 | 9.40449 | 2.97239 | 0.68738 | 0.58956 | 0.73688 |
| u1hs6 | 3.29753 | 5.68329 | 1.7235 | 0.79195 | 0.66482 | 0.79895 |
| g1t45 | 3.94445 | 11.5019 | 2.91597 | 0.76301 | 0.65805 | 0.79054 |
| g2hs6 | 4.28726 | 7.91601 | 1.8464 | 0.80529 | 0.73056 | 0.84129 |
| u4hs6 | 4.58151 | 7.37475 | 1.60968 | 0.80864 | 0.72638 | 0.83997 |
| u1hs4 | 4.9463 | 5.68329 | 1.149 | 0.87398 | 0.84362 | 0.90734 |
| g2hs4 | 6.43089 | 7.91601 | 1.23094 | 0.9103 | 0.89237 | 0.93315 |
| u4hs4 | 6.87226 | 7.37475 | 1.07312 | 0.90174 | 0.87593 | 0.92452 |

**Table 4-2, continued**

| Model run | Dip [°] | Along-strike fault length [km] | Plate rate [mm/yr] | Thermal gradient [°C/km] |
|---|---|---|---|---|
| d30w6hs10 | 30 | 25 | 45 | 107.01754 |
| u3hs20 | 60 | 25 | 65 | 65 |
| u2hs20 | 60 | 50 | 65 | 65 |
| u8hs18 | 60 | 25 | 45 | 65 |
| u3hs16 | 60 | 25 | 65 | 65 |
| h8d70t75 | 70 | 25 | 65 | 75 |
| u1hs15 | 60 | 25 | 45 | 65 |
| h8d60t75 | 60 | 25 | 65 | 75 |
| d25whsC10 | 25 | 25 | 45 | 126.61254 |
| d40w6hs10 | 40 | 25 | 45 | 83.24487 |
| u1hs14 | 60 | 25 | 45 | 65 |
| u10hs10 | 60 | 25 | 45 | 82 |
| t80hs10 | 60 | 25 | 45 | 80 |
| u3hs13 | 60 | 25 | 65 | 65 |
| h8d50t75 | 50 | 25 | 65 | 75 |
| cth8t65 | 60 | 25 | 65 | 65 |
| d30whsC10 | 30 | 25 | 45 | 107.01754 |
| g2hs16 | 60 | 25 | 55 | 65 |
| d45w6hs10 | 45 | 25 | 45 | 75.67283 |
| d30hs10 | 30 | 25 | 45 | 75 |
| d60hs10 | 60 | 25 | 45 | 75 |
| u9hs10 | 60 | 25 | 45 | 75 |
| d48hs10 | 48 | 25 | 45 | 75 |
| d40hs10 | 40 | 25 | 45 | 75 |
| d70hs10 | 70 | 25 | 45 | 75 |
| d50hs10 | 50 | 25 | 45 | 75 |
| t75hs10 | 60 | 25 | 45 | 75 |
| u1hs12 | 60 | 25 | 45 | 65 |
| ht8t65 | 60 | 25 | 65 | 65 |
| cth8t60 | 60 | 25 | 65 | 60 |
| h8d44t75 | 44 | 25 | 65 | 75 |
| u3hs115 | 60 | 25 | 65 | 65 |
| u1hs115 | 60 | 25 | 45 | 65 |
| d48w6hs10 | 48 | 25 | 45 | 72.00315 |
| t72hs10 | 60 | 25 | 45 | 72 |
| u8hs1135 | 60 | 25 | 45 | 65 |
| cth8t59 | 60 | 25 | 65 | 59 |
| u8hs113 | 60 | 25 | 45 | 65 |

| Model run | Dip [°] | Along-strike fault length [km] | Plate rate [mm/yr] | Thermal gradient [°C/km] |
|---|---|---|---|---|
| h8d43t75 | 43 | 25 | 65 | 75 |
| d35whsC10 | 35 | 25 | 45 | 93.2897 |
| d49w6hs10 | 49 | 25 | 45 | 70.89982 |
| t71hs10 | 60 | 25 | 45 | 71 |
| u2hs1125 | 60 | 50 | 45 | 65 |
| h7d70t65 | 70 | 25 | 65 | 65 |
| u8hs112 | 60 | 25 | 45 | 65 |
| d50w6hs10 | 50 | 25 | 45 | 69.85074 |
| t70hs10 | 60 | 25 | 45 | 70 |
| h8d42t75 | 42 | 25 | 65 | 75 |
| g1t85 | 60 | 25 | 55 | 85 |
| cth8t58 | 60 | 25 | 65 | 58 |
| u1hs11 | 60 | 25 | 45 | 65 |
| cvh8v75 | 40 | 25 | 75 | 75 |
| cvh8v45 | 40 | 25 | 45 | 75 |
| cvh8v55 | 40 | 25 | 55 | 75 |
| h8d40t75 | 40 | 25 | 65 | 75 |
| cvh8v35 | 40 | 25 | 35 | 75 |
| d40whsC10 | 40 | 25 | 45 | 83.24487 |
| n40w6hs10 | 40 | 25 | 45 | 83.24487 |
| cth8t55 | 60 | 25 | 65 | 55 |
| t67hs10 | 60 | 25 | 45 | 67 |
| h7d60t65 | 60 | 25 | 65 | 65 |
| v45hs10 | 60 | 25 | 45 | 65 |
| v55hs10 | 60 | 25 | 55 | 65 |
| u8hs10 | 60 | 25 | 45 | 65 |
| v75hs10 | 60 | 25 | 75 | 65 |
| v25hs10 | 60 | 25 | 25 | 65 |
| v65hs10 | 60 | 25 | 65 | 65 |
| u6hs10 | 60 | 25 | 45 | 65 |
| as5hs10 | 60 | 5 | 45 | 65 |
| u7hs10 | 60 | 25 | 45 | 65 |
| as10hs10 | 60 | 10 | 45 | 65 |
| u1hs10 | 60 | 25 | 45 | 65 |
| u2hs10 | 60 | 50 | 45 | 65 |
| u5hs10 | 60 | 25 | 45 | 65 |
| v35hs10 | 60 | 25 | 35 | 65 |
| t65hs10 | 60 | 25 | 45 | 65 |
| as500_01 | 60 | 400 | 55 | 65 |
| Aas500 | 60 | 500 | 60 | 65 |
| d50whsC10 | 50 | 25 | 45 | 69.85074 |
| n50whsC10 | 50 | 25 | 45 | 69.85074 |

| Model run | Dip [°] | Along-strike fault length [km] | Plate rate [mm/yr] | Thermal gradient [°C/km] |
|---|---|---|---|---|
| cth8t50 | 60 | 25 | 65 | 50 |
| h8d35t75 | 35 | 25 | 65 | 75 |
| ht8t55 | 60 | 25 | 65 | 55 |
| d60whsC10 | 60 | 25 | 45 | 61.78661 |
| d60w6hs10 | 60 | 25 | 45 | 61.78661 |
| g1t75 | 60 | 25 | 55 | 75 |
| g2hs12 | 60 | 25 | 55 | 65 |
| d70whsC10 | 70 | 25 | 45 | 56.94285 |
| sn34hs10 | 60 | 25 | 45 | 65 |
| n70w6hs10 | 70 | 25 | 45 | 56.94285 |
| u4hs12 | 60 | 25 | 45 | 50 |
| cth8t45 | 60 | 25 | 65 | 45 |
| h8d30t75 | 30 | 25 | 65 | 75 |
| d70w6hs10 | 70 | 25 | 45 | 56.94285 |
| u3hs8 | 60 | 25 | 65 | 65 |
| u1hs8 | 60 | 25 | 45 | 65 |
| d40t55hs10 | 40 | 25 | 45 | 55 |
| t55hs10 | 60 | 25 | 45 | 55 |
| g1t65 | 60 | 25 | 55 | 65 |
| h7d40t65 | 40 | 25 | 65 | 65 |
| ht8t45 | 60 | 25 | 65 | 45 |
| u4hs10 | 60 | 25 | 45 | 50 |
| u4hs9 | 60 | 25 | 45 | 50 |
| t45hs10 | 60 | 25 | 45 | 45 |
| g1t55 | 60 | 25 | 55 | 55 |
| u1hs6 | 60 | 25 | 45 | 65 |
| g1t45 | 60 | 25 | 55 | 45 |
| g2hs6 | 60 | 25 | 55 | 65 |
| u4hs6 | 60 | 25 | 45 | 50 |
| u1hs4 | 60 | 25 | 45 | 65 |
| g2hs4 | 60 | 25 | 55 | 65 |
| u4hs4 | 60 | 25 | 45 | 50 |

## 4.A Comparison to continental settings

### 4.A.1 Estimating seismic coupling in the Corinth rift

We use earthquake catalog data to estimate the seismic coupling coefficient for the Corinth rift. The Corinth rift is an actively rifting half-graben separating the Peloponnese from continental Greece, and it is currently opening at 10–14 mm/yr according to geodetic studies (Briole et al., 2000; Moretti et al., 2003). We first calculate moment release rates from earthquake catalog data by summing the moment released by earthquakes between 1964 and 2008, and dividing by the elapsed time. Since earthquakes occur throughout central Greece, this estimate is dependent on how rift-related seismicity is separated from more diffuse seismicity. We define a rectangular region around the main part of the Corinth rift (Figure 4-A1), and obtain 25 estimates of moment release rate by shifting the boundaries of this region and summing the moments of the events occurring within the boundaries. We found that using a slightly smaller or larger rectangular area to select earthquakes did not have a large effect on the calculated moment release rate. This is because moment release is dominated by the largest events in the catalog, and the largest events in the Corinth rift occur in areas that are clearly within the actively rifting section (Figure 4-A1). The calculated coupling coefficient is related to the moment release rate by

$$\chi = \frac{\dot{M}_0 \sin \varphi}{V_{pl} \mu H (1 - M)} \tag{1}$$

where $\dot{M}_0$ is the moment released per unit time and unit length of rift, $H$ is the thickness of the seismogenic layer, $V_{pl}$ is the "plate" velocity or forcing velocity, $\mu$ is the shear modulus, $\varphi$ is the fault dip angle, and $M$ is the fraction of the plate separation rate accommodated magmatically (i.e., not by fault slip) (Buck et al., 2005; Olive & Escartín, 2016). To propagate the uncertainties in fault dip and seismogenic layer thickness into our estimates of seismic coupling, we parameterized $\varphi$ and $H$ with probability density functions and drew 1000 random values for each parameter within ranges defined by field and seismic studies in the Gulf of Corinth. We then calculated the coupling coefficient (Equation (1)) with each possible combination of fault dip, seismogenic layer thickness, and our 25 estimates of moment release rate to obtain $2.5 \times 10^7$ estimates of coupling.

The structure and level of activity of major faults in the Corinth rift remains a subject of debate. Previous studies have found evidence for normal faulting both at low angles and with dips closer to 60º (Armijo et al., 1996; Beckers et al., 2015; Bernard et al., 1997; Clément et al., 2004; Lambotte et al., 2014; Micarelli et al., 2003; Rigo et al., 1996). Thus, we drew dip values from a normal distribution with a mean of 50° (Bell et al., 2009), and a standard deviation of 3°. This choice skews toward the steeper-dipping faults observed in the eastern part of the rift, consistent with studies suggesting that the newer (and steeper) faults in the Aigion area are representative of the current stage of rifting (e.g., Moretti et al., 2003).

The distribution of seismicity in the region suggests that the thickness of the seismogenic layer is at least 10 km and may be greater than 20 km (Lambotte et al., 2014; Makropoulos et al., 2012; Taylor et al., 2011). Values for the seismogenic layer thickness (in km) were drawn from a lognormal distribution with a location parameter $\mu = 1.7$ and scale parameter $\sigma = 0.4$ added to a base value of 10 km. This distribution is close to zero for layer thicknesses $< 10$ km, peaks near a thickness of 15 km, and tapers off gradually, returning to near zero for thicknesses $> 25$ km. This assumption effectively confines seismicity to the crust, as the Moho is estimated to lie at ~30 km beneath the Gulf of Corinth (Chouliaras et al., 1997; Zelt et al., 2005).

An extensive earthquake catalog has been compiled for Central Greece, complete to at least $M_L = 4.5$ since 1964 (Makropoulos et al., 2012). We used a conversion from local to moment magnitudes calibrated for the region from Papazachos et al. (1997):

$$M_W = 0.97M_L + 0.58 \quad (2)$$

and then calculated the seismic moment in Nm from the moment magnitudes:

$$M_0 = 10^{1.5*(M_W+6.033)} \quad (3)$$

The magnitude of completeness for the catalog was estimated to be $M_L = 3.7$ using the goodness-of-fit method of Wiemer and Wyss (2000). We then summed the moment release for events with magnitudes greater than the magnitude of completeness and estimated the coupling coefficient. Some studies have found local magnitudes to be equivalent to moment magnitudes for $M_L > 3$ (e.g.,

Deichmann, 2006, 2017; Hanks & Boore, 1984). Because the magnitude of completeness for the local magnitudes was greater than 3, we also tried estimating the coupling coefficient assuming $M_L = M_W$. Finally, the ISC catalog includes the Central Greece catalog, with moment magnitudes given for a few large events. We estimated the coupling coefficient a third time based on the ISC catalog (International Seismological Centre, 2017). If moment magnitudes were not available in the ISC catalog, local magnitudes were converted using Equation (2); if local magnitudes were also not available, body wave magnitudes $m_b$ were used with the regional conversion of Papazachos et al. (1997):

$$M_W = 1.28 * m_b - 1.12 \quad (4)$$

For the Central Greece catalog with the $M_L$ to $M_W$ magnitude conversion and an opening rate of 13 mm/yr, we estimate a seismic coupling coefficient of $\chi = 3.24 \pm 0.49$. Taking $M_L = M_W$ without the magnitude conversion, we find $\chi = 0.84 \pm 0.13$. Finally, with the ISC catalog and conversions where $M_W$ is not directly available, $\chi = 1.65 \pm 0.25$ (Figure 4-A2). In theory, the coupling coefficient should be between 0 and 1, but values greater than 1 can be observed when the time length of the catalog is short relative to the recurrence interval of large events. Specifically, when the coupling coefficient is converging to a value near 1, it stays above 1 for portions of the first few seismic cycles (Figure 4-A3). We also observed this in our numerical models, in cases where the coupling coefficient started very large and dropped to a stable value once enough slip had accumulated that a large event had only a small effect on the ratio of seismic to total slip (Figure 4-A3c). Because we used catalogs for Corinth starting at 1964 to ensure that the completion magnitude was sufficiently low, we only had three large events to analyze, implying that $\chi > 1$ may be due to the brevity of the catalog.

The estimates of seismogenic layer thickness and fault dip also impact the calculated seismic coupling coefficient $\chi$. Figure 4-A3 shows how different estimates of seismogenic layer thickness influence the calculated coupling coefficient for the Corinth rift. We know the seismic moment release from the catalog data, and calculate the coupling coefficient by estimating the total moment release rate (seismic and aseismic) for the fault. If we assume a large seismogenic layer thickness, the total moment release rate over the seismogenic zone will be higher than the seismic moment release

rate, and the coupling coefficient will be less than 1, implying more aseismic slip. Alternatively, if we assume a smaller seismogenic layer thickness, the total moment release rate is less than what is being released by earthquakes and coupling is greater than 1. If the seismogenic layer thickness is such that the total moment release rate matches the average seismic moment release rate, the coupling coefficient will oscillate as successive earthquakes occur, converging toward 1. A similar calculation can be done to show how the assumptions for the fault dip influence the coupling coefficient. We have accounted for these effects by propagating the uncertainties in seismogenic layer thickness and fault dip through to the uncertainty in $\chi$ in the probability distributions shown in Figure 4-A2.

### 4.A.2 Figures

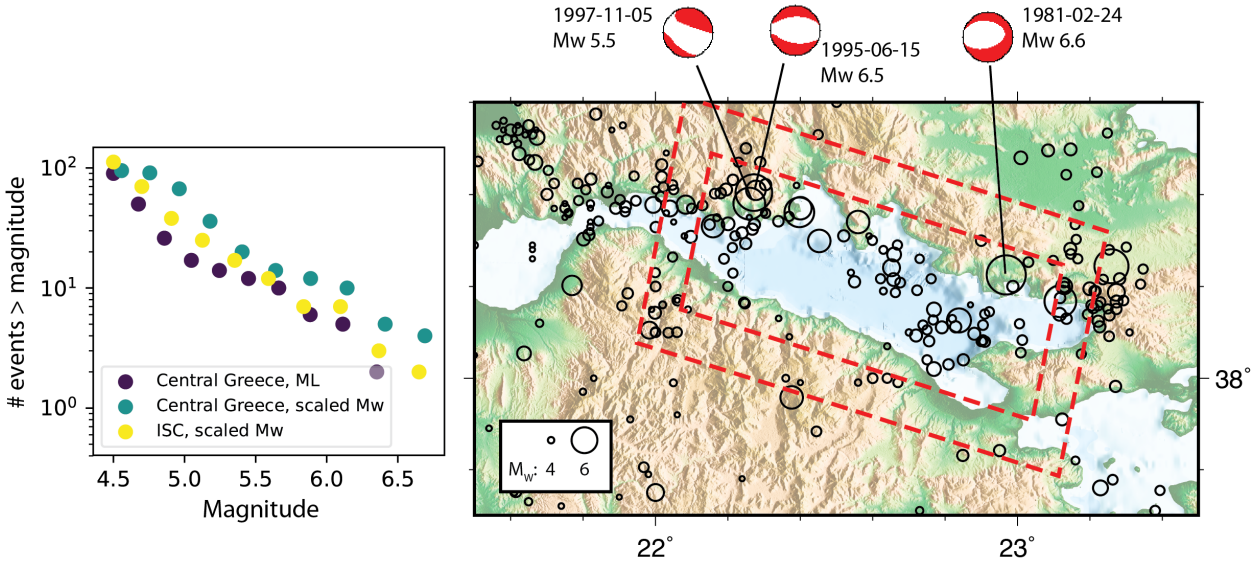


**Figure 4A-1.** Seismicity in the Gulf of Corinth (right). Earthquakes from 1964-2008 from the local catalog (Makropoulos et al., 2012) are shown by black circles, with the circle size scaled by earthquake magnitude. Focal mechanisms from the Harvard CMT catalog are shown for some of the largest events. Red dashed lines outline the largest and smallest rectangular regions used to select events from the catalog. Map topography is from GMRT v3.4. The magnitude distribution of the local catalog, moment-scaled local catalog and ISC catalog for events within the larger red box are plotted to the left.

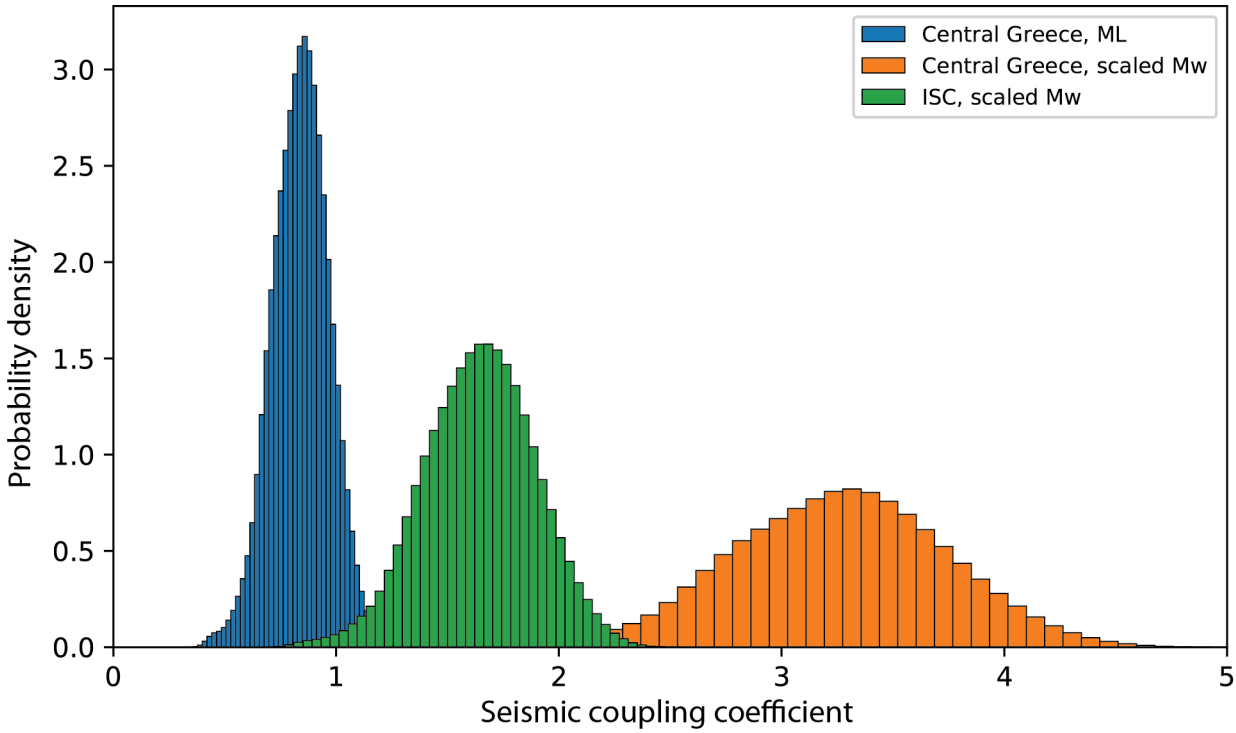


**Figure 4A-2.** Probability distributions of the coupling coefficient for the Corinth rift calculated with $M_L$ from the Central Greece catalog (Makropoulos et al., 2012) (blue), $M_L$ from the Central Greece catalog scaled to $M_W$ using a regional correlation (Papazachos et al., 1997) (orange), and magnitudes scaled to $M_W$ pulled from the global ISC catalog (International Seismological Centre, 2017) (green).

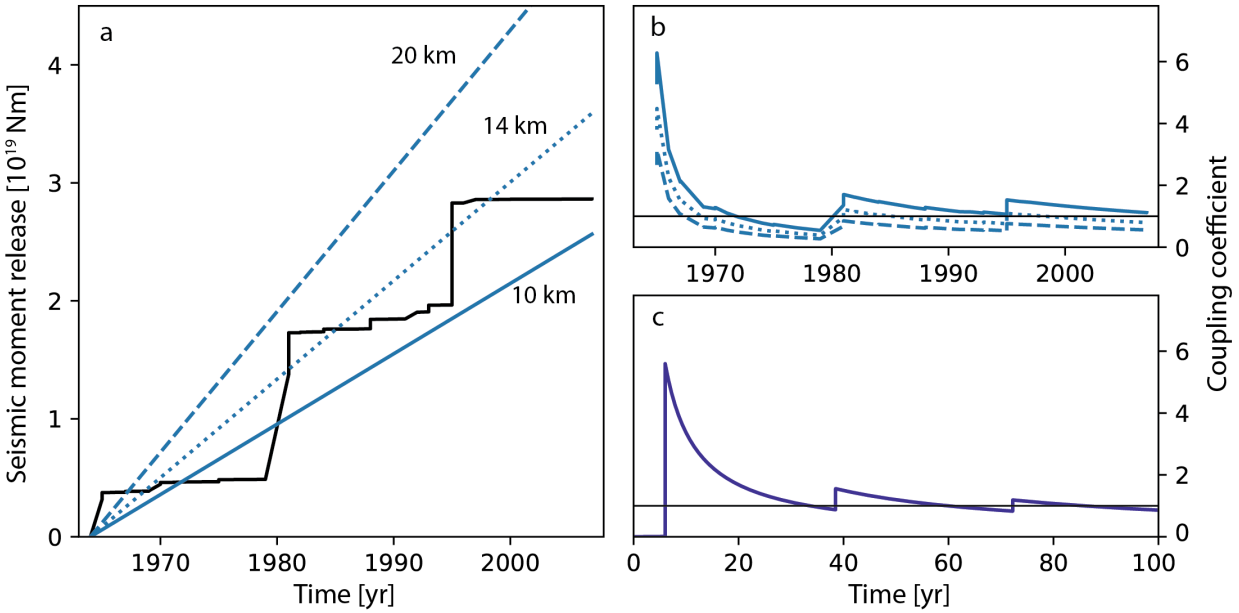


**Figure 4A-3. (a)** Cumulative seismic moment release in the Gulf of Corinth (black line) with three different estimates of the total (seismic + aseismic) moment release calculated using a seismogenic layer thickness of 10, 14, and 20 km and a fault dip of 50°. **(b)** Seismic coupling coefficient through time based on the observations and the three prediction scenarios shown in (a). **(c)** Seismic coupling coefficient through time for model run *u4hs4* (Table 4-2). In the model run, as for the observations, the coupling coefficient can be greater than 1 for several seismic cycles or parts of seismic cycles depending on where in the seismic cycle we start the summation of cumulative moment.

# Appendix

# Future directions for modeling the development of seismic anisotropy in the oceanic upper mantle

## A.1 Abstract

Laboratory experiments have shown that deformation of mantle minerals such as olivine can produce mineral fabrics. These experimental results imply that macroscopic seismic anisotropy resulting from mineral alignment can be used as a proxy for mantle flow. Observations of regional variations in mantle anisotropy invite interpretation in terms of dynamic flow patterns, but making connections between these observations and particular mantle dynamics requires a quantitative framework linking grain-scale deformation processes to measurable quantities. Numerical models can be used to build such a framework by generating predictions for mineral fabrics and seismic anisotropy under varying assumptions for mantle rheology and flow. Previous modeling studies exploring the effects of particular rheologic parameters and mantle flow regimes near mid-ocean ridges have predicted significant differences in flow patterns and/or anisotropy for variations in factors such as the upwelling style at the ridge or the amount of deep mantle melting occurring below the ridge. These studies have also suggested that the effects of such factors on anisotropy may be different when they are considered in combination rather than being treated as isolated variables. Here, we present preliminary models for the development of mineral fabrics due to mid-ocean ridge corner flow, and we discuss ways that these models could be extended in the future to explore the effects of more complex rheologies, rheologic feedbacks, and dynamic flow in the asthenosphere on the development of mineral fabrics and corresponding seismic observations.

## A.2 Introduction

Laboratory experiments have demonstrated that deformation of mantle minerals such as olivine can produce mineral fabrics under physical conditions expected to be present in parts of the mantle (e.g., Ave'Lallemant, 1975; Skemer & Hansen, 2016; Zhang et al., 2000; Zhang & Karato, 1995). Observations of macroscopic seismic anisotropy in the mantle are therefore often attributed to the large-scale alignment of the mineral olivine by shear deformation due to flow (e.g., D. L. Anderson, 1987; Auer et al., 2015; Ekstrom & Dziewonski, 1998; Fuchs, 1977; Gaherty et al., 2004; Maggi et al., 2006; McKenzie, 1979; Morris et al., 1969; Raitt et al., 1971). Measurements of seismic anisotropy in the upper mantle broadly agree with predicted directions for large-scale mantle flow (e.g., Becker et al., 2003, 2014; Behn et al., 2004; Conrad et al., 2007), suggesting that laboratory results can be usefully extrapolated to tectonic scales.

Observations of regional variations in seismic anisotropy near mid-ocean ridges have invited interpretation in terms of dynamic variation in mantle flow and plate formation processes (Dunn & Toomey, 1997; Toomey et al., 2007; VanderBeek et al., 2016), and models for mantle flow and consequent mineral fabric development due to plate spreading predict observable variations in seismic anisotropy associated with dynamic flow (e.g., Blackman & Kendall, 2002; Conder, 2007; Toomey et al., 2002). However, these models have mainly focused on the near-axis region, and have not addressed whether seismic anisotropy can be used to make inferences about processes that influence anisotropy as the plate moves off axis. For example, observations of low-anisotropy channels in the asthenosphere coincident with the seismic low velocity zone have prompted hypotheses that channeled flow at the base of the lithosphere or secondary convection lead to weak or quasi-vertical fabric within a narrow depth range (e.g., Lin et al., 2016; Montagner, 2002), but we lack quantitative predictions for anisotropy due to secondary convection or channel flow to compare to the observations.

Testing hypotheses for mantle flow patterns requires a quantitative framework linking deformation to seismic observations. Numerical models can be used to build such a framework by predicting seismic anisotropy under different mantle flow regimes. Models for anisotropy consist of two components, a model for mantle flow and a model for texture development due to deformation. These components can each be parameterized with varying levels of complexity in how they treat

rheology, and can also be coupled to varying degrees in order to incorporate rheologic feedbacks associated with fabric development.

Previous modeling studies have shown that mantle flow predictions vary significantly depending on how mantle rheology is parameterized (Braun et al., 2000; Podolefsky et al., 2004; A. J. Turner et al., 2015). These previous studies looking at rheologic factors in isolation or in limited combination have also suggested that rheologic feedbacks are potentially significant for the development of anisotropy (e.g., Blackman et al., 2017), indicating that model parameterizations that simultaneously incorporate multiple factors such as melting, dehydration, and viscous anisotropy in a composite rheology may be useful for interpreting observations from the mantle. Further, there are other rheologic factors that are predicted to influence mantle flow patterns, such as grain size evolution, that have not yet been used in models to predict anisotropy.

The combination of geophysical measurements made at the NoMelt site in the central Pacific offers a uniquely detailed point of comparison for regional geodynamic modeling to tease apart the flow patterns and physical factors that shape the anisotropic structure of the upper mantle. Observations from NoMelt constrain shear velocity, conductivity, attenuation, and azimuthal anisotropy through the asthenosphere, and receiver functions show evidence for the presence of the G discontinuity beneath the NoMelt array (Lin et al., 2016; Ma et al., 2018; Matsuno & Evans, 2017; Russell et al., 2019; Sarafian et al., 2015). The plate at the NoMelt site has a simple tectonic history, making it a useful basis for comparison to regions where more complex tectonics have influenced upper mantle structure.

In this appendix, I describe previous work done to model mantle flow and anisotropy using different rheologic parameterizations, and I present preliminary models for mantle flow and texture development. I also discuss future directions for modeling efforts to complement the multifaceted geophysical observations from NoMelt.

### A.3 Previous approaches to modeling mantle flow and fabric development

Models for the development of mineral fabrics in the Earth have two components: (1) a calculation of the mantle flow field, and (2) a calculation of fabric based on the flow and a model for how the

mantle responds to deformation. The resulting fabric prediction can then be translated into predictions for seismic observations. Previous studies have approached these two calculations in a variety of ways, each with particular advantages and disadvantages.

Early mantle flow models used to study anisotropy employed analytical treatments to model 2D mantle flow beneath mid-ocean ridges. For example, Ribe (1992) calculated mantle flow assuming a power law rheology, where shear stress is proportional to the deformation gradient raised to a power. Further studies improved upon these efforts by implementing temperature-dependent viscosity and parameterizing some effects of melting and melt extraction in finite element models (Blackman et al., 1996, 2002; Blackman & Kendall, 2002). Studies have also tested models that include composite rheology and deep damp mantle melting (Braun et al., 2000), anisotropic viscosity (Blackman et al., 2017), and grain size evolution (A. J. Turner et al., 2015, 2017). The flow fields predicted by these different models are broadly similar; slight variations in flow mainly appear near the ridge axis, associated with buoyancy-driven or passive upwelling, and in the shallow mantle off-axis due to differences in the viscosity structure predicted for different rheologies (e.g., Blackman & Kendall, 2002; Braun et al., 2000).

Texture development has been modeled using finite strain, kinematic constraint, stress equilibrium, and visco-plastic self-consistent (VPSC) methods. Finite strain calculations predict the orientations of crystallographic axes based solely on the time-integrated strain that crystals experience (e.g., Ribe, 1992). Kinematic constraint, or upper bound, models enforce homogeneous strain throughout a polycrystal. In theory, this requires five independent slip systems, which olivine does not have, but models have been developed which effectively use fewer slip systems (e.g., Ribe & Yu, 1991). Stress equilibrium methods, also known as lower bound models, require all grains to be under equal stress and parameterize texture development by intracrystalline slip using prescribed hardnesses of different slip systems in a polycrystal (e.g., Chastel et al., 1993). These have the advantage of not requiring five independent slip systems to begin with. VPSC models can be tuned to emphasize stress equilibrium and strain compatibility to varying degrees, and they consider interaction between individual grains and their surroundings in the form of a homogeneous equivalent medium (e.g., Molinari et al., 1987; Tommasi et al., 2000).

Recently, kinematic models such as the D-Rex model have been developed that include parameterizations of dynamic recrystallization and grain boundary sliding, neither of which is considered in previous texturing models (Kaminski et al., 2004; Kaminski & Ribe, 2001). These models predict lattice preferred orientations for aggregates using dislocation densities calculated from local stresses. Their predictions for texture are dependent on non-dimensional model parameters that govern grain boundary mobility, subgrain nucleation, and grain boundary sliding. These parameters have been calibrated to reproduce olivine textures observed in laboratory experiments (Kaminski et al., 2004; Lev & Hager, 2008; Zhang et al., 2000; Zhang & Karato, 1995). Similar models have been developed and calibrated to predict mechanical anisotropy as well as mineral texture for large strains (Hansen, Conrad, et al., 2016).

Combined models for mantle flow and mineral textures have predicted observable differences in anisotropy for different flow regimes (Blackman et al., 2017; Blackman & Kendall, 2002). Finite strain calculations suggest that factors such as melting should also have significant effects on mineral fabrics and anisotropy (Braun et al., 2000). Interestingly, models that incorporate feedbacks between mineral fabrics and mantle flow through anisotropic viscosity do not show large differences in mantle flow compared to models with isotropic viscosity, but do suggest that melt distribution is influenced by anisotropic viscosity (Blackman et al., 2017).

Other factors that are predicted to significantly influence mantle flow patterns have not yet been included in models to predict seismic anisotropy. For example, grain size is known to influence mantle viscosity and permeability, and is expected to have an effect on mantle flow patterns and seismic observations (Behn et al., 2009; Dannberg et al., 2017; Faul & Jackson, 2005; A. J. Turner et al., 2015). Models for mineral fabrics have also tended to focus on the effects of flow at mid-ocean ridges, leaving the effects of deformation further off-axis largely unexplored.

### A.4 Preliminary models

We have run preliminary models for mantle flow and associated mineral fabric development for a simple corner flow scenario. The flow model was set up as a 2D rectangular domain, 2400 km wide by 200 km deep, representing a cross-section of half of a symmetric spreading ridge. The open-source finite element code ASPECT was used to calculate the flow field (Bangerth et al., 2019;

Heister et al., 2017; Kronbichler et al., 2012). Flow within the domain was driven by the velocity boundary conditions, which were specified on all four boundaries to match the analytical solution for corner flow driven by a horizontal surface plate velocity of 5 cm/yr. On the top boundary, the driving velocity was increased from zero at the ridge axis to 5 cm/yr at 5 km off-axis. This ramp-up is not part of the analytical solution but was necessary to avoid a singular point at x=0. Initial temperatures in the domain were prescribed based on an adiabatic gradient defined by the ages of the upper and lower boundaries. The temperatures at the top and bottom of the domain were held at 273 K and 1570 K, respectively, and temperatures within the domain evolved along with the flow field. The flow model was run forward in time until the velocity and temperature fields were observed to reach steady state. The model was isoviscous, with a constant viscosity of $1x10^{21}$ Pa s. The flow field in the model, which matches the analytical solution aside from a few cells near the corner where the boundary conditions were modified, is shown in Figure A-1.

The steady-state flow conditions of the model were used to calculate finite strain and mineral fabric along streamlines using the D-Rex model (Kaminski et al., 2004; Kaminski & Ribe, 2001). The grain boundary mobility parameter, M*, was set to 125, the nucleation parameter, $\lambda$*, was set to 5, and the threshold dimensionless volume fraction for grain boundary sliding, $\chi$, set to 0.2 (Kaminski et al., 2004). Grain orientations were calculated for aggregates composed of 70% olivine and 30% enstatite. The major axes of the finite strain ellipses (FSE) calculated using D-Rex rotate toward the shear direction along each streamline (Figure A-2).

The orientations of the crystallographic *a* axes are predicted to follow the FSE major axes fairly closely throughout the model domain, since the *a* axes rotate toward the long axis of the FSE for large strains (Kaminski & Ribe, 2002; Ribe, 1992). D-Rex calculates the orientations of crystallographic axes for grains in an aggregate based on the local velocity gradients along a streamline, and the orientations of the *a* axes at representative points along one streamline are shown by pole figures in Figure A-3. The aggregate starts out with randomly orientated grains, and the *a* axes initially develop two broad peak orientations roughly oriented parallel and orthogonal to the flow direction in the upwelling region. The secondary peak orthogonal to flow fades with continued strain, leaving the *a* axes oriented approximately vertically. As the streamline goes through the corner, the axes rotate counter to the flow direction, eventually leaving the peak *a* axis

orientation subparallel to flow as the aggregate moves away from the ridge. This progression can be visualized throughout the model domain by plotting the peak orientations of the *a* axes along multiple streamlines (Figure A-4). As expected, the *a* axis peak orientations roughly match the FSE major axes throughout the domain.

The grain orientations predicted by D-Rex were used to calculate Voigt-averaged elastic tensors along streamlines based on single-crystal elastic tensors for olivine and enstatite. Predictions for anisotropy were then calculated from the hexagonal components of the elastic tensors obtained by symmetry decomposition (Browaeys & Chevrot, 2004). The predictions for anisotropy show a roughly constant strength in the upper ~100 km of the model at 20 Myr (Figure A-5). The rate of fabric development varies with depth, as strong fabrics are quickly generated and locked in along streamlines that go through the shallow part of the domain while aggregates along streamlines through the deeper parts of the model experience less shear near the axis but continue developing fabric further from the ridge (Figure A-5).

Finite strain, mineral fabrics, and associated seismic anisotropy were also calculated using a modified version of the D-Rex model that included a simple parameterization of a dehydration boundary. Seismic observations have suggested that a dehydration boundary formed by melting at the ridge is present in the oceanic upper mantle and the viscosity contrast associated with a dehydration boundary could have consequences for fabric development and anisotropy. The flow model was not modified for this calculation, although the presence of a dehydration boundary is expected to affect flow patterns as well as deformation mechanisms. The effects of hydrogen saturation were incorporated by changing the critical resolved shear stresses for olivine (Jung & Karato, 2001; Wang et al., 2019). This change was imposed over 20 km, between 70 and 50 km depth (Hirth & Kohlstedt, 1996). The resulting predictions for anisotropy show a local minimum in the strength of anisotropy around 60 km depth (Figure A-5). Including the dehydration boundary also resulted in slightly weaker anisotropy above ~40 km compared to the case with no dehydration boundary (Figure A-5).

### A.5 Future directions

While isoviscous models can provide some insights into basic mantle flow patterns, future models including temperature-dependent viscosity and non-linear composite rheology would better match the expected conditions and behavior of the mantle. Composite rheology models can be implemented using experimentally derived parameters (e.g., Faul & Jackson, 2007; Hirth & Kohlstedt, 2004).

Previous models for anisotropy due to mantle corner flow show that individual factors in rheologic models, such as implementations of melting and viscous anisotropy, affect predictions for anisotropy (e.g., Blackman et al., 2017; Braun et al., 2000), and have also suggested that rheologic feedbacks affecting the generation and transport of melt could influence fabric development. These observations motivate further models using rheologic parameterizations that combine composite rheology with melting and anisotropic viscosity in fully coupled models linking fabric development and mantle flow. Studies showing the effects of variable grain size on melt transport beneath mid-ridges suggest that grain size evolution should also be incorporated into future models (A. J. Turner et al., 2017).

While deformation during plate formation is undeniably important in the formation of mineral fabrics, the effects of continued mantle deformation off-axis remain mostly unexplored. The model including the dehydration boundary shows a decrease in anisotropy at ~60 km depth, but it does not reproduce the low-anisotropy channels observed at ~100 km beneath the Pacific plate (Lin et al., 2016; Montagner, 2002), suggesting that it is missing key parts of the rheology and/or the flow regime in the asthenosphere such as secondary convection (Richter, 1973; Richter & Parsons, 1975) or asthenospheric channel flow (French et al., 2013). Further, the viscosity contrast associated with a dehydration boundary is expected to influence mantle flow and deformation patterns both on- and off-axis, and these effects are not accounted for in our simple implementation of a dehydration boundary as a change in the relative hardness of olivine slip systems.

Another factor for future models to consider is the effect of time-dependent flow on predictions for anisotropy. Models where the forces driving flow change over time could inform our understanding of how mantle mineral fabrics are affected by changes in plate motion directions, such as those

associated with the reorganization of the Pacific plate ~50 Myr ago (e.g., Caress et al., 2012; Lonsdale, 1988; Whittaker et al., 2007). This would require extending models from 2D to 3D.

Finally, an important step in connecting model outputs to observations is to propagate predictions for mineral fabrics into predictions for specific types of seismic observations. The NoMelt experiment provides constraints on shear velocity, azimuthal anisotropy, conductivity, and attenuation through the upper 300 km of the mantle at a single location in the central Pacific (Lin et al., 2016; Ma et al., 2018; Russell et al., 2019; Sarafian et al., 2015), enabling detailed comparisons between observations and predictions for seismic structure.

## A.6 Figures

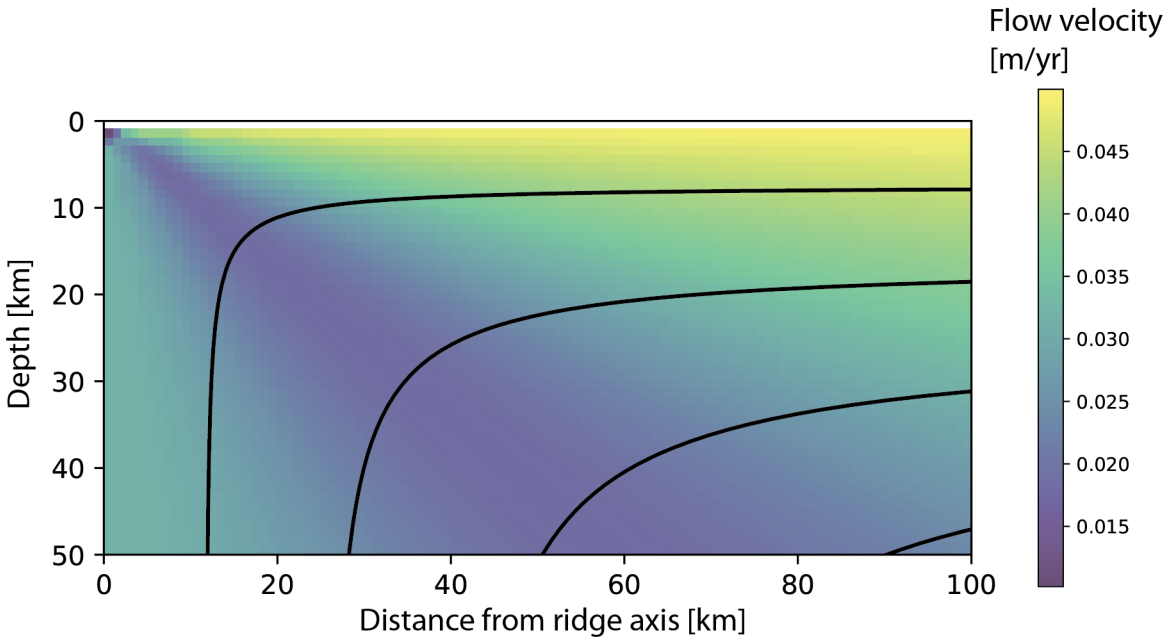


**Figure A-1.** Velocity magnitudes (background colors) and streamlines (black lines) in the flow model.

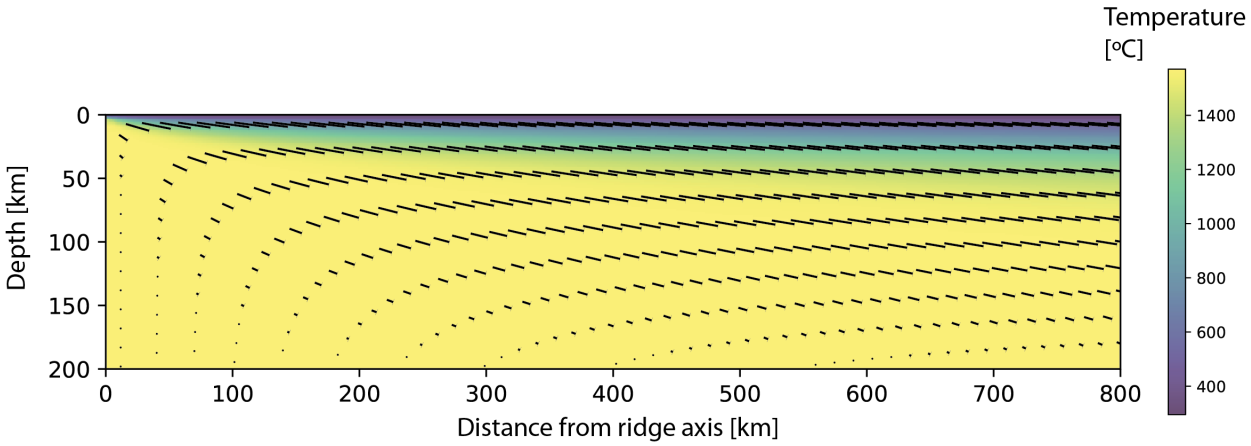


**Figure A-2.** Temperature (background colors) and the major axes of finite strain ellipses (black lines) along streamlines in the flow model.

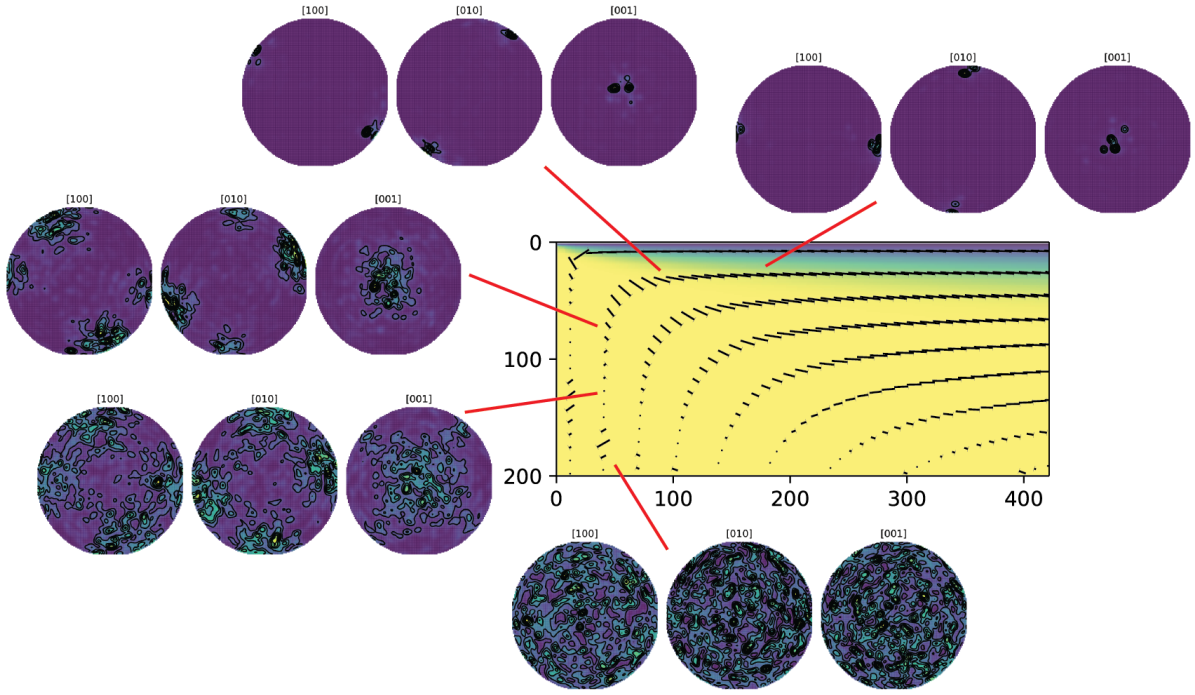


**Figure A-3.** Pole figures for olivine + enstatite aggregates at several points along a streamline in the model. The panel in the center shows part of Figure A-4 for reference.

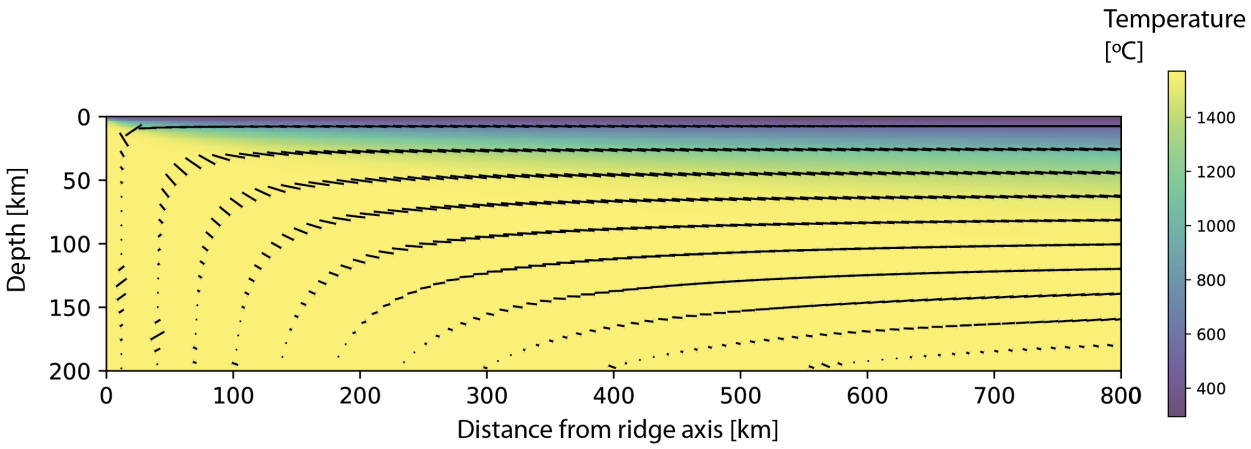


**Figure A-4.** Temperature (background colors) and the peak orientations of olivine *a* axes (black lines) along streamlines within the flow model.

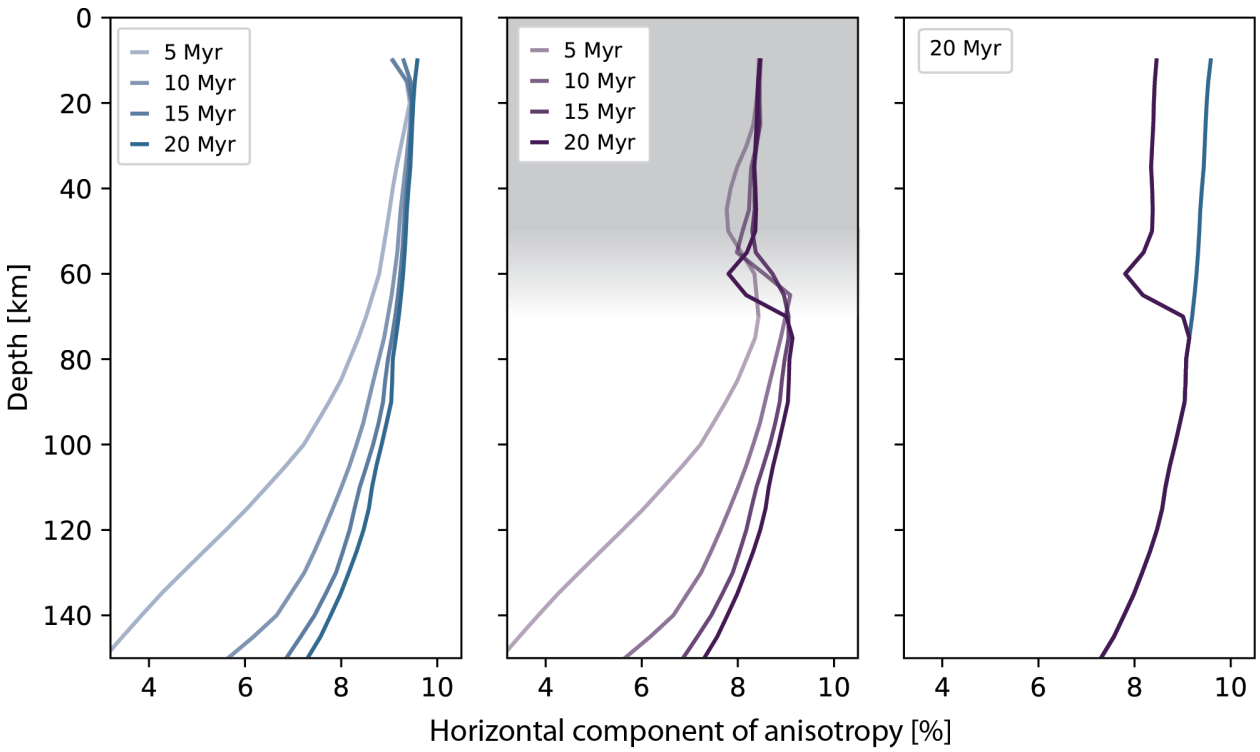


**Figure A-5.** Depth profiles of the horizontal component of anisotropy through time at 5 Myr, 10 Myr, 15 Myr, and 20 Myr, with age indicated by line shading. Profiles are shown for calculations with no dehydration boundary (left) and with a simple dehydration boundary imposed beginning at 70 km depth (center). The transition in critical resolved shear stresses corresponding to the dehydration boundary is indicated by grey background shading. Profiles at 20 Myr for both cases are plotted together on the right.

# References


Anderson, D. L. (1987). Global Mapping of the Uppermantle by Surface Wave Tomography. In K. Fuchs & C. Froidevaux (Eds.), *Composition, Structure and Dynamics of the Lithosphere-Asthenosphere System* (pp. 89–97). American Geophysical Union. https://doi.org/10.1029/GD016p0089

Anderson, D. L., Minster, B., & Cole, D. (1974). The effect of oriented cracks on seismic velocities. *Journal of Geophysical Research*, *79*(26), 4011–4015.

Anderson, O. L., Schreiber, E., Liebermann, R. C., & Soga, N. (1968). Some elastic constant data on minerals relevant to geophysics. *Reviews of Geophysics*, *6*(4), 491–524. https://doi.org/10.1029/RG006i004p00491

Armijo, R., Meyer, B., King, G. C. P., Rigo, A., & Papanastassiou, D. (1996). Quaternary evolution of the Corinth Rift and its implications for the Late Cenozoic evolution of the Aegean. *Geophysical Journal International*, *126*(1), 11–53. https://doi.org/10.1111/j.1365-246X.1996.tb05264.x

Auer, L., Becker, T. W., Boschi, L., & Schmerr, N. (2015). Thermal structure, radial anisotropy, and dynamics of oceanic boundary layers. *Geophysical Research Letters*, *42*(22), 9740–9749. https://doi.org/10.1002/2015GL066246

Ave'Lallemant, H. G. (1975). Mechanisms of preferred orientations of olivine in tectonite peridotite. *Geology*, *3*(11), 653–656.

Backus, G. E. (1962). Long-wave elastic anisotropy produced by horizontal layering. *Journal of Geophysical Research*, *67*(11), 4427–4440.

Backus, G. E. (1965). Possible forms of seismic anisotropy of the uppermost mantle under oceans. *Journal of Geophysical Research*, *70*(14), 3429–3439.

Bangerth, W., Dannberg, J., Gassmöller, R., & Heister, T. (2019). *ASPECT v2.1.0*. Zenodo. https://doi.org/10.5281/zenodo.2653531

Barbot, S., Lapusta, N., & Avouac, J.-P. (2012). Under the Hood of the Earthquake Machine: Toward Predictive Modeling of the Seismic Cycle. *Science*, *336*(6082), 707–710. https://doi.org/10.1126/science.1218796

Barckhausen, U., Bagge, M., & Wilson, D. S. (2013). Seafloor spreading anomalies and crustal ages of the Clarion-Clipperton Zone. *Marine Geophysical Research*, *34*(2), 79–88. https://doi.org/10.1007/s11001-013-9184-6

Becker, T. W. (2008). Azimuthal seismic anisotropy constrains net rotation of the lithosphere. *Geophysical Research Letters*, *35*(5). https://doi.org/10.1029/2007GL032928

Becker, T. W., Kellogg, J. B., Ekström, G., & O'Connell, R. J. (2003). Comparison of azimuthal seismic anisotropy from surface waves and finite strain from global mantle-circulation models. *Geophysical Journal International*, *155*(2), 696–714.

Becker, T. W., Conrad, C. P., Schaeffer, A. J., & Lebedev, S. (2014). Origin of azimuthal seismic anisotropy in oceanic plates and mantle. *Earth and Planetary Science Letters*, *401*, 236–250. https://doi.org/10.1016/j.epsl.2014.06.014

Beckers, A., Hubert-Ferrari, A., Beck, C., Bodeux, S., Tripsanas, E., Sakellariou, D., & De Batist, M. (2015). Active faulting at the western tip of the Gulf of Corinth, Greece, from high-resolution seismic data. *Marine Geology*, *360*, 55–69. https://doi.org/10.1016/j.margeo.2014.12.003

Beeler, N. M., Tullis, T. E., & Weeks, J. D. (1994). The roles of time and displacement in the evolution effect in rock friction. *Geophysical Research Letters*, *21*(18), 1987–1990. https://doi.org/10.1029/94GL01599

Beghein, C., Yuan, K., Schmerr, N., & Xing, Z. (2014). Changes in Seismic Anisotropy Shed Light on the Nature of the Gutenberg Discontinuity. *Science*, *343*(6176), 1237–1240. https://doi.org/10.1126/science.1246724

Behn, M. D., & Ito, G. (2008). Magmatic and tectonic extension at mid-ocean ridges: 1. Controls on fault characteristics. *Geochemistry, Geophysics, Geosystems*, *9*(8). https://doi.org/10.1029/2008GC001965

Behn, M. D., Conrad, C. P., & Silver, P. G. (2004). Detection of upper mantle flow associated with the African Superplume. *Earth and Planetary Science Letters*, *224*(3), 259–274.

Behn, M. D., Hirth, G., & Elsenbeck II, J. R. (2009). Implications of grain size evolution on the seismic structure of the oceanic upper mantle. *Earth and Planetary Science Letters*, *282*(1–4), 178–189. https://doi.org/10.1016/j.epsl.2009.03.014

Bell, R. E., McNeill, L. C., Bull, J. M., Henstock, T. J., Collier, R. E. L., & Leeder, M. R. (2009). Fault architecture, basin structure and evolution of the Gulf of Corinth Rift, central Greece. *Basin Research*, *21*(6), 824–855. https://doi.org/10.1111/j.1365-2117.2009.00401.x

Ben Ismaïl, W., & Mainprice, D. (1998). An olivine fabric database: an overview of upper mantle fabrics and seismic anisotropy. *Tectonophysics*, *296*(1), 145–157.

Ben-Zion, Y., & Rice, J. R. (1997). Dynamic simulations of slip on a smooth fault in an elastic solid. *Journal of Geophysical Research: Solid Earth*, *102*(B8), 17771–17784. https://doi.org/10.1029/97JB01341

Bergman, E. A., & Solomon, S. C. (1984). Source mechanisms of earthquakes near mid-ocean ridges from body waveform inversion: Implications for the early evolution of oceanic lithosphere. *Journal of Geophysical Research: Solid Earth*, *89*(B13), 11415–11441. https://doi.org/10.1029/JB089iB13p11415

Bernard, P., Briole, P., Meyer, B., Lyon-Caen, H., Gomez, J.-M., Tiberi, C., et al. (1997). The Ms= 6.2, June 15, 1995 Aigion earthquake (Greece): evidence for low angle normal faulting in the Corinth rift. *Journal of Seismology*, *1*(2), 131–150.

Biemiller, J., & Lavier, L. (2017). Earthquake supercycles as part of a spectrum of normal fault slip styles. *Journal of Geophysical Research: Solid Earth*, *122*(4), 2016JB013666. https://doi.org/10.1002/2016JB013666

Birch, F. (1960). The velocity of compressional waves in rocks to 10 kilobars, part 1. *Journal of Geophysical Research*, *65*(4), 1083–1102. https://doi.org/10.1029/JZ065i004p01083

Bird, P., & Kagan, Y. Y. (2004). Plate-tectonic analysis of shallow seismicity: Apparent boundary width, beta, corner magnitude, coupled lithosphere thickness, and coupling in seven tectonic settings. *Bulletin of the Seismological Society of America*, *94*(6), 2380–2399.

Bird, P., Kagan, Y. Y., & Jackson, D. D. (2002). Plate Tectonics and Earthquake Potential of Spreading Ridges and Oceanic Transform Faults. In S. Stein & J. T. Freymueller (Eds.), *Plate Boundary Zones* (pp. 203–218). American Geophysical Union. https://doi.org/10.1029/GD030p0203

Blackman, D. K., & Kendall, J.-M. (2002). Seismic anisotropy in the upper mantle 2. Predictions for current plate boundary flow models. *Geochemistry, Geophysics, Geosystems*, *3*(9), 1 of 26–26 26. https://doi.org/10.1029/2001GC000247

Blackman, D. K., Kendall, J.-M., Dawson, P. R., Wenk, H.-R., Boyce, D., & Morgan, J. P. (1996). Teleseismic imaging of subaxial flow at mid-ocean ridges: Traveltime effects of anisotropic mineral texture in the mantle. *Geophysical Journal International*, *127*(2), 415–426.

Blackman, D. K., Wenk, H.-R., & Kendall, J.-M. (2002). Seismic anisotropy of the upper mantle 1. Factors that affect mineral texture and effective elastic properties. *Geochemistry, Geophysics, Geosystems*, *3*(9), 1–24. https://doi.org/10.1029/2001GC000248

Blackman, D. K., Boyce, D. E., Castelnau, O., Dawson, P. R., & Laske, G. (2017). Effects of crystal preferred orientation on upper mantle flow near plate boundaries: Rheologic feedbacks and seismic anisotropy. *Geophysical Journal International*. https://doi.org/10.1093/gji/ggx251

Blanpied, M. L., Lockner, D. A., & Byerlee, J. D. (1995). Frictional slip of granite at hydrothermal conditions. *Journal of Geophysical Research: Solid Earth*, *100*(B7), 13045–13064. https://doi.org/10.1029/95JB00862

Boettcher, M. S., & Jordan, T. H. (2004). Earthquake scaling relations for mid-ocean ridge transform faults. *Journal of Geophysical Research*, *109*(B12). https://doi.org/10.1029/2004JB003110

Boettcher, M. S., Hirth, G., & Evans, B. (2007). Olivine friction at the base of oceanic seismogenic zones. *Journal of Geophysical Research*, *112*(B1). https://doi.org/10.1029/2006JB004301

Boneh, Y., & Skemer, P. (2014). The effect of deformation history on the evolution of olivine CPO. *Earth and Planetary Science Letters*, *406*, 213–222. https://doi.org/10.1016/j.epsl.2014.09.018

Boneh, Y., Morales, L. F. G., Kaminski, E., & Skemer, P. (2015). Modeling olivine CPO evolution with complex deformation histories: Implications for the interpretation of seismic anisotropy in the mantle. *Geochemistry, Geophysics, Geosystems*, *16*(10), 3436–3455. https://doi.org/10.1002/2015GC005964

Bratt, S. R., & Purdy, G. M. (1984). Structure and variability of oceanic crust on the flanks of the East Pacific Rise between 11° and 13°N. *Journal of Geophysical Research: Solid Earth*, *89*(B7), 6111–6125. https://doi.org/10.1029/JB089iB07p06111

Braun, M. G., Hirth, G., & Parmentier, E. M. (2000). The effects of deep damp melting on mantle flow and melt generation beneath mid-ocean ridges. *Earth and Planetary Science Letters*, *176*(3), 339–356.

Briole, P., Rigo, A., Lyon-Caen, H., Ruegg, J. C., Papazissi, K., Mitsakaki, C., et al. (2000). Active deformation of the Corinth rift, Greece: Results from repeated Global Positioning System surveys between 1990 and 1995. *Journal of Geophysical Research*, *105*, 25. https://doi.org/10.1029/2000JB900148

Browaeys, J. T., & Chevrot, S. (2004). Decomposition of the elastic tensor and geophysical applications. *Geophysical Journal International*, *159*(2), 667–678. https://doi.org/10.1111/j.1365-246X.2004.02415.x

Brune, J. N., Henyey, T. L., & Roy, R. F. (1969). Heat flow, stress, and rate of slip along the San Andreas Fault, California. *Journal of Geophysical Research*, *74*(15), 3821–3827. https://doi.org/10.1029/JB074i015p03821

Buck, W. R., Lavier, L. L., & Poliakov, A. N. (2005). Modes of faulting at mid-ocean ridges. *Nature*, *434*(7034), 719–723.

Burgos, G., Montagner, J.-P., Beucler, E., Capdeville, Y., Mocquet, A., & Drilleau, M. (2014). Oceanic lithosphere-asthenosphere boundary from surface wave dispersion data. *Journal of Geophysical Research: Solid Earth*, *119*(2), 1079–1093. https://doi.org/10.1002/2013JB010528

Byrnes, J. S., Hooft, E. E. E., Toomey, D. R., Villagómez, D. R., Geist, D. J., & Solomon, S. C. (2015). An upper mantle seismic discontinuity beneath the Galápagos Archipelago and its implications for studies of the lithosphere-asthenosphere boundary. *Geochemistry, Geophysics, Geosystems*, *16*(4), 1070–1088. https://doi.org/10.1002/2014GC005694

Calais, E., d'Oreye, N., Albaric, J., Deschamps, A., Delvaux, D., Déverchère, J., et al. (2008). Strain accommodation by slow slip and dyking in a youthful continental rift, East Africa. *Nature*, *456*(7223), 783–787. https://doi.org/10.1038/nature07478

Cannat, M., Mangeney, A., Ondréas, H., Fouquet, Y., & Normand, A. (2013). High-resolution bathymetry reveals contrasting landslide activity shaping the walls of the Mid-Atlantic Ridge

axial valley. *Geochemistry, Geophysics, Geosystems*, *14*(4), 996–1011. https://doi.org/10.1002/ggge.20056

Caress, D. W., Menard, H. W., & Hey, R. N. (2012). Eocene reorganization of the Pacific-Farallon Spreading Center north of the Mendocino Fracture Zone. *Journal of Geophysical Research: Solid Earth*, 2813–2838. https://doi.org/10.1029/JB093iB04p02813

Carlson, R. L., & Miller, D. J. (2003). Mantle wedge water contents estimated from seismic velocities in partially serpentinized peridotites. *Geophysical Research Letters*, *30*(5), 1250. https://doi.org/10.1029/2002GL016600

Cash, J. R., & Karp, A. H. (1990). A variable order Runge-Kutta method for initial value problems with rapidly varying right-hand sides. *ACM Transactions on Mathematical Software (TOMS)*, *16*(3), 201–222.

Chen, T., & Lapusta, N. (2009). Scaling of small repeating earthquakes explained by interaction of seismic and aseismic slip in a rate and state fault model. *Journal of Geophysical Research*, *114*(B1). https://doi.org/10.1029/2008JB005749

Chen, W.-P., & Molnar, P. (1983). Focal depths of intracontinental and intraplate earthquakes and their implications for the thermal and mechanical properties of the lithosphere. *Journal of Geophysical Research: Solid Earth*, *88*(B5), 4183–4214. https://doi.org/10.1029/JB088iB05p04183

Chouliaras, G., Pham, V. N., Boyer, D., Bernard, P., & Stavrakakis, G. N. (1997). Crustal structure of the Gulf of Corinth in Central Greece, determined from magnetotelluric soundings. *Annals of Geophysics*, *40*(1). https://doi.org/10.4401/ag-3935

Christensen, N. I. (1974). Compressional wave velocities in possible mantle rocks to pressures of 30 kilobars. *Journal of Geophysical Research*, *79*(2), 407–412. https://doi.org/10.1029/JB079i002p00407

Christensen, N. I. (1979). Compressional wave velocities in rocks at high temperatures and pressures, critical thermal gradients, and crustal low-velocity zones. *Journal of Geophysical Research: Solid Earth*, *84*(B12), 6849–6857. https://doi.org/10.1029/JB084iB12p06849

Clément, C., Sachpazi, M., Charvis, P., Graindorge, D., Laigle, M., Hirn, A., & Zafiropoulos, G. (2004). Reflection–refraction seismics in the Gulf of Corinth: hints at deep structure and control of the deep marine basin. *Tectonophysics*, *391*(1–4), 97–108. https://doi.org/10.1016/j.tecto.2004.07.010

Collins, J. A. (2002). Upper mantle structure beneath the Hawaiian swell: Constraints from the ocean seismic network pilot experiment. *Geophysical Research Letters*, *29*(11). https://doi.org/10.1029/2001GL013302

Conder, J. A. (2007). Dynamically driven mantle flow and shear wave splitting asymmetry across the EPR, MELT area. *Geophysical Research Letters*, *34*(16). https://doi.org/10.1029/2007GL030832

Conrad, C. P., Behn, M. D., & Silver, P. G. (2007). Global mantle flow and the development of seismic anisotropy: Differences between the oceanic and continental upper mantle. *Journal of Geophysical Research*, *112*(B7). https://doi.org/10.1029/2006JB004608

Constantin, M., Hékinian, R., Ackermand, D., & Stoffers, P. (1995). Mafic and Ultramafic Intrusions into Upper Mantle Peridotites from Fast Spreading Centers of the Easter Microplate (South East Pacific). In *Mantle and Lower Crust Exposed in Oceanic Ridges and in Ophiolites* (pp. 71–120). Springer, Dordrecht. https://doi.org/10.1007/978-94-015-8585-9_4

Cormier, M.-H., Gans, K. D., & Wilson, D. S. (2011). Gravity lineaments of the Cocos Plate: Evidence for a thermal contraction crack origin. *Geochemistry, Geophysics, Geosystems*, *12*(7). https://doi.org/10.1029/2011GC003573

Cowie, P. A., Scholz, C. H., Edwards, M., & Malinverno, A. (1993). Fault strain and seismic coupling on mid-ocean ridges. *Journal of Geophysical Research: Solid Earth*, *98*(B10), 17911–17920. https://doi.org/10.1029/93JB01567

Crampin, S. (1984). An introduction to wave propagation in anisotropic media. *Geophysical Journal International*, *76*(1), 17–28.

Crampin, S., McGonigle, R., & Bamford, D. (1980). Estimating crack parameters from observations of P-wave velocity anisotropy. *Geophysics*, *45*(3), 345–360. https://doi.org/10.1190/1.1441086

Dannberg, J., Eilon, Z., Faul, U., Gassmöller, R., Moulik, P., & Myhill, R. (2017). The importance of grain size to mantle dynamics and seismological observations. *Geochemistry, Geophysics, Geosystems*, *18*(8), 3034–3061. https://doi.org/10.1002/2017GC006944

Debayle, E., & Ricard, Y. (2013). Seismic observations of large-scale deformation at the bottom of fast-moving plates. *Earth and Planetary Science Letters*, *376*, 165–177. https://doi.org/10.1016/j.epsl.2013.06.025

Deichmann, N. (2006). Local Magnitude, a Moment Revisited. *Bulletin of the Seismological Society of America*, *96*(4A), 1267–1277. https://doi.org/10.1785/0120050115

Deichmann, N. (2017). Theoretical Basis for the Observed Break in ML/Mw Scaling between Small and Large Earthquakes. *Bulletin of the Seismological Society of America*, *107*(2), 505–520. https://doi.org/10.1785/0120160318

Demartin, B., Hirth, G., & Evans, B. (2004). Experimental Constraints on Thermal Cracking of Peridotite at Oceanic Spreading Centers. In *Mid-Ocean Ridges* (pp. 167–185). American Geophysical Union (AGU). https://doi.org/10.1029/148GM07

Dick, H. J., Fisher, R. L., & Bryan, W. B. (1984). Mineralogic variability of the uppermost mantle along mid-ocean ridges. *Earth and Planetary Science Letters*, *69*(1), 88–106.

Dieterich, J. H. (1972). Time-dependent friction in rocks. *Journal of Geophysical Research*, *77*(20), 3690–3697. https://doi.org/10.1029/JB077i020p03690

Dieterich, J. H. (1978). Time-dependent friction and the mechanics of stick-slip. *Pure and Applied Geophysics*, *116*(4–5), 790–806.

Dieterich, J. H. (1979). Modeling of rock friction: 1. Experimental results and constitutive equations. *Journal of Geophysical Research: Solid Earth*, *84*(B5), 2161–2168. https://doi.org/10.1029/JB084iB05p02161

Dixon, T. H., Jiang, Y., Malservisi, R., McCaffrey, R., Voss, N., Protti, M., & Gonzalez, V. (2014). Earthquake and tsunami forecasts: Relation of slow slip events to subsequent earthquake rupture. *Proceedings of the National Academy of Sciences of the United States of America*, *111*(48), 17039–17044. https://doi.org/10.1073/pnas.1412299111

Dodge, D. A., Beroza, G. C., & Ellsworth, W. L. (1996). Detailed observations of California foreshock sequences: Implications for the earthquake initiation process. *Journal of Geophysical Research: Solid Earth*, *101*(B10), 22371–22392. https://doi.org/10.1029/96JB02269

Dragert, H., Wang, K., & James, T. S. (2001). A Silent Slip Event on the Deeper Cascadia Subduction Interface. *Science*, *292*(5521), 1525–1528. https://doi.org/10.1126/science.1060152

Dunn, R. A. (2015). Tracking stress and hydrothermal activity along the Eastern Lau Spreading Center using seismic anisotropy. *Earth and Planetary Science Letters*, *410*, 105–116. https://doi.org/10.1016/j.epsl.2014.11.027

Dunn, R. A., & Toomey, D. R. (1997). Seismological evidence for three-dimensional melt migration beneath the East Pacific Rise. *Nature*, *388*(6639), 259–262.

Dziewonski, A. M., & Anderson, D. L. (1981). Preliminary reference Earth model. *Physics of the Earth and Planetary Interiors*, *25*(4), 297–356. https://doi.org/10.1016/0031-9201(81)90046-7

Ebinger, C., Ayele, A., Keir, D., Rowland, J., Yirgu, G., Wright, T., et al. (2010). Length and Timescales of Rift Faulting and Magma Intrusion: The Afar Rifting Cycle from 2005 to Present. *Annual Review of Earth and Planetary Sciences*, *38*(1), 439–466. https://doi.org/10.1146/annurev-earth-040809-152333

Ekstrom, G., & Dziewonski, A. M. (1998). The unique anisotropy of the Pacific upper mantle. *Nature*, *394*(6689), 168–172.

Ekström, G., Nettles, M., & Dziewoński, A. M. (2012). The global CMT project 2004–2010: Centroid-moment tensors for 13,017 earthquakes. *Physics of the Earth and Planetary Interiors*, *200–201*, 1–9. https://doi.org/10.1016/j.pepi.2012.04.002

Ellsworth, W. L., & Beroza, G. C. (1995). Seismic evidence for an earthquake nucleation phase. *Science*, 851–851.

Escartín, J., Hirth, G., & Evans, B. (1997). Effects of serpentinization on the lithospheric strength and the style of normal faulting at slow-spreading ridges. *Earth and Planetary Science Letters*, *151*(3), 181–189. https://doi.org/10.1016/S0012-821X(97)81847-X

Escartín, J., Cowie, P. A., Searle, R. C., Allerton, S., Mitchell, N. C., MacLeod, C. J., & Slootweg, A. P. (1999). Quantifying tectonic strain and magmatic accretion at a slow spreading ridge segment, Mid-Atlantic Ridge, 29°N. *Journal of Geophysical Research: Solid Earth*, *104*(B5), 10421–10437. https://doi.org/10.1029/1998JB900097

Faul, U. H., & Jackson, I. (2005). The seismological signature of temperature and grain size variations in the upper mantle. *Earth and Planetary Science Letters*, *234*(1), 119–134.

Faul, U. H., & Jackson, I. (2007). Diffusion creep of dry, melt-free olivine. *Journal of Geophysical Research: Solid Earth*, *112*(B4). https://doi.org/10.1029/2006JB004586

Fischer, K. M., Ford, H. A., Abt, D. L., & Rychert, C. A. (2010). The Lithosphere-Asthenosphere Boundary. *Annual Review of Earth and Planetary Sciences*, *38*(1), 551–575. https://doi.org/10.1146/annurev-earth-040809-152438

Fowler, C. M. R. (2005). *The Solid Earth: An Introduction to Global Geophysics*. Cambridge University Press.

Francheteau, J., Armijo, R., Cheminée, J. L., Hekinian, R., Lonsdale, P., & Blum, N. (1990). 1 Ma East Pacific Rise oceanic crust and uppermost mantle exposed by rifting in Hess Deep (equatorial Pacific Ocean). *Earth and Planetary Science Letters*, *101*(2–4), 281–295. https://doi.org/10.1016/0012-821X(90)90160-Y

French, S., Lekic, V., & Romanowicz, B. (2013). Waveform tomography reveals channeled flow at the base of the oceanic asthenosphere. *Science*, *342*(6155), 227–230.

Frohlich, C., & Wetzel, L. R. (2007). Comparison of seismic moment release rates along different types of plate boundaries. *Geophysical Journal International*, *171*(2), 909–920. https://doi.org/10.1111/j.1365-246X.2007.03550.x

Froment, B., McGuire, J. J., van der Hilst, R. D., Gouédard, P., Roland, E. C., Zhang, H., & Collins, J. A. (2014). Imaging along-strike variations in mechanical properties of the Gofar transform fault, East Pacific Rise. *Journal of Geophysical Research: Solid Earth*, *119*(9), 7175–7194. https://doi.org/10.1002/2014JB011270

Fuchs, K. (1977). Seismic anisotropy of the subcrustal lithosphere as evidence for dynamical processes in the upper mantle. *Geophysical Journal International*, *49*(1), 167–179.

Gaherty, J. B., Jordan, T. H., & Gee, L. S. (1996). Seismic structure of the upper mantle in a central Pacific corridor. *Journal of Geophysical Research: Solid Earth*, *101*(B10), 22291–22309. https://doi.org/10.1029/96JB01882

Gaherty, J. B., Lizarralde, D., Collins, J. A., Hirth, G., & Kim, S. (2004). Mantle deformation during slow seafloor spreading constrained by observations of seismic anisotropy in the western Atlantic. *Earth and Planetary Science Letters*, *228*(3–4), 255–265. https://doi.org/10.1016/j.epsl.2004.10.026

Garbin, H. D., & Knopoff, L. (1973). The compressional modulus of a material permeated by a random distribution of circular cracks. *Quarterly of Applied Mathematics*, *30*(4), 453–464.

Garbin, H. D., & Knopoff, L. (1975a). Elastic moduli of a medium with liquid-filled cracks. *Quarterly of Applied Mathematics*, *33*(3), 301–303.

Garbin, H. D., & Knopoff, L. (1975b). The shear modulus of a material permeated by a random distribution of free circular cracks. *Quarterly of Applied Mathematics*, *33*(3), 296–300.

Garmany, J. (1981). Anisotropic gradients in the upper mantle. *Geophysical Research Letters*, *8*(9), 955–957. https://doi.org/10.1029/GL008i009p00955

Gealy, E. L. (1971). Sound Velocity, Elastic Constants, and Related Properties of Marine Sediments in the Western Equatorial Pacific: Leg 7, Glomar Challenger, 57. https://doi.org/doi:10.2973/dsdp.proc.7.1971

Ghosh, A., Holt, W. E., Wen, L., Haines, A. J., & Flesch, L. M. (2008). Joint modeling of lithosphere and mantle dynamics elucidating lithosphere-mantle coupling. *Geophysical Research Letters*, *35*(16). https://doi.org/10.1029/2008GL034365

Goff, J. A., & Tucholke, B. E. (1997). Multiscale spectral analysis of bathymetry on the flank of the Mid-Atlantic Ridge: Modification of the seafloor by mass wasting and sedimentation. *Journal of Geophysical Research: Solid Earth*, *102*(B7), 15447–15462. https://doi.org/10.1029/97JB00723

Greenfield, R. J., & Graham, E. K. (1996). Application of a simple relation for describing wave velocity as a function of pressure in rocks containing microcracks. *Journal of Geophysical Research: Solid Earth*, *101*(B3), 5643–5652. https://doi.org/10.1029/95JB03462

Gutenberg, B. (1959). The asthenosphere low-velocity layer. *Annals of Geophysics*, *12*(4), 439–460. https://doi.org/10.4401/ag-5730

Hammond, W. C., & Humphreys, E. D. (2000). Upper mantle seismic wave velocity: Effects of realistic partial melt geometries. *Journal of Geophysical Research: Solid Earth*, *105*(B5), 10975–10986. https://doi.org/10.1029/2000JB900041

Hanks, T. C., & Boore, D. M. (1984). Moment-magnitude relations in theory and practice. *Journal of Geophysical Research: Solid Earth*, *89*(B7), 6229–6235. https://doi.org/10.1029/JB089iB07p06229

Hansen, L. N., Zhao, Y.-H., Zimmerman, M. E., & Kohlstedt, D. L. (2014). Protracted fabric evolution in olivine: Implications for the relationship among strain, crystallographic fabric, and seismic anisotropy. *Earth and Planetary Science Letters*, *387*, 157–168. https://doi.org/10.1016/j.epsl.2013.11.009

Hansen, L. N., Qi, C., & Warren, J. M. (2016). Olivine anisotropy suggests Gutenberg discontinuity is not the base of the lithosphere. *Proceedings of the National Academy of Sciences*, *113*(38), 10503–10506. https://doi.org/10.1073/pnas.1608269113

Hansen, L. N., Conrad, C. P., Boneh, Y., Skemer, P., Warren, J. M., & Kohlstedt, D. L. (2016). Viscous anisotropy of textured olivine aggregates: 2. Micromechanical model. *Journal of Geophysical Research: Solid Earth*, *121*(10), 7137–7160. https://doi.org/10.1002/2016JB013240

He, C., Wang, Z., & Yao, W. (2007). Frictional sliding of gabbro gouge under hydrothermal conditions. *Tectonophysics*, *445*(3–4), 353–362. https://doi.org/10.1016/j.tecto.2007.09.008

Hedjazian, N., & Kaminski, E. (2014). Defining a proxy for the interpretation of seismic anisotropy in non-Newtonian mantle flows. *Geophysical Research Letters*, *41*(20), 7065–7072. https://doi.org/10.1002/2014GL061372

Hedjazian, Navid, Garel, F., Davies, D. R., & Kaminski, E. (2017). Age-independent seismic anisotropy under oceanic plates explained by strain history in the asthenosphere. *Earth and Planetary Science Letters*, *460*, 135–142. https://doi.org/10.1016/j.epsl.2016.12.004

Heister, T., Dannberg, J., Gassmöller, R., & Bangerth, W. (2017). High accuracy mantle convection simulation through modern numerical methods – II: realistic models and problems. *Geophysical Journal International*, *210*(2), 833–851. https://doi.org/10.1093/gji/ggx195

Hekinian, R., Bideau, D., Francheteau, J., Cheminee, J. L., Armijo, R., Lonsdale, P., & Blum, N. (1993). Petrology of the East Pacific Rise crust and upper mantle exposed in Hess deep (eastern equatorial Pacific). *Journal of Geophysical Research: Solid Earth*, *98*(B5), 8069–8094. https://doi.org/10.1029/92JB02072

Helffrich, G. (2006). Extended-Time Multitaper Frequency Domain Cross-Correlation Receiver-Function Estimation. *Bulletin of the Seismological Society of America*, *96*(1), 344–347. https://doi.org/10.1785/0120050098

Henkart, P. (2003). Seismic processing system SIOSEIS. Retrieved March 20, 2017, from http://sioseis.ucsd.edu/

Hess, H. H. (1964). Seismic Anisotropy of the Uppermost Mantle under Oceans. *Nature*, *203*(4945), 629–631. https://doi.org/10.1038/203629a0

Hirschmann, M. M. (2010). Partial melt in the oceanic low velocity zone. *Physics of the Earth and Planetary Interiors*, *179*(1–2), 60–71. https://doi.org/10.1016/j.pepi.2009.12.003

Hirth, G., & Guillot, S. (2013). Rheology and Tectonic Significance of Serpentinite. *Elements*, *9*(2), 107–113. https://doi.org/10.2113/gselements.9.2.107

Hirth, G., & Kohlstedt, D. (2004). Rheology of the Upper Mantle and the Mantle Wedge: A View from the Experimentalists. In J. Eiler (Ed.), *Inside the Subduction Factory* (pp. 83–105). American Geophysical Union. https://doi.org/10.1029/138GM06

Hirth, G., & Kohlstedt, D. L. (1996). Water in the oceanic upper mantle: implications for rheology, melt extraction and the evolution of the lithosphere. *Earth and Planetary Science Letters*, *144*(1–2), 93–108.

Höink, T., Jellinek, A. M., & Lenardic, A. (2011). Viscous coupling at the lithosphere-asthenosphere boundary. *Geochemistry, Geophysics, Geosystems*, *12*(10), Q0AK02. https://doi.org/10.1029/2011GC003698

Holtzman, B. K., Kohlstedt, D. L., Zimmerman, M. E., Heidelbach, F., Hiraga, T., & Hustoft, J. (2003). Melt segregation and strain partitioning: Implications for seismic anisotropy and mantle flow. *Science*, *301*(5637), 1227–1230.

Hopper, E., Ford, H. A., Fischer, K. M., Lekic, V., & Fouch, M. J. (2014). The lithosphere–asthenosphere boundary and the tectonic and magmatic history of the northwestern United States. *Earth and Planetary Science Letters*, *402*, 69–81. https://doi.org/10.1016/j.epsl.2013.12.016

Houston, H., Delbridge, B. G., Wech, A. G., & Creager, K. C. (2011). Rapid tremor reversals in Cascadia generated by a weakened plate interface. *Nature Geoscience; London*, *4*(6), 404–409. http://dx.doi.org/10.1038/ngeo1157

Howell, S. M., Ito, G., Behn, M. D., Martinez, F., Olive, J.-A., & Escartín, J. (2016). Magmatic and tectonic extension at the Chile Ridge: Evidence for mantle controls on ridge segmentation. *Geochemistry, Geophysics, Geosystems*, *17*(6), 2354–2373. https://doi.org/10.1002/2016GC006380

Hudson, J. A. (1981). Wave speeds and attenuation of elastic waves in material containing cracks. *Geophysical Journal International*, *64*(1), 133–150.

International Seismological Centre. (2017). On-line Bulletin. Retrieved October 16, 2017, from http://www.isc.ac.uk

Jackson, I., Gerald, J. D. F., Faul, U. H., & Tan, B. H. (2002). Grain-size-sensitive seismic wave attenuation in polycrystalline olivine. *Journal of Geophysical Research: Solid Earth*, *107*(B12), ECV 5-1-ECV 5-16. https://doi.org/10.1029/2001JB001225

Jin, A., Moya, C. A., & Ando, M. (2000). Simultaneous Determination of Site Responses and Source Parameters of Small Earthquakes along the Atotsugawa Fault Zone, Central Japan. *Bulletin of the Seismological Society of America*, *90*(6), 1430–1445. https://doi.org/10.1785/0119990140

Johnson, K. M., Bürgmann, R., & Larson, K. (2006). Frictional Properties on the San Andreas Fault near Parkfield, California, Inferred from Models of Afterslip following the 2004 Earthquake. *Bulletin of the Seismological Society of America*, *96*(4B), S321–S338. https://doi.org/10.1785/0120050808

Jung, H., & Karato, S. (2001). Water-Induced Fabric Transitions in Olivine. *Science*, *293*(5534), 1460–1463. https://doi.org/10.1126/science.1062235

Kaminski, E., & Ribe, N. M. (2001). A kinematic model for recrystallization and texture development in olivine polycrystals. *Earth and Planetary Science Letters*, *189*(3–4), 253–267. https://doi.org/10.1016/S0012-821X(01)00356-9

Kaminski, E., & Ribe, N. M. (2002). Timescales for the evolution of seismic anisotropy in mantle flow. *Geochemistry, Geophysics, Geosystems*, *3*(8), 1–17.

Kaminski, E., Ribe, N. M., & Browaeys, J. T. (2004). D-Rex, a program for calculation of seismic anisotropy due to crystal lattice preferred orientation in the convective upper mantle. *Geophysical Journal International*, *158*(2), 744–752. https://doi.org/10.1111/j.1365-246X.2004.02308.x

Karato, S.-I. (2012). On the origin of the asthenosphere. *Earth and Planetary Science Letters*, *321–322*, 95–103. https://doi.org/10.1016/j.epsl.2012.01.001

Karato, S.-I., Paterson, M. S., & FitzGerald, J. D. (1986). Rheology of synthetic olivine aggregates: Influence of grain size and water. *Journal of Geophysical Research: Solid Earth*, *91*(B8), 8151–8176. https://doi.org/10.1029/JB091iB08p08151

Kato, A., Obara, K., Igarashi, T., Tsuruoka, H., Nakagawa, S., & Hirata, N. (2012). Propagation of Slow Slip Leading Up to the 2011 Mw 9.0 Tohoku-Oki Earthquake. *Science*, *335*(6069), 705–708. https://doi.org/10.1126/science.1215141

Kawakatsu, H., Kumar, P., Takei, Y., Shinohara, M., Kanazawa, T., Araki, E., & Suyehiro, K. (2009). Seismic Evidence for Sharp Lithosphere-Asthenosphere Boundaries of Oceanic Plates. *Science*, *324*(5926), 499–502. https://doi.org/10.1126/science.1169499

Keen, C. E., & Barrett, D. L. (1971). A Measurement of Seismic Anistropy in the Northeast Pacific. *Canadian Journal of Earth Sciences*, *8*(9), 1056–1064.

Keen, C. E., & Tramontini, C. (1970). A seismic refraction survey on the Mid-Atlantic Ridge. *Geophysical Journal International*, *20*(5), 473–491.

Keir, D., Ebinger, C. J., Stuart, G. W., Daly, E., & Ayele, A. (2006). Strain accommodation by magmatism and faulting as rifting proceeds to breakup: Seismicity of the northern Ethiopian

rift. *Journal of Geophysical Research: Solid Earth*, *111*(B5). https://doi.org/10.1029/2005JB003748

Kelemen, P. B., Dick, H. J. B., & Quick, J. E. (1992). Formation of harzburgite by pervasive melt/rock reaction in the upper mantle. *Nature*, *358*(6388), 635–641. https://doi.org/10.1038/358635a0

Korenaga, J. (2007). Thermal cracking and the deep hydration of oceanic lithosphere: A key to the generation of plate tectonics? *Journal of Geophysical Research*, *112*(B5). https://doi.org/10.1029/2006JB004502

Kronbichler, M., Heister, T., & Bangerth, W. (2012). High accuracy mantle convection simulation through modern numerical methods: High accuracy mantle convection simulation. *Geophysical Journal International*, *191*(1), 12–29. https://doi.org/10.1111/j.1365-246X.2012.05609.x

Kumar, P., & Kawakatsu, H. (2011). Imaging the seismic lithosphere-asthenosphere boundary of the oceanic plate. *Geochemistry, Geophysics, Geosystems*, *12*(1). https://doi.org/10.1029/2010GC003358

Lambotte, S., Lyon-Caen, H., Bernard, P., Deschamps, A., Patau, G., Nercessian, A., et al. (2014). Reassessment of the rifting process in the Western Corinth Rift from relocated seismicity. *Geophysical Journal International*, *197*(3), 1822–1844. https://doi.org/10.1093/gji/ggu096

Langmuir, C. H., Klein, E. M., & Plank, T. (1992). Petrological Systematics of Mid-Ocean Ridge Basalts: Constraints on Melt Generation Beneath Ocean Ridges. In J. P. Morgan, D. K. Blackman, & J. M. Sinton (Eds.), *Mantle Flow and Melt Generation at Mid-Ocean Ridges* (pp. 183–280). American Geophysical Union. https://doi.org/10.1029/GM071p0183

Lapusta, N., & Liu, Y. (2009). Three-dimensional boundary integral modeling of spontaneous earthquake sequences and aseismic slip. *Journal of Geophysical Research*, *114*(B9). https://doi.org/10.1029/2008JB005934

Lapusta, N., Rice, J. R., Ben-Zion, Y., & Zheng, G. (2000). Elastodynamic analysis for slow tectonic loading with spontaneous rupture episodes on faults with rate- and state-dependent friction. *Journal of Geophysical Research: Solid Earth*, *105*(B10), 23765–23789. https://doi.org/10.1029/2000JB900250

Lenardic, A., Richards, M. A., & Busse, F. H. (2006). Depth-dependent rheology and the horizontal length scale of mantle convection. *Journal of Geophysical Research: Solid Earth*, *111*(B7). https://doi.org/10.1029/2005JB003639

Lev, E., & Hager, B. H. (2008). Prediction of anisotropy from flow models: A comparison of three methods. *Geochemistry, Geophysics, Geosystems*, *9*(7), n/a-n/a. https://doi.org/10.1029/2008GC002032

Lin, P.-Y. P., Gaherty, J. B., Jin, G., Collins, J. A., Lizarralde, D., Evans, Rob. L., & Hirth, G. (2016). High-resolution seismic constraints on flow dynamics in the oceanic asthenosphere. *Nature*, *535*(7613), 538–541. https://doi.org/10.1038/nature18012

Linde, A. T., & Silver, P. G. (1989). Elevation changes and the Great 1960 Chilean Earthquake: Support for aseismic slip. *Geophysical Research Letters*, *16*(11), 1305–1308. https://doi.org/10.1029/GL016i011p01305

Linde, A. T., Gladwin, M. T., Johnston, M. J. S., Gwyther, R. L., & Bilham, R. G. (1996). A slow earthquake sequence on the San Andreas fault. *Nature*, *383*(6595), 65–68. http://dx.doi.org/10.1038/383065a0

Liu, Y., & Rice, J. R. (2005). Aseismic slip transients emerge spontaneously in three-dimensional rate and state modeling of subduction earthquake sequences. *Journal of Geophysical Research*, *110*(B8). https://doi.org/10.1029/2004JB003424

Liu, Y., & Rice, J. R. (2007). Spontaneous and triggered aseismic deformation transients in a subduction fault model. *Journal of Geophysical Research*, *112*(B9). https://doi.org/10.1029/2007JB004930

Liu, Y., McGuire, J. J., & Behn, M. D. (2012). Frictional behavior of oceanic transform faults and its influence on earthquake characteristics. *Journal of Geophysical Research: Solid Earth*, *117*(B4). https://doi.org/10.1029/2011JB009025

Lizarralde, D., Gaherty, J. B., Collins, J. A., Hirth, G., & Evans, R. L. (2018). A lithospheric-mantle phase boundary at 30 km depth beneath the northeast Pacific NoMelt site. *AGU Fall Meeting Abstracts*, *23*. Retrieved from http://adsabs.harvard.edu/abs/2018AGUFM.T23E0427L

Lonsdale, P. (1988). Paleogene history of the Kula plate: Offshore evidence and onshore implications. *GSA Bulletin*, *100*(5), 733–754. https://doi.org/10.1130/0016-7606(1988)100<0733:PHOTKP>2.3.CO;2

Ma, Z., Dalton, C. A., Forsyth, D. W., & Gaherty, J. B. (2018). Seismic attenuation structure of the Pacific upper mantle in the NoMelt experiment region as constrained by Rayleigh waves from earthquakes. *AGU Fall Meeting Abstracts*, *23*. Retrieved from http://adsabs.harvard.edu/abs/2018AGUFM.T23E0428M

Macdonald, K. C., Scheirer, D. S., & Carbotte, S. M. (1991). Mid-Ocean Ridges: Discontinuities, Segments and Giant Cracks. *Science*, *253*(5023), 986–994. https://doi.org/10.1126/science.253.5023.986

Macdonald, K. C., Fox, P. J., Miller, S., Carbotte, S., Edwards, M. H., Eisen, M., et al. (1992). The East Pacific Rise and its flanks 8–18° N: History of segmentation, propagation and spreading direction based on SeaMARC II and Sea Beam studies. *Marine Geophysical Researches*, *14*(4), 299–344. https://doi.org/10.1007/BF01203621

Maggi, A., Debayle, E., Priestley, K., & Barruol, G. (2006). Azimuthal anisotropy of the Pacific region. *Earth and Planetary Science Letters*, *250*(1–2), 53–71. https://doi.org/10.1016/j.epsl.2006.07.010

Mainprice, D. (2015). Seismic Anisotropy of the Deep Earth from a Mineral and Rock Physics Perspective. In *Treatise on Geophysics* (pp. 487–538). Elsevier. https://doi.org/10.1016/B978-0-444-53802-4.00044-0

Mainprice, D., Barruol, G., & Ismaïl, W. B. (2000). The Seismic Anisotropy of the Earth's Mantle: from Single Crystal to Polycrystal. In S.-I. Karato, A. Forte, R. Liebermann, Guysters, & L. Stixrude (Eds.), *Earth's Deep Interior: Mineral Physics and Tomography From the Atomic to the Global Scale* (pp. 237–264). American Geophysical Union. https://doi.org/10.1029/GM117p0237

Makropoulos, K., Kaviris, G., & Kouskouna, V. (2012). An updated and extended earthquake catalogue for Greece and adjacent areas since 1900. *Natural Hazards and Earth System Science*, *12*(5), 1425–1430. https://doi.org/10.5194/nhess-12-1425-2012

Marone, C. (1998). Laboratory-derived friction laws and their application to seismic faulting. *Annual Review of Earth and Planetary Sciences*, *26*(1), 643–696.

Marone, C., & Cox, S. J. D. (1994). Scaling of rock friction constitutive parameters: The effects of surface roughness and cumulative offset on friction of gabbro. *Pure and Applied Geophysics*, *143*(1), 359–385.

Matsuno, T., & Evans, Rob. L. (2017). Constraints on lithospheric mantle and crustal anisotropy in the NoMelt area from an analysis of long-period seafloor magnetotelluric data. *Earth, Planets and Space*, *69*(1). https://doi.org/10.1186/s40623-017-0724-1

McGuire, J. J. (2008). Seismic Cycles and Earthquake Predictability on East Pacific Rise Transform Faults. *Bulletin of the Seismological Society of America*, *98*(3), 1067–1084. https://doi.org/10.1785/0120070154

McGuire, J. J., Boettcher, M. S., & Jordan, T. H. (2005). Foreshock sequences and short-term earthquake predictability on East Pacific Rise transform faults. *Nature*, *434*(7032), 457–461. https://doi.org/10.1038/nature03377

McGuire, J. J., Collins, J. A., Gouédard, P., Roland, E., Lizarralde, D., Boettcher, M. S., et al. (2012). Variations in earthquake rupture properties along the Gofar transform fault, East Pacific Rise. *Nature Geoscience*, *5*(5), 336–341. https://doi.org/10.1038/ngeo1454

McKenzie, D. (1979). Finite deformation during fluid flow. *Geophysical Journal International*, *58*(3), 689–715.

Mckenzie, D., Jackson, J., & Priestley, K. (2005). Thermal structure of oceanic and continental lithosphere. *Earth and Planetary Science Letters*, *233*(3–4), 337–349. https://doi.org/10.1016/j.epsl.2005.02.005

Meglis, I. L., Greenfield, R. J., Engelder, T., & Graham, E. K. (1996). Pressure dependence of velocity and attenuation and its relationship to crack closure in crystalline rocks. *Journal of Geophysical Research: Solid Earth*, *101*(B8), 17523–17533. https://doi.org/10.1029/96JB00107

Métois, M., Socquet, A., & Vigny, C. (2012). Interseismic coupling, segmentation and mechanical behavior of the central Chile subduction zone. *Journal of Geophysical Research: Solid Earth*, *117*(B3). https://doi.org/10.1029/2011JB008736

Micarelli, L., Moretti, I., & Daniel, J. M. (2003). Structural properties of rift-related normal faults: the case study of the Gulf of Corinth, Greece. *Journal of Geodynamics*, *36*(1–2), 275–303. https://doi.org/10.1016/S0264-3707(03)00051-6

Miller, M. M., Melbourne, T., Johnson, D. J., & Sumner, W. Q. (2002). Periodic Slow Earthquakes from the Cascadia Subduction Zone. *Science*, *295*(5564), 2423–2423. https://doi.org/10.1126/science.1071193

Mishra, J. K., & Gordon, R. G. (2016). The rigid-plate and shrinking-plate hypotheses: Implications for the azimuths of transform faults. *Tectonics*, *35*(8), 1827–1842. https://doi.org/10.1002/2015TC003968

Montagner, J.-P. (2002). Upper mantle low anisotropy channels below the Pacific Plate. *Earth and Planetary Science Letters*, *202*(2), 263–274. https://doi.org/10.1016/S0012-821X(02)00791-4

Montési, L. G. J., & Behn, M. D. (2007). Mantle flow and melting underneath oblique and ultraslow mid-ocean ridges. *Geophysical Research Letters*, *34*(24). https://doi.org/10.1029/2007GL031067

Moretti, I., Sakellariou, D., Lykousis, V., & Micarelli, L. (2003). The Gulf of Corinth: an active half graben? *Journal of Geodynamics*, *36*(1–2), 323–340. https://doi.org/10.1016/S0264-3707(03)00053-X

Morris, G. B., Raitt, R. W., & Shor, G. G. (1969). Velocity anisotropy and delay-time maps of the mantle near Hawaii. *Journal of Geophysical Research*, *74*(17), 4300–4316.

Naif, S., Key, K., Constable, S., & Evans, R. L. (2013). Melt-rich channel observed at the lithosphere–asthenosphere boundary. *Nature*, *495*(7441), 356–359. https://doi.org/10.1038/nature11939

Nettles, M., & Dziewoński, A. M. (2008). Radially anisotropic shear velocity structure of the upper mantle globally and beneath North America. *Journal of Geophysical Research*, *113*(B2). https://doi.org/10.1029/2006JB004819

Nicolas, A., & Christensen, N. I. (1987). Formation of Anisotropy in Upper Mantle Peridotites - A Review. In K. Fuchs & C. Froidevaux (Eds.), *Composition, Structure and Dynamics of the Lithosphere-Asthenosphere System* (pp. 111–123). American Geophysical Union. https://doi.org/10.1029/GD016p0111

Nicolas, A., Boudier, F., & Boullier, A. M. (1973). Mechanisms of flow in naturally and experimentally deformed peridotites. *American Journal of Science*, *273*(10), 853–876. https://doi.org/10.2475/ajs.273.10.853

Nishizawa, O. (1982). Seismic velocity anisotropy in a medium containing oriented cracks—Transversely isotropic case. *J. Phys. Earth*, *30*(4), 331–347.

Okada, Y. (1992). Internal deformation due to shear and tensile faults in a half-space. *Bulletin of the Seismological Society of America*, *82*(2), 1018–1040.

Olive, J.-A., & Escartín, J. (2016). Dependence of seismic coupling on normal fault style along the Northern Mid-Atlantic Ridge. *Geochemistry, Geophysics, Geosystems*, *17*(10), 4128–4152. https://doi.org/10.1002/2016GC006460

Olugboji, T. M., Park, J., Karato, S., & Shinohara, M. (2016). Nature of the seismic lithosphere-asthenosphere boundary within normal oceanic mantle from high-resolution receiver functions. *Geochemistry, Geophysics, Geosystems*, *17*(4), 1265–1282. https://doi.org/10.1002/2015GC006214

Pacheco, J. F., Sykes, L. R., & Scholz, C. H. (1993). Nature of seismic coupling along simple plate boundaries of the subduction type. *Journal of Geophysical Research: Solid Earth*, *98*(B8), 14133–14159. https://doi.org/10.1029/93JB00349

Pälike, H., Lyle, M., Nishi, H., Raffi, I., Gamage, K., Klaus, A., & Expedition 320/321 Scientists (Eds.). (2010a). *Site U1331* (Vol. 320/321). Integrated Ocean Drilling Program. https://doi.org/10.2204/iodp.proc.320321.2010

Pälike, H., Lyle, M., Nishi, H., Raffi, I., Gamage, K., Klaus, A., & Expedition 320/321 Scientists (Eds.). (2010b). *Site U1332* (Vol. 320/321). Integrated Ocean Drilling Program. https://doi.org/10.2204/iodp.proc.320321.2010

Papazachos, B. C., Kiratzi, A. A., & Karacostas, B. G. (1997). Toward a homogeneous moment-magnitude determination for earthquakes in Greece and the surrounding area. *Bulletin of the Seismological Society of America*, *87*(2), 474–483.

Park, J., & Levin, V. (2000). Receiver Functions from Multiple-Taper Spectral Correlation Estimates. *Bulletin of the Seismological Society of America*, *90*(6), 1507–1520. https://doi.org/10.1785/0119990122

Park, J., Lindberg, C. R., & Vernon, F. L. (1987). Multitaper spectral analysis of high-frequency seismograms. *Journal of Geophysical Research: Solid Earth*, *92*(B12), 12675–12684. https://doi.org/10.1029/JB092iB12p12675

Peng, Z., & Gomberg, J. (2010). An integrated perspective of the continuum between earthquakes and slow-slip phenomena. *Nature Geoscience*, *3*, 9. https://doi.org/10.1038/ngeo940

Phipps Morgan, J. (1997). The generation of a compositional lithosphere by mid-ocean ridge melting and its effect on subsequent off-axis hotspot upwelling and melting. *Earth and Planetary Science Letters*, *146*(1–2), 213–232.

Phipps Morgan, J., Parmentier, E. M., & Lin, J. (1987). Mechanisms for the origin of mid-ocean ridge axial topography: Implications for the thermal and mechanical structure of accreting plate boundaries. *Journal of Geophysical Research: Solid Earth*, *92*(B12), 12823–12836. https://doi.org/10.1029/JB092iB12p12823

Podolefsky, N. S., Zhong, S., & McNamara, A. K. (2004). The anisotropic and rheological structure of the oceanic upper mantle from a simple model of plate shear. *Geophysical Journal International*, *158*, 287–296.

Qi, C., Hansen, L. N., Wallis, D., Holtzman, B. K., & Kohlstedt, D. L. (2018). Crystallographic Preferred Orientation of Olivine in Sheared Partially Molten Rocks: The Source of the "A-C Switch." *Geochemistry, Geophysics, Geosystems*. https://doi.org/10.1002/2017GC007309

Radiguet, M., Perfettini, H., Cotte, N., Gualandi, A., Valette, B., Kostoglodov, V., et al. (2016). Triggering of the 2014 Mw7.3 Papanoa earthquake by a slow slip event in Guerrero, Mexico. *Nature Geoscience*, *9*(11), 829–833. https://doi.org/10.1038/ngeo2817

Raitt, R. W., Shor, G. G., Francis, T. J. G., & Morris, G. B. (1969). Anisotropy of the Pacific upper mantle. *Journal of Geophysical Research*, *74*(12), 3095–3109. https://doi.org/10.1029/JB074i012p03095

Raitt, R. W., Shor, G. G., Morris, G. B., & Kirk, H. K. (1971). Mantle anisotropy in the Pacific Ocean. *Tectonophysics*, *12*(3), 173–186. https://doi.org/10.1016/0040-1951(71)90002-3

Reinen, L. A., Weeks, J. D., & Tullis, T. E. (1991). The frictional behavior of serpentinite: Implications for aseismic creep on shallow crustal faults. *Geophysical Research Letters*, *18*(10), 1921–1924.

Reinen, L. A., Weeks, J. D., & Tullis, T. E. (1994). The frictional behavior of lizardite and antigorite serpentinites: Experiments, constitutive models, and implications for natural faults. *Pure and Applied Geophysics*, *143*(1), 317–358.

Ribe, N. M. (1992). On the relation between seismic anisotropy and finite strain. *Journal of Geophysical Research: Solid Earth*, *97*(B6), 8737–8747. https://doi.org/10.1029/92JB00551

Rice, J. R. (1993). Spatio-temporal complexity of slip on a fault. *Journal of Geophysical Research: Solid Earth*, *98*(B6), 9885–9907. https://doi.org/10.1029/93JB00191

Rice, J. R., & Ben-Zion, Y. (1996). Slip complexity in earthquake fault models. *Proceedings of the National Academy of Sciences*, *93*(9), 3811–3818.

Rice, J. R., & Ruina, A. L. (1983). Stability of Steady Frictional Slipping. *Journal of Applied Mechanics*, *50*(2), 343–349. https://doi.org/10.1115/1.3167042

Richards, M. A., & Lenardic, A. (2018). The Cathles Parameter ( Ct): A Geodynamic Definition of the Asthenosphere and Implications for the Nature of Plate Tectonics. *Geochemistry, Geophysics, Geosystems*. https://doi.org/10.1029/2018GC007664

Richards, M. A., Yang, W.-S., Baumgardner, J. R., & Bunge, H.-P. (2001). Role of a low-viscosity zone in stabilizing plate tectonics: Implications for comparative terrestrial planetology. *Geochemistry, Geophysics, Geosystems*, *2*(8). https://doi.org/10.1029/2000GC000115

Richter, F. M. (1973). Convection and the large-scale circulation of the mantle. *Journal of Geophysical Research*, *78*(35), 8735–8745. https://doi.org/10.1029/JB078i035p08735

Richter, F. M., & Parsons, B. (1975). On the interaction of two scales of convection in the mantle. *Journal of Geophysical Research*, *80*(17), 2529–2541. https://doi.org/10.1029/JB080i017p02529

Rigo, A., Lyon-Caen, H., Armijo, R., Deschamps, A., Hatzfeld, D., Makropoulos, K., et al. (1996). A microseismic study in the western part of the Gulf of Corinth (Greece): implications for large-scale normal faulting mechanisms. *Geophysical Journal International*, *126*(3), 663–688. https://doi.org/10.1111/j.1365-246X.1996.tb04697.x

Ringwood, A. E. (1958). The constitution of the mantle—III Consequences of the olivine-spinel transition. *Geochimica et Cosmochimica Acta*, *15*(3), 195–212. https://doi.org/10.1016/0016-7037(58)90057-7

Ritzwoller, M. H., Shapiro, N. M., & Zhong, S.-J. (2004). Cooling history of the Pacific lithosphere. *Earth and Planetary Science Letters*, *226*(1–2), 69–84. https://doi.org/10.1016/j.epsl.2004.07.032

Roland, E., Lizarralde, D., McGuire, J. J., & Collins, J. A. (2012). Seismic velocity constraints on the material properties that control earthquake behavior at the Quebrada-Discovery-Gofar transform faults, East Pacific Rise. *Journal of Geophysical Research: Solid Earth*, *117*(B11), B11102. https://doi.org/10.1029/2012JB009422

Rubin, A. M., & Ampuero, J.-P. (2005). Earthquake nucleation on (aging) rate and state faults. *Journal of Geophysical Research: Solid Earth*, *110*(B11). https://doi.org/10.1029/2005JB003686

Ruina, A. (1983). Slip instability and state variable friction laws. *Journal of Geophysical Research: Solid Earth*, *88*(B12), 10359–10370. https://doi.org/10.1029/JB088iB12p10359

Rundquist, D. V., & Sobolev, P. O. (2002). Seismicity of mid-oceanic ridges and its geodynamic implications: a review. *Earth-Science Reviews*, *58*(1–2), 143–161. https://doi.org/10.1016/S0012-8252(01)00086-1

Russell, J. B., Gaherty, J. B., Lin, P.-Y. P., Lizarralde, D., Collins, J. A., Hirth, G., & Evans, R. L. (2019). High-Resolution Constraints on Pacific Upper Mantle Petrofabric Inferred From Surface-Wave Anisotropy. *Journal of Geophysical Research: Solid Earth*. https://doi.org/10.1029/2018JB016598

Ryan, W. B. F., Carbotte, S. M., Coplan, J. O., O'Hara, S., Melkonian, A., Arko, R., et al. (2009). Global Multi-Resolution Topography synthesis. *Geochemistry, Geophysics, Geosystems*, *10*(3), Q03014. https://doi.org/10.1029/2008GC002332

Rychert, C. A., Rondenay, S., & Fischer, K. M. (2007). P-to-S and S-to-P imaging of a sharp lithosphere-asthenosphere boundary beneath eastern North America. *Journal of Geophysical Research*, *112*(B8). https://doi.org/10.1029/2006JB004619

Rychert, C. A., Harmon, N., & Tharimena, S. (2018). Scattered wave imaging of the oceanic plate in Cascadia. *Science Advances*, *4*(2), eaao1908.

Sandwell, D., & Fialko, Y. (2004). Warping and cracking of the Pacific plate by thermal contraction. *Journal of Geophysical Research: Solid Earth*, *109*(B10). https://doi.org/10.1029/2004JB003091

Sarafian, E., Evans, Rob. L., Collins, J. A., Elsenbeck, J., Gaetani, G. A., Gaherty, J. B., et al. (2015). The electrical structure of the central Pacific upper mantle constrained by the NoMelt experiment. *Geochemistry, Geophysics, Geosystems*, *16*(4), 1115–1132. https://doi.org/10.1002/2014GC005709

Sasajima, R., & Ito, T. (2017). Anisotropic Horizontal Thermal Contraction of Young Oceanic Lithosphere Inferred From Stress Release Due To Oceanic Intraplate Earthquakes. *Tectonics*. https://doi.org/10.1002/2017TC004680

Savage, M. K. (1999). Seismic anisotropy and mantle deformation: What have we learned from shear wave splitting? *Reviews of Geophysics*, *37*(1), 65–106. https://doi.org/10.1029/98RG02075

Schmerr, N. (2012). The Gutenberg Discontinuity: Melt at the Lithosphere-Asthenosphere Boundary. *Science*, *335*(6075), 1480–1483. https://doi.org/10.1126/science.1215433

Scholz, C. H. (1998). Earthquakes and friction laws. *Nature*, *391*(6662), 37–42. https://doi.org/10.1038/34097

Scholz, C. H., & Campos, J. (1995). On the mechanism of seismic decoupling and back arc spreading at subduction zones. *Journal of Geophysical Research: Solid Earth*, *100*(B11), 22103–22115. https://doi.org/10.1029/95JB01869

Scholz, C. H., & Campos, J. (2012). The seismic coupling of subduction zones revisited. *Journal of Geophysical Research: Solid Earth*, *117*(B5), B05310. https://doi.org/10.1029/2011JB009003

Schwartz, S. Y., & Rokosky, J. M. (2007). Slow slip events and seismic tremor at circum-Pacific subduction zones. *Reviews of Geophysics*, *45*(3), RG3004. https://doi.org/10.1029/2006RG000208

Segall, P., Desmarais, E. K., Shelly, D., Miklius, A., & Cervelli, P. (2006). Earthquakes triggered by silent slip events on Kīlauea volcano, Hawaii. *Nature*, *442*(7098), 71–74. https://doi.org/10.1038/nature04938

Seton, M., Müller, R. D., Zahirovic, S., Gaina, C., Torsvik, T., Shephard, G., et al. (2012). Global continental and ocean basin reconstructions since 200Ma. *Earth-Science Reviews*, *113*(3–4), 212–270. https://doi.org/10.1016/j.earscirev.2012.03.002

Shearer, P. M., & Orcutt, J. (1985). Anisotropy in the oceanic lithosphere — theory and observations from the Ngendei seismic refraction experiment in the south-west Pacific. *Geophysical Journal of the Royal Astronomical Society*, *80*(2), 493–526. https://doi.org/10.1111/j.1365-246X.1985.tb05105.x

Shearer, P. M., & Orcutt, J. A. (1986). Compressional and shear wave anisotropy in the oceanic lithosphere - the Ngendei seismic refraction experiment. *Geophysical Journal International*, *87*(3), 967–1003. https://doi.org/10.1111/j.1365-246X.1986.tb01979.x

Shibutani, T., Ueno, T., & Hirahara, K. (2008). Improvement in the Extended-Time Multitaper Receiver Function Estimation Technique. *Bulletin of the Seismological Society of America*, *98*(2), 812–816. https://doi.org/10.1785/0120070226

Shimamura, H. (1984). Anisotropy in the oceanic lithosphere of the North-western Pacific Basin. *Geophysical Journal International*, *76*(1), 253–260. https://doi.org/10.1111/j.1365-246X.1984.tb05042.x

Shintaku, N., Forsyth, D. W., Hajewski, C. J., & Weeraratne, D. S. (2014). Pn anisotropy in Mesozoic western Pacific lithosphere. *Journal of Geophysical Research: Solid Earth*, *119*(4), 3050–3063. https://doi.org/10.1002/2013JB010534

Shipboard Scientific Party. (2002). Leg 199 Preliminary Report. *ODP Preliminary Report*, *99*, 105. https://doi.org/doi: 10.2973/odp.proc.ir.199.101.2002

Skemer, P., & Hansen, L. N. (2016). Inferring upper-mantle flow from seismic anisotropy: An experimental perspective. *Tectonophysics*, *668–669*, 1–14. https://doi.org/10.1016/j.tecto.2015.12.003

Skemer, P., Warren, J. M., & Hirth, G. (2012). The influence of deformation history on the interpretation of seismic anisotropy. *Geochemistry, Geophysics, Geosystems*, *13*(3). https://doi.org/10.1029/2011GC003988

Snydsman, W. E., Lewis, B. T. R., & McClain, J. (1975). Upper mantle velocities on the Northern Cocos Plate. *Earth and Planetary Science Letters*, *28*(1), 46–50. https://doi.org/10.1016/0012-821X(75)90072-2

Sobolev, P. O., & Rundquist, D. V. (1999). Seismicity of oceanic and continental rifts—a geodynamic approach. *Physics of the Earth and Planetary Interiors*, *111*(3–4), 253–266. https://doi.org/10.1016/S0031-9201(98)00165-4

Solomon, S. C., & Sleep, N. H. (1974). Some simple physical models for absolute plate motions. *Journal of Geophysical Research (1896-1977)*, *79*(17), 2557–2567. https://doi.org/10.1029/JB079i017p02557

Solomon, S. C., Huang, P. Y., & Meinke, L. (1988). The seismic moment budget of slowly spreading ridges. *Nature*, *334*(6177), 58–60. https://doi.org/10.1038/334058a0

Stein, C. A., & Stein, S. (1992). A model for the global variation in oceanic depth and heat flow with lithospheric age. *Nature*, *359*(6391), 123–129.

Stixrude, L., & Lithgow-Bertelloni, C. (2005). Mineralogy and elasticity of the oceanic upper mantle: Origin of the low-velocity zone. *Journal of Geophysical Research*, *110*(B3). https://doi.org/10.1029/2004JB002965

Takeo, A., Kawakatsu, H., Isse, T., Nishida, K., Sugioka, H., Ito, A., et al. (2016). Seismic azimuthal anisotropy in the oceanic lithosphere and asthenosphere from broadband surface wave analysis of OBS array records at 60 Ma seafloor. *Journal of Geophysical Research: Solid Earth*, *121*(3), 1927–1947. https://doi.org/10.1002/2015JB012429

Tan, Y., & Helmberger, D. V. (2007). Trans-Pacific upper mantle shear velocity structure. *Journal of Geophysical Research*, *112*(B8). https://doi.org/10.1029/2006JB004853

Taylor, B., Weiss, J. R., Goodliffe, A. M., Sachpazi, M., Laigle, M., & Hirn, A. (2011). The structures, stratigraphy and evolution of the Gulf of Corinth rift, Greece. *Geophysical Journal International*, *185*(3), 1189–1219. https://doi.org/10.1111/j.1365-246X.2011.05014.x

Tharimena, S., Rychert, C., Harmon, N., & White, P. (2017). Imaging Pacific lithosphere seismic discontinuities-Insights from SS precursor modeling. *Journal of Geophysical Research: Solid Earth*. https://doi.org/10.1002/2016JB013526

Thomsen, L. (1995). Elastic anisotropy due to aligned cracks in porous rock. *Geophysical Prospecting*, *43*(6), 805–829. https://doi.org/10.1111/j.1365-2478.1995.tb00282.x

Tichelaar, B. W., & Ruff, L. J. (1993). Depth of seismic coupling along subduction zones. *Journal of Geophysical Research: Solid Earth*, *98*(B2), 2017–2037. https://doi.org/10.1029/92JB02045

Toomey, D. R., Wilcock, W. S. D., Conder, J. A., Forsyth, D. W., Blundy, J. D., Parmentier, E. M., & Hammond, W. C. (2002). Asymmetric mantle dynamics in the MELT region of the East Pacific Rise. *Earth and Planetary Science Letters*, *200*(3), 287–295. https://doi.org/10.1016/S0012-821X(02)00655-6

Toomey, D. R., Jousselin, D., Dunn, R. A., Wilcock, W. S. D., & Detrick, R. S. (2007). Skew of mantle upwelling beneath the East Pacific Rise governs segmentation. *Nature*, *446*(7134), 409–414. https://doi.org/10.1038/nature05679

Tucholke, B. E., Behn, M. D., Buck, W. R., & Lin, J. (2008). Role of melt supply in oceanic detachment faulting and formation of megamullions. *Geology*, *36*(6), 455–458.

Turner, A. J., Katz, R. F., & Behn, M. D. (2015). Grain-size dynamics beneath mid-ocean ridges: Implications for permeability and melt extraction. *Geochemistry, Geophysics, Geosystems*, *16*(3), 925–946. https://doi.org/10.1002/2014GC005692

Turner, A. J., Katz, R. F., Behn, M. D., & Keller, T. (2017). Magmatic Focusing to Mid-Ocean Ridges: The Role of Grain-Size Variability and Non-Newtonian Viscosity. *Geochemistry, Geophysics, Geosystems*, *18*(12), 4342–4355. https://doi.org/10.1002/2017GC007048

Turner, F. J. (1942). Preferred orientation of olivine crystals in peridotites, with special reference to New Zealand examples. *Transactions and Proceedings of the Royal Society of New Zealand*, *72*(3), 280–300.

VanderBeek, B. P., & Toomey, D. R. (2017). Shallow Mantle Anisotropy Beneath the Juan de Fuca Plate. *Geophysical Research Letters*, *44*(22), 11,382-11,389. https://doi.org/10.1002/2017GL074769

VanderBeek, B. P., Toomey, D. R., Hooft, E. E. E., & Wilcock, W. S. D. (2016). Segmentation of mid-ocean ridges attributed to oblique mantle divergence. *Nature Geoscience*, *9*(8), 636–642. https://doi.org/10.1038/ngeo2745

Verma, R. K. (1960). Elasticity of some high-density crystals. *Journal of Geophysical Research*, *65*(2), 757–766. https://doi.org/10.1029/JZ065i002p00757

Vidale, J. E., & Houston, H. (2012). Slow slip: A new kind of earthquake. *Physics Today*. https://doi.org/10.1063/PT.3.1399

Voglis, C., & Lagaris, I. E. (2004). A Rectangular Trust Region Dogleg Approach for Unconstrained and Bound Constrained Nonlinear Optimization (p. 7). Presented at the WSEAS.

Wang, L., Miyajima, N., Kawazoe, T., & Katsura, T. (2019). Activation of [100](001) slip system by water incorporation in olivine and the cause of seismic anisotropy decrease with depth in the asthenosphere. *American Mineralogist*, *104*(1), 47–52. https://doi.org/10.2138/am-2019-6574

Wech, A. G., Creager, K. C., & Melbourne, T. I. (2009). Seismic and geodetic constraints on Cascadia slow slip. *Journal of Geophysical Research: Solid Earth*, *114*(B10), B10316. https://doi.org/10.1029/2008JB006090

Wessel, P., Smith, W. H. F., Scharroo, R., Luis, J., & Wobbe, F. (2013). Generic Mapping Tools: Improved Version Released. *Eos, Transactions American Geophysical Union*, *94*(45), 409–410. https://doi.org/10.1002/2013EO450001

Whittaker, J. M., Müller, R. D., Leitchenkov, G., Stagg, H., Sdrolias, M., Gaina, C., & Goncharov, A. (2007). Major Australian-Antarctic Plate Reorganization at Hawaiian-Emperor Bend Time. *Science*, *318*(5847), 83–86. https://doi.org/10.1126/science.1143769

Wiemer, S., & Wyss, M. (2000). Minimum Magnitude of Completeness in Earthquake Catalogs: Examples from Alaska, the Western United States, and Japan. *Bulletin of the Seismological Society of America*, *90*(4), 859–869. https://doi.org/10.1785/0119990114

Wiens, D. A., & Stein, S. (1984). Intraplate seismicity and stresses in young oceanic lithosphere. *Journal of Geophysical Research: Solid Earth*, *89*(B13), 11442–11464. https://doi.org/10.1029/JB089iB13p11442

Wilson, J. T. (1965). Evidence from ocean islands suggesting movement in the Earth. *Philosophical Transactions of the Royal Society of London. Series A, Mathematical and Physical Sciences*, *258*(1088), 145–167. https://doi.org/10.1098/rsta.1965.0029

Yuan, X., Kind, R., Li, X., & Wang, R. (2006). The S receiver functions: synthetics and data example. *Geophysical Journal International*, *165*(2), 555–564. https://doi.org/10.1111/j.1365-246X.2006.02885.x

Zelt, B. C., Taylor, B., Sachpazi, M., & Hirn, A. (2005). Crustal velocity and Moho structure beneath the Gulf of Corinth, Greece. *Geophysical Journal International*, *162*(1), 257–268. https://doi.org/10.1111/j.1365-246X.2005.02640.x

Zhang, S., & Karato, S. (1995). Lattice preferred orientation of olivine aggregates deformed in simple shear. *Nature*, *375*(6534), 774–777. https://doi.org/10.1038/375774a0

Zhang, S., Karato, S., Gerald, J. F., Faul, U. H., & Zhou, Y. (2000). Simple shear deformation of olivine aggregates. *Tectonophysics*, *316*(1), 133–152.

Zhong, X., Frehner, M., Kunze, K., & Zappone, A. (2014). A novel EBSD-based finite-element wave propagation model for investigating seismic anisotropy: Application to Finero Peridotite, Ivrea-Verbano Zone, Northern Italy. *Geophysical Research Letters*, *41*(20), 7105–7114. https://doi.org/10.1002/2014GL060490